MASTERARBEIT / MASTER’S THESIS

Titel der Masterarbeit / Title of the Master‘s Thesis

„Cloud condensation nuclei (CCN) activity of extracts from selected wind pollinated plants“

verfasst von / submitted by

Sebastian Sonnenberg BSc

angestrebter akademischer Grad / in partial fulfilment of the requirements for the degree of

Master of Science (MSc)

Wien, 2021

Studienkennzahl lt. Studienblatt / degree programme code as it appears on the student record sheet:	A 066 876
Studienrichtung lt. Studienblatt / degree programme as it appears on the student record sheet:	Physik (Master)
Betreut von / Supervisor:	Mag. Dr. Julia Burkart
Mitbetreut von / Co-Supervisor:	

Contents

1 Danksagung 3

2 Zusammenfassung 4

3 Abstract 6

4 Introduction 8
- 4.1 Atmospheric aerosols . . . 9
- 4.2 Bioaerosols . . . 12
- 4.3 Pollen . . . 14
  - 4.3.1 Composition of Pollen . . . 14
  - 4.3.2 Pollination process . . . 14
  - 4.3.3 Concentration of Pollen in the atmosphere . . . 15
- 4.4 Pollen rupture . . . 16
- 4.5 Investigated pollen species . . . 17
  - 4.5.1 Betula pendula . . . 17
  - 4.5.2 Artemisia vulgaris . . . 18
  - 4.5.3 Ambrosia artemisiifolia . . . 18
  - 4.5.4 Corylus avellana . . . 18
  - 4.5.5 Phleum pratense . . . 18

5 Clouds and droplet formation 19
- 5.1 Clouds . . . 19
  - 5.1.1 Mechanics behind the formation of a cloud . . . 19
  - 5.1.2 Importance for atmosphere and energy budget . . . 20
  - 5.1.3 Macroscopic properties . . . 20
  - 5.1.4 Microscopic properties . . . 21
- 5.2 Droplet formation . . . 22
  - 5.2.1 Thermodynamics of liquid-vapor systems . . . 22
  - 5.2.2 Homogenous nucleation . . . 24
  - 5.2.3 Kelvin . . . 25
  - 5.2.4 Heterogenous nucleation . . . 26
  - 5.2.5 Deliquescence and hygroscopic growth . . . 27
  - 5.2.6 Raoult's law . . . 28
  - 5.2.7 Koehler equation . . . 29
  - 5.2.8 Hygroscopicity parameter κ . . . 32

6 Experimental 33
- 6.1 CCNC . . . 33
  - 6.1.1 Operation principle . . . 33
  - 6.1.2 Growth chamber . . . 35
  - 6.1.3 Calculating the centerline supersaturation . . . 36
  - 6.1.4 Flow calibration . . . 37
- 6.2 DMA . . . 38
  - 6.2.1 Theory and operation principle . . . 38
  - 6.2.2 Transferfunction . . . 41
  - 6.2.3 PSL measurements . . . 41
- 6.3 Experimental Setup . . . 43
  - 6.3.1 Setup and schematic of the experiment . . . 43

6.3.2 General procedure of the experiment 45
6.4 Calibration 45
6.4.1 D-scans 46
6.4.2 Data fitting procedure 48
6.4.3 Correction of doubly charged particles 49
6.4.4 Calculating the effective supersaturation and plotting the calibration line 51
6.4.5 S-scans 52
6.4.6 Pollen measurements 54
6.5 Results 55
6.5.1 Discussion and comparison with other studies 60
6.5.2 Impact of cytoplasm fragments on cloud formation 62
6.5.3 Suggested improvements and outlook 63
6.6 Outro 64

1 Danksagung

Mein großer Dank gilt meiner Betreuerin Dr. Julia Burkart, welche mir bei Zeiten der Unsicherheit und Probleme immer zur Hilfe stand. Ich bin auf das Thema durch das Aerosolseminar gekommen, wo ich bereits von Dr. Burkart bei einem Vortrag über dieses Thema betreut wurde. Ich möchte mich daher an dieser Stelle an Dr. Burkart vielmals bedanken, dass ich die Möglichkeit erhalten habe für meine Masterarbeit an diesem spannenden Thema weiterzuarbeiten.

Ebenso gilt mein großer Dank an Jürgen Gratzl für die Herstellung der Probelösungen welche im Zuge meiner Arbeit untersucht wurden. Meine Arbeit ist damit eine direkte Folge der Arbeit von Jürgen Gratzl und ich bedanke mich auch an dieser Stelle für die Erklärungen und Unterstüzung bei meinen Fragen und Unsicherheiten zum Thema.

Desweiteren bedanke ich mich an die Aerosolgruppe für die Unterstützung bei diversen Fragen, allen voran Max Dollner für die Unterstżung mit der Software IGOR, welche für das Zeichnen von einigen Graphen in meiner Arbeit verwendet wurde und Dr. Maria del Carmen Dameto de Espana, welche mir immer bei theoretischen Fragen zum CCN Thema geholfen hat.

Zuletzt gilt mein enormer Dank meinen Eltern MaŁgorzata und Gerhard Sonnenberg, deren massive Unterstützung die Fertigstellung dieser Arbeit ermöglicht hat.

2 Zusammenfassung

Aerosolpartikel in the Atmosphäre können als sogenannte Kondensationskeime (im Englischen Cloud Condensation Nuclei, kurz CCN) fungieren. Damit haben sie einen enormen Einfluss auf die Entwicklung von Wolken und folglich auf die Strahlungsbilanz unseres Planeten (Seinfeld and Spyros (2006), Lohmann and Feichter (2005)). Die wichtigsten Paremeter, welche die CCN-Fähigkeit eines Partikels festlegen, sind dessen Größe, chemische Zusammenzetzung und die aktuelle Übersättigung in der Atmosphäre. Große Partikel, welche eine Menge an hydrophilen Substanzen beinhalten, sind die effektivsten CCN.

In den letzten Jahrzehnten wurde der Partikelfraktion mit biologischen Ursprung mehr Beachtung geschenkt, insbesondere aufgrund deren Einfluss auf die menschliche Gesundheit und den grossen Unsicherheiten bezüglich deren gemessenen Massen- und Anzahlkonzentration in der Atmosphäre (Despres et al. (2012), Andreae and Rosenfeld (2008)). Während der Blütezeit werden von verschiedenen Pflanzenarten Pollen in großen Mengen ausgesendet um andere Pflanzen zu befruchten und die Produktion von neuen Samen einzuleiten. In Regionen wo der Bestäubungsprozess hauptsächlich anemophilen Charakter hat können Pollenkörner lange Strecken in der Luft zurücklegen und somit ist es ihnen möglich an verschiedensten atmosphärischen Prozessen teilnehmen. Dies erlaubt es ihnen auf das Klimasystem der Erde einzuwirken. Ganze Pollenkörner haben die Fähigkeit Wasser auf ihrer Oberfläche zu kondensieren, was bereits zuvor erwiesen wurde (Pope (2010)). Pollenkörner, deren Größe 10 μm - 100 μm beträgt, deuten allerdings auf eine kurze Verweildauer in der Luft, wodurch sie keinen signifikanten Beitrag zur globalen atmosphärischen CCN Konzentration erbringen.

In Zeiten von hoher Luftfeuchtigkeit können ganze Pollenkörner durch einen Prozess, den man Osmotischen Schock nennt zerreissen und zytoplasmatisches Material aus ihrem Inneren herausstoßen (Steiner et al. (2015), Miguel et al. (2006), Taylor et al. (2004), Taylor et al. (2002)). Viele Pollenkörner, hauptsächlich jene, die von anemophilen Pflanzen produziert werden, besitzen unlösliche Stärkekörner in ihren vegetativen Zellen (Baker and Baker (1979)), welche mitsamt löslichem zytoplasmatischen Material während des Zerreissens ausgestoßen werden. Diese Stärkekörner werden im Englischen als sogenannte Subpollen Submicron Particles (SPP) bezeichnet (Steiner et al. (2015)). Kleiner als die ganzen Pollenkörner und beschichtet mit dem löslichen zytoplasmatischem Material, könnten diese Partikel einen wesentlichen Einfluss auf regionale CCN Konzentrationen haben, falls die Anzahl an produzierten Pollenkörner hoch genug ist.

Das Ziel dieser Studie ist die Analyse der CCN Aktivität der löslichen zytoplasmatichen Materialfraktion, welche von 6 verschiedenen Pollenarten extrahiert wurde. Die Namen dieser 6 Pollenarten lauten *Betula pendula* (Birch), *Phleum pratense* (Timothy grass), *Poa pratensis* (blue grass), *Corylus avellana* (Hazel), *Artemisia vulgaris* (Mugwort) and *Ambrosia artemisiifolia* (Ragweed). Die veröffentlichte Masterarbeit von Gratzl (2020) beschreibt den detaillierten Prozess wie das zytoplasmatische Material aus einem Pollenkorn extrahiert wird und die anschließende Trennung zwischen den unlöslichen Stärkekörner und dem löslichen zytoplasmatischen Material. Beide wurden dann anschließend als Probelösungen für weitere Messungen vorbereitet. Meine Arbeit legt den Fokus auf die Bestimmung der CCN Fähigkeit der löslichen zytoplasmatischen Substanz und untersucht ob die durch einen Zerstäuber generierten Teilchen dieses Materials unter atmosphärischen Bedingungen als Kondensationskeime fungieren können und ob sie einen Einfluss auf die Bildung von Wolken haben könnten.

Bei der Durchfürung des experimentellen Teils diese Arbeit wurde ein sogenannten Cloud

Condensation Nuclei Counter (CCNC) von Droplet Measurement Technologies verwendet. Dieser misst die Anzahl der ankommenden Partikel welche bei einer bestimmten eingestellten Übersättigung zu Wolkentröpfchen anwachsen können (Rose et al. (2008), Roberts and Nenes (2005)). Der erste Teil des Experiments beinhaltet die Kalibrierung des CCNC mit $(NH_4)_2SO_4$ Partikeln. Dadurch kann die Beziehung zwischen dem Temperaturgradienten, welche für die Generierung der eingestellten Übersättigung im CCNC verantwortlich ist und der sogenannten effektiven Übersättigung SS_{eff} gefunden werden. SS_{eff} ist die wirksame Übersättigung in der CCNC Kammer, welche zu deren jeweiligen Temperaturgradienten korrespondiert. Sie ist definiert als jene Übersättigung bei der 50% der ankommenden Probepartikel aktivieren können falls deren trockene Größe mindestens einen kritischen Wert $D_{s,crit}$ erreicht haben. Im zweiten Teil des Experimentes werden Aktivierungskurven von den 6 Zytoplasma Probelösungen gemessen. Dies findet jeweils mit der D-Scan und S-Scan Methode statt.

Durch Verwendung der klassischen Köhlertheorie koennen wir aus jeder D-Scan Aktivierungskurve einen kritischen Trockendurchmesser $D_{s,crit}$ berechnen. Mit Hilfe des κ - Köhler Modells können wir die Kondensationsfähigkeit dieser Proben durch einen einzelnen Hygroskopizittsparameter κ festlegen (Petters and Kreidenweis (2007)). Die κ Ergebnisse fuer $(NH_4)_2SO_4$ liegen auf einem konstanten Wert von 0.73 während die Ergebnisse für die Zytoplasma Proben im Intervall 0.1 - 0.2 liegen. Auf der niedrigsten gemessenen effektiven Uebersättigung SS_{eff} weist die Poa Probe mit einem κ Wert von 0.2 die höchste Affinität zu Wasser auf während Artemisia mit einem Wert von 0.13 den niedrigsten hydrophilen Charakter aufweist. κ Werte im Intervall 0.1 - 0.4 korrespondieren zu einer moderaten Hygroskopizität. Dies ist aufgrund dem Vorhandensein von organischen Komponenten zurückzuführen (Petters and Kreidenweis (2007)). Die kleine Größenregion (<200nm) von den Probepartikel und deren Fähigkeit zur CCN Aktivierung bei Üebersättigungen typisch für atmosphärische Wolken (<1%) zeigen, dass das zytoplasmatische Material in Teilchenform die Entwicklung und Eigenschaften von Wolken beinflussen kann. Jedoch kommt die Stärke dieses Einflusses auf deren Anzahlkonzentration an.

Wenn man die κ Ergebnisse der Proben mit den κ Werten von ganzen Pollenkörnern, welche im Bereich 0.05 - 0.1 (Pope (2010)) liegen vergleicht, dann sieht man die stärkere Wasseraffinität des löslichen zytoplasmatischen Materials. Die wichtisten Komponenten des zytoplasmatischen Materials von Pollen sind Proteine und Polysaccharide, letztere werden hauptsächlich durch Stärke vertreten. Die geringe Größe von Subpollen Submicron Particles und die moderate Hygroskopizität des zytoplasmatischen Materials machen deren Kombination eine potentielle zusätzliche Quelle an organischem CCN in Regionen wo der Bestäubungsprozess hauptsächlich durch Wind verursacht wird (Steiner et al. (2015), Despres et al. (2012)).

3 Abstract

Atmospheric aerosol particles serving as Cloud Condensation Nuclei (CCN) have a significant influence on the formation of clouds and thus on the radiative balance of the planet (Seinfeld and Spyros (2006), Lohmann and Feichter (2005)). The crucial parameters that determine a particle's CCN activation and droplet growth are it's size, it's chemical composition and the current supersaturation level in the atmosphere. Particles with large sizes and chemical compounds that favour the uptake of water are the most effective CCN.

In the recent decades the biological fraction of the atmospheric aerosol population has received more attention in environmental studies due to their impact on human health and the large uncertainties regarding their atmospheric number and mass concentrations (Despres et al. (2012), Andreae and Rosenfeld (2008)).During the blooming season of flowers pollen grains are emitted in large quantities by various species for the purpose of fertilizing other plants to induce the growth of new seeds. In regions where the majority of pollination processes are anemophilous, pollen can travel long distances through the air and thus take part in atmospheric processes which influence the earth's climate system. Whole pollen grains have already showcased the ability act as CCN and enable the condensation of water (Pope (2010)) but their large size (10μm - 100μm) indicates a short residence time in the air, making them unable to bring any significant contribution to the atmospheric CCN concentration.

During conditions of high moisture pollen grains can rupture due to a process defined as osmotic shock and emit cytoplasm content from it's vegetative cell (Steiner et al. (2015), Miguel et al. (2006), Taylor et al. (2004), Taylor et al. (2002)). Many pollen grains, mainly those emitted by anemophilous plants contain unsoluble starch granules inside their cell (Baker and Baker (1979)) which are released alongside more soluble cytoplasm compounds during this process. These starch granules are commonly reffered to as Subpollen Submicron Particles (SPP) (Steiner et al. (2015)). Smaller in size and coated in soluble cytoplasm material these particles could make a significant contribution to regional atmospheric CCN concentrations if the number of emitted pollen grains are sufficiently high. The goal of this study is to analyze the CCN activity of of the soluble organic cytoplasm material extracted from 5 different wind-pollinated plant species. The method developed in the published master thesis of Gratzl (2020) describes the detailed process of extracting the cytoplasm content from a pollen grain and seperate the soluble cytoplasm compounds from the unsoluble starch granules before preparing both as sample solutions for further measurements. This work focuses on determining the CCN ability of the soluble cytoplasm fraction and to determine if atomized cytoplasm fragments can activate under atmospheric conditions and wheter they can have an impact on the formation of clouds.

The experimental setup for this work constitutes the Cloud Condensation Nuclei Counter (CCNC) with a continuous flow from Droplet Measurement Technologies which measures the number of incoming particles that activate and grow into cloud droplets (Rose et al. (2008), Roberts and Nenes (2005)). The first part of the experiment involves calibrating the CCNC with an aquaous dilute solution of $(NH_4)SO_2$. This determines the relationship between the temperature gradient established in the CCNC and the effective supersaturation SS_{eff}, the true supersaturation that corresponds to said temperature gradient where 50% of incoming sample particles activate into cloud droplets if they reach a certain critical dry size $D_{s,crit}$. The second part involves recording activation spectra of the 5 cytoplasm sample solutions using both the D-Scan and S-Scan method of measuring an activation curve.

By using the classical Koehler model, from each activation curve a critical dry diameter can be

derived, indicating the size where 50% of all particles entering the CCN can activate and grow into cloud droplet. Using the κ - Koehler model the condensation activity of these samples can be determined through the hygroscopicity parameter κ (Petters and Kreidenweis (2007)). κ values for $(NH_4)SO_2$ measurements stay at a constant value of 0.73 while values for the cytoplasm samples vary all lie within the range of 0.1 - 0.2. At the lowest effective supersaturation the Poa samples show the highest hygroscopicity with a κ value of 0.2 while Artemisia showcases the lowest with a value of 0.13.. Values in the range of 0.1 - 0.4 for κ indicate moderate condensation activity due to the presence of organic constituents (Petters and Kreidenweis (2007)). Given their low size (<200nm) and their ability to activate at supersaturations typical for clouds (<1%) these cytoplasm fragments can impact cloud formation processes, depending on their number concentrations which can vary greatly regionally.

When compared with the κ results of whole pollen grains which lie in the range 0.05 - 0.1 (Pope (2010)) the cytoplasm samples showcase a stronger water affinity. The main components of pollen cytoplasm are proteins and polysaccharides, the latter mainly being represented by unsoluble starch. The smaller size of Subpollen Particles, which increases their time in the atmosphere and the moderate water affinity of pollen cytoplasm makes their combination a potential source of additional organic CCN in regions where pollination is predominantly occuring through wind updrafts (Steiner et al. (2015), Despres et al. (2012)).

4 Introduction

Aerosols in the atmosphere are next to water the most crucial component for the formation of clouds. Most commonly aerosols are defined as mixtures of particles suspended in a carrier gas (Hinds (2012), Seinfeld and Spyros (2006), Lohmann et al. (2016)). The particles themselves can appear in either solid or liquid form while the carrier gas for atmospheric aerosols is the air itself. In literature it is common to equate the term aerosol with the aerosol particles but when describing the properties of an aerosol we mean the properties of the particles without the carrier gas (Hinds (2012). In this work I will also follow suit, equating the terms but all described properties only refer to the particles without the carrier gas.

Aerosols have a substantial influence on our climate system through their interaction with incoming sunlight and terrestial radiation emitted from the earth's surface. They can both scatter and absorb portions of both types of radiation. The net result that an aerosol particle can have on an incoming beam of light depends on it's size and is described in detail through it's refractive index (Hinds (2012), Boucher (2015)). Their overall overall global forcing effect on the radiative balance is estimated according to the IPCC as -0.50 ± 0.40 Wm^{-2} (Forster (2007)), thus cooling the atmosphere and surface. Depending on the chemical composition and size of the aerosols they can individually provide a higher or lower forcing effect on the planet. Through these interactions the intensity of incoming radiation diminishes, described through the extinction coefficient (Hinds (2012)) which is a function of the particle's size. For the human eye these interactions with light showcase themselves in a change of visibility. An aerosol particle with a weak extinction effect on the red wavelength portion of light means that the human eye will see the wavelength portion corresponding to blue and green much stronger.

Next to this direct influence on the climate aerosol particles can also serve as both cloud condensation nuclei or Ice nuclei, affecting the formation of clouds and thus having an indirect influence on the climate (Lohmann et al. (2016), Hinds (2012), Seinfeld and Spyros (2006), Ramanathan et al. (2002)). This effect is credited with the highest amount of uncertainty for the earth's radiative balance and is described more in detail in the next chapter.

The arguably strongest parameter for the classification of aerosols is the size of the particles. It is expressed through the diameter of the spherically shaped particle. The particle diameter influences other properties like the particle's settling velocity and the amount of raditation it can scatter at different wavelengths. Depending on the value of the diameter one can group aerosols into the nucleation mode (1nm - 10nm), the Aitken mode (10nm - 100nm), the accumulation mode (0.1μm - 2.5μm) or the coarse mode ($\geq$ 2.5μm) (Hinds (2012), Seinfeld and Spyros (2006)). Particles from nuclei, aitken and accumulation mode are also commonly reffered to as fine particles.

Measurements in the laboratory often require monodisperse aerosol sample flows which can be generated through size classifying techniques. One of them, the process of classifying particles according to their electrical mobility is used in this work to generate a monodisperse sample flow. In the atmosphere particle size of an aerosol isn't constant as processes like condensation, evaporation and coagulation continue to bring size change through the aerosol population during it's entire lifetime.

Aerosols in the atmosphere consist of multiple modes, making them polydisperse. They are also not homogenous, meaning they consist of particles of various chemical compositions.

4.1 Atmospheric aerosols

The atmospheric aerosol population consists of a mix of various particles of different sizes and chemical compositions. Polydisperse aerosols of various origin exist over both continental and marine surfaces. Due to the vast number of different sources of origin and their relatively short lifetime (as short as a few hours to multiple weeks) in the atmosphere their properties like number concentration and size distribution vary greatly over time and space(Boucher (2015)). Aerosol particles also don't stay in one place during their residence time. Through horizontal wind currents they also travel over large distances which allows them to collide and stick to other particles, grow into droplets by travelling to regions of higher humidity or landing on trees or buildings. This provides another influence on their variability. Airborne particles from both nucleation and aitken mode dominate the number concentration in the atmosphere while particles from the coarse mode make up the majority of the particle mass in the air (Seinfeld and Spyros (2006)). Due to the polydisperse nature of atmospheric aerosols, the size distribution is next to the mass and number concentration an important measured quantity. Number concentrations of aerosols in the atmsphere can reach values as high as $4 \cdot 10^6 cm^{-3}$ in urban regions and values in the range $50 - 10^4 cm^{-3}$ in remote continental areas.

Atmospheric aerosols can be divided into primary and secondary aerosols. Primary aerosol particles are those which are directly emitted into the atmosphere, transported through updrafts into the air from both terrestial and marine surfaces. Secondary particles are formed directly in the air, through chemical reactions of so called precursor gases. Examples for such precursor gases are nitrogen oxides and volatile organic compounds (VOCs). The products from the oxidation of these precursors can either form new particles through nucleation or condense onto already existing particles. The chemical composition of airborne particles can give a hint as to where particles are secondary of primary since since some chemical species are known to be formed through the reactions of precursor gases (Boucher (2015)).

It is also common to categorize aerosols according to the type of environment they are found. From Hinds (2012) aeosols are commonly distinguished between natural background aerosols and urban aerosols. Natural background aerosols are specified as the aerosols which would be present if human acitivty was absent, thus all the primary and secondary particles having their origin in natural sources. Urban aerosol is largely dominated by anthropogenic sources but contain also fractions of natural background aerosols. While the number of anthropogenic sources is smaller than the amount of natural sources, their contribution (in percentage) to global particulate emissions can reach up to 50% (Hinds (2012)). Though a categorization in urban and natural background aerosol is rather flawed due to the previously mentioned ability of aerosols to travel long distances. For example we can find aerosols that are typical over oceans also over continental regions (Boucher (2015)).

A more general approach in categorizing aerosols is thus to distinguish between emissions from either natural or anthropogenic sources. Major representatives for particles of natural origin include sea spray aerosols, droplets consisting of various hygroscopic salts as well as organic components. Due to the friction with wind currents along marines surfaces these droplets are transported into the air where they loose a fraction of their water content, resulting in an increase of salt concentration. They are also said to be produced by entrained air bubbles rising to the ocean surface and their eventual bursting (Tomasi et al. (2016)). The sizes for these are in the range of 100 nm to several tens of μm (Boucher (2015)) and thus many of them have a short residence time in the air before falling back into the sea, making them less relevant for atmospheric processes. However despite that their strong water affinity due to the inorganic salts makes them the most important source for cloud condensation nuclei above oceanic regions and thus responsible for most cloud formations over oceans (O'Dowd et al.

(1997)). Another major contributor to the particle population of natural origin is Desert Dust, also called Mineral Dust. Major sources for dust particles are desertic regions like the Sahara desert were wind speed along the surface isn't halted by vegetation. Mineral Dust represents the major fraction of natural background aerosols in the atmosphere above subtropical regions (Tomasi et al. (2016)). Just like sea spray, mineral dust particles lie in the size range of 100 nm to several tens of μm and emissions into the atmosphere are sporadic, making them also a very unreliable influence on atmospheric processes. Ash emitted during the eruptons of volcanoes are another natural source of particles. Due to their large size (few μm to a few mm) makes their residence times even shorter spea spray and mineral dust. However volcanoes can also expell volatile precursor gases like SO_2 (sulphur dioxide) which through oxidation can become particulate matter. Furtheremore sometimes volcanoes can emit those precursor gases beyond the troposphere, into the stratosphere which in turn increases their lifetime in the atmosphere.

The most important processes with generate aerosols of anthropogenic origin includes the combustion of fossil fuel, the burning of biomass and various other industrial processes. Both the combustion of fossil fuels and biomass produces black carbon and organic carbon, the latter in the form of both primary or secondary particles. They also produce volatile precursos gases such as sulphur dioxide and nitrogen oxides which have negative impacts on human health, causing respiratory and cardio-vascular diseases. The emissions from both processes are most likely to double down by the year 2040, with China and India predicted as the major sources of anthropogenic increases (Tomasi et al. (2016)).

Figure 1 showcases the contributions to the global aerosol mass (in Teragramm) of primary and secondary particles from both natural and anthropogenic sources.

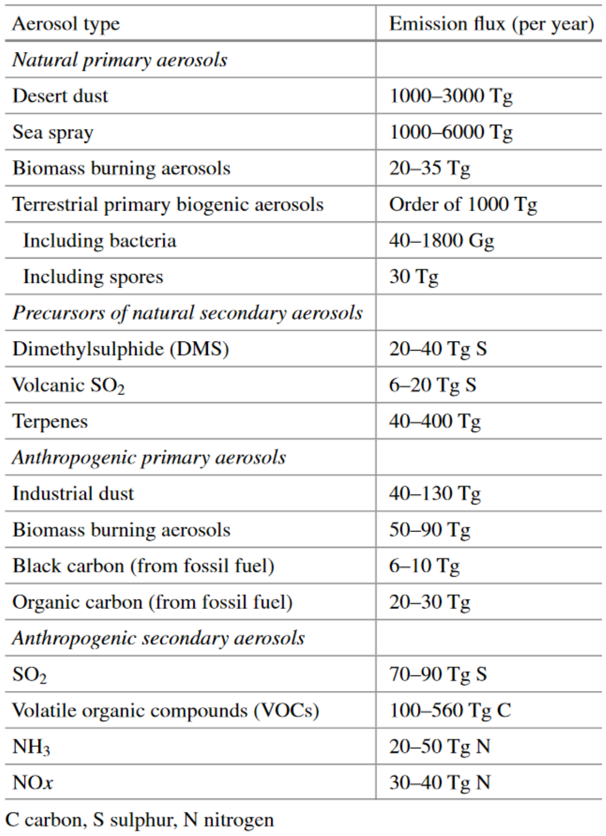

Aerosol type	Emission flux (per year)
Natural primary aerosols	
Desert dust	1000–3000 Tg
Sea spray	1000–6000 Tg
Biomass burning aerosols	20–35 Tg
Terrestrial primary biogenic aerosols	Order of 1000 Tg
Including bacteria	40–1800 Gg
Including spores	30 Tg
Precursors of natural secondary aerosols	
Dimethylsulphide (DMS)	20–40 Tg S
Volcanic SO_2	6–20 Tg S
Terpenes	40–400 Tg
Anthropogenic primary aerosols	
Industrial dust	40–130 Tg
Biomass burning aerosols	50–90 Tg
Black carbon (from fossil fuel)	6–10 Tg
Organic carbon (from fossil fuel)	20–30 Tg
Anthropogenic secondary aerosols	
SO_2	70–90 Tg S
Volatile organic compounds (VOCs)	100–560 Tg C
NH_3	20–50 Tg N
NO_x	30–40 Tg N

C carbon, S sulphur, N nitrogen

Figure 1: Major mass contributions of various aerosol sources, adapted from Boucher (2015)

Because of their microscopic size atmospheric aerosols can vary visibility to a great amount if their number concentrations have reached sufficient values. Figure 2 showcases how the collective effect of Saharan dust over the Alps changes visibility. Due to their extinction ability the human eye sees the wavelengths responsible for the orange colour much stronger.

Figure 2: Influence of visibility due to Saharan dust, adapted from Boucher (2015)

Increasing human activity has modified the chemical composition and physical properties of atmospheric aerosols tremendously. Model calculations have shown that number concentrations of particles in the pristine atmosphere above continents were similar to number concentrations over marine regions today, showcasing a stronger than anticipated increase in pollution due to human acitivities (Andreae and Rosenfeld (2008)). An important fraction of anthropogenic emissions is represented by greenhouse gases, which are the main driver for the increased warming of our climate system. The 3 main anthropogenic greenhouse gases (CO_2, CH_4 and N_2O) have increased tremendously the time period of 1765 - 2005 (Boucher (2015)).

Due to both their direct and indirect influence on climate and their effect on human health, the measurement and study of properties like the number concentration (typically given as number of particles per cm^3) and the size distribution (given as number of particles per size intervall), as well as the chemical constinuents within aerosols from various sources has been an important topic in environmental models in the last decades (Despres et al. (2012), Tomasi et al. (2016)).

My work focuses on Pollen, belonging to the biological fraction (of primary type) of the atmospheric aerosol. This is why the next section will give a more thorough description and characterization of atmospheric aerosols of biological origin.

4.2 Bioaerosols

Bioaerosols are commonly defined as both secondary and primary particles emitted by biological sources. The primary sources of origin for these are humans, animals and plants. Other sources include water and soil which inhabit various biological microorganisms that can find themselves in the air through wind turbulence. Various types of plantlife emit both primary microbial (microbiological) particles and low volatility gaseous precursors mainly due to decay processes. Many plant organisms also emit bioparticles with the goal or reproduction (pollen, fungal spores).

Once in the atmosphere bioparticles can be part of the atmosphere for quite a long time, travelling through wind currents or sticking at insects before they are deposited to the ground or on other surfaces. Thus they can take part in atmospheric processes and serve as both condensation (assuming a wettable surface) and ice nuclei and thereby influence cloud formation processes (Steiner et al. (2015), Despres et al. (2012), Pöschl et al. (2010), Hoose et al. (2010), Andreae and Rosenfeld (2008)). Atmospheric bioparticles often carry the reproductive unit from their respective parent plant species and thus they are a major contributor to the spread of organisms in regions of dense vegetation, thus being a crucial aspect in the development and dynamics of ecosystems (Fröhlich-Nowoisky et al. (2016)). The Composition, abundance and interaction of bioparticles with the earth's climate and ecosystem are not fully explored and characterized yet.

Figure 3 gives both the size (through the particle diameter) and number concentration range for a few types of primary bioparticles in outdoor environments. When compared to typical aerosol number concentrations in urban environments these numbers are rather low.

Type of Bioaerosol	Size (μm)	Concentration (number/m^3)
Viruses	0.02–0.3	—
Bacteria	0.3–10	0.5–1000
Fungal Spores	0.5–30	0–10,000
Pollen	10–100	0–1000

Figure 3: Number concentration and size of various primary bioaerosols in outdoor environments, adapted from Hinds (2012)

Bioparticles can be found in both indoor and outdoor environments through both natural and anthropogenic activities (Hinds (2012)). Natural activities for bioparticle generation outside include wind friction with surfaces which lofts various microorganisms into the air and the collision of ocean waves against cliffs, resulting in catapulting sea spray aerosols that contain various bioparticles into the atmosphere. Examples for anthropogenic sources for bioparticles are cooling towers, activities that involve the treatment of wastewater and agricultural processes such as harvesting and tilling. Indoor industrial manifacturing processes or human activities as simple as just talking and coughing are major sources of bioparticles.

The number concentration of these particles depends heavily on various parameters. For those that have their source of origin in plants it includes the plant type, the type of emitted particles but also on the specific location and season. Furthermore the current relative humidity also influences their number as growing humidity enhances the creation of airborne droplets to which bioparticles stick. In that sense precipitation events lead to a cleaning of the atmosphere from particles, including the bioparticles. For most types of biomaterial the time in the air is estimated to be in the range of less than a single day to multiple weeks (Despres et al. (2012)). The most important removal mechanic for airborne particles is the process of dry deposition which is determined by a particles aerodynamic diameter (defined as the diameter of a sphere with a density of 1 g/cm^3 that settles in the air at the same velocity of the particle in question Hinds (2012)). However most bioparticles showcase complex shapes and thus its possible for large differences in their physical and aerodynamic diameters (Conwell et al. (2001)). Precipitation is another process that allows cleaning of the atmosphere from particles, mostly for smaller ranged particles (0.1μm - 10μm).

In general their contribution to the total atmospheric aerosol number concentration is as low as 1% over marine regions and 2-3% in continental environments (Winiwarter et al. (2009)). However it's been shown that this number can go higher in regions of increased vegetation. In the work of Elbert et al. (2007) it is shown that in Amazonia (Brazil) contributions can rise up to 35% on average due to fungi providing a major source for primary bioparticles. For the bioparticles of the coarse mode (1) their contribution to atmospheric number and mass concentration can reach up to 30% above rural and urban regions and up to 80% above pristine rainforests (Fröhlich-Nowoisky et al. (2016)).

For the longest time the impact of bioparticles has been neglected due to the huge variations in number concentration and because global average number concentrations have been shown to be insignificant in comparison to non-biological aerosols. The intergovernmental Panel on Climate Change (IPCC) in 2001 (Metz et al. (2001)) listed the mass contribution (in teragramm) of primary bioparticles per year as 56 TG/yr while sea salt and mineral dust contributions were as high as 3340 Tg/yr and 2150 Tg/yr respectively. Other studies like the one conducted by Jaenicke (2005) have estimated the mass contribution of bioparticles to be up to 1000 Tg/yr. These discrepancies and the impact of bioparticles on the health of all living organisms on the planet has increased interest in this field in the last decades.

Their impact on health warrants special treatment as only a miniscule mass of bioparticles inhaled can already transmit various diseases. These inflicted health problems can be categorized into infectious diseases, respiratory symptoms (such as congestion, wheezing and asthma) and reactions to toxins and irritants.

In the following section I will go over the main representatives of primary bioparticles and their general properties (Tomasi et al. (2016)). Bioparticles can be categorized according to their size and whether they are living or non-living. In terms of size they can be as small as a few nanometers (viruses, bacteria) or as big as hundreds of micrometers (pollen, fungi, plant debris).

Viruses and bacteria are the most common representatives of small sized bioparticles. Viruses are parasytes that are typically in the size range of 20nm - 300nm and are often sticking to other particles or droplets. Viruses need a host cell to survive and reproduce and are therefore non-living particles due to their inability to survive on their own. Viruses can infect their host with various diseases and are transmitted through direct contact or through contaminated food and water. Bacteria consist of single cells and are in the size range of $(0.3\mu m - 10\mu m)$. Bacteria that transmit diseases are called pathogens. Typical examples for their transmitted diseases are tubercullosis and legionelosis. Their primary source is water and soil. A single gram of soil alone can carry up to 10^9 bacteria (Hinds (2012)).

Fungi and pollen are prime examples for larger sized bioparticles. Fungi are microorganisms with the most common known example being mushrooms. Fungi expell spores that serve for fertilize other fungi for the purpose of reproduction. This is similar to seed producing plants which expell pollen. The fungal spores can contain a range of allergens which are able to penetrate the human airways and cause respiratory problems. Fungi have a wide size range due to them appearing as single celled or multicellular organisms. They are primarily found in plantlife and soil. The primary purpose of fungi is the decomposition of organic waste and the recycling of minerals and carbon in our environment.

4.3 Pollen

Pollen will be treated separately in this section since this work focuses on the condensation activity of pollen samples from wind pollinated plants. Pollen primarily serve as a means for reproduction for all seed producing plants which include both flowering (Angiosperms) and non-flowering plantlife where the seeds grow inside cones (Gymnosperms). Pollen grains are micrometer sized primary bioparticles emitted by any types of seed producing plants. Pollen from flowering plants are also commonly called flower sperm.

4.3.1 Composition of Pollen

Pollen are formed at the male part of the respective plant species and contain the male plant DNA. A pollen grain consists of a hard outer layer called the exine which is made out of three layers and a thinner layer underneath, called the intine (Knut et al. (1989)). The exine's surface has various apertures which includes microchannels and germination pores. Furtheremore the exine consists of a variety of proteins, lipids and pigments while the intine consists of enzymes, polysaccharides and cellulose. Underneath the intine is a cytoplasmic core which inhabits the sperm cells containing pollen cytoplasm. These sperm cells are 1 or multiple vegetative cells and a single reproductive cell. The exine showcases a strong mechanical resistance which helps to protect the cytoplasmic core inside from water loss and heat. Once the pollen grain formation has been completed the grain's target is the female part, called the stigma of the same plant species. As the grain reaches the stigma it begins to absorb water and form a tube through the stigma where the grain travels through to reach the embryo sack where fertilization occurs. The resulting seeds produced contain embryos that receive nutrition to grow before they are able to germinate and grow into plants.

4.3.2 Pollination process

The pollination process is the basis for food production. Angiosperms include plants that produce fruit with common examples being wheat and corn, both important ingredients for many types of food we all eat everyday.

The grains can reach the female plant part in multiple ways. Seed producing plants can self-pollinate, meaning the produced pollen grain can fertilize the female part of the same plant to induce the growth of new seeds. Pollen grains can also leave their mother plant and travel to another plant of the same species where they fertilize the respective female plant part. This is called cross pollination and usually results in a stronger seed growth.

Cross pollination can happen through animals and insects or through wind currents. In former case the sticky grains latch to the fur of animals and insects that accidently rub their bodies against flowers. Bees are a main transport source for pollen as they spend the entire day collecting nectar from flowering plants, rubbing their bodies against the flowers in the process and unwillingly having grains latch onto their fur. Furthermore due to their protein content pollen grains represent an important food source for many insects who collect the grains for their offsprings. Plants that rely on insects and animals for the pollination process have a strong smell to attract them, are most often brightly coloured and easily stick to fur. Pollen grains can also be emitted by plants in large amounts, appearing as a powder-like substance and allow the wind to carry them. Plants that rely on wind for the pollination process are called anemophilous (wind-loving). The grains emitted by those plants are dry and light in order to ensure a longer residence time in the air. Since they don't rely on animals for transportation the plants producing them are without scent and dully coloured. Studies have shown that these grains can travel distances in the range of 100km - 1000km before being deposited (Schueler and Schlünzen (2006), Sofiev et al. (2006)) and are in the size range of 17μm - 58μm (Pope (2010), Bohrer et al. (2008)).

4.3.3 Concentration of Pollen in the atmosphere

Pollen can be found in both the free troposphere and the atmospheric boundary layer (Noh et al. (2012)). Like with any bioparticles the number concentration of Pollen depends on several factors. Depending on the plant type the emitted grains have different sizes, densities and shapes which affects their settling velocity and thus their residence time in the air (Diehl et al. (2001)). A plant's age and the availability for the plant to have access to nutrients also increases pollen emittance efficiency (Burge (1995)). Depending on how high pollen grains are transported in the atmosphere their residence time increases with increasing altitude. Meteorological factors also determine their number in the atmosphere. Temperature and relative humidity determine how well pollen grains are bonding with surfaces and how well they can be resuspended back into the air (Jones and Harrison (2004)). A rise in temperature may increase the distances pollen grains from anemophilous plants are able to travel (Kuparinen et al. (2009)).

Other factors include the wind speed and precipitation as both can have a significant influence on pollen counts (Ogden et al. (1969)). Lastly an important aspect that affects pollen counts is their seasonality. Pollen from each plant type follow a clear seasonal cycle. The seasons of pollination for each plant begins at a certain date where pollen grains are emitted in low numbers followed by the main pollination timeline where grain emittance reaches a maximum. The season concludes with a date where pollen production is stopped entirely. Many plants continue to produce pollen till the first frost fall, albeit at smaller numbers. These pollination seasons are locally predictable for many plant species due to peaks in observed pollen counts coinciding with flowering seasons (Tormo-Molina et al. (2010)). However for some species there are noticeable shifts between the flowering periods and the observed pollen counts due to resuspension of grains. Furthermore the expelled pollen number concentration can vary greatly from one year to another.

Climate change introduced a shift on pollen seasons as the increase in annual temperature and carbon dioxide concentrations results in many plants to start producing pollen earlier and in higher amounts. A higher pollen concentration means a higher fertilization rate but many pollen types carry allergens which can trigger diseases like hay fever and respiratory symptoms like asthma. If small enough some pollen grains can also deposit in the eyes and the Nasopharyngeal region. For example around 15,5% of the american population suffers from allergy to ragweed pollen (Paivi M et al. (2014)) (Climate Change Indicators: Ragweed Pollen Season, Epa.gov). Due to their health impact many pollen-monitoring programmes and networks have been developed in the recent decade to gain information on pollen number concentrations throughout the year in order to predict their behaviour for the future (Despres et al. (2012)). Furthermore meteorological changes introduced through climate change can also prolong the main pollination season of each plant type.

As with other bioparticles, both number and mass concentrations of Pollen in different regions can show large variations depending on the density of vegetation. It is thus only natural that regions with a high density of forests and plants will expell more pollen and other bioparticles than those with less so. Thus in such regions pollen could become a potentially important factor when researching atmospheric processes involving aerosols.

4.4 Pollen rupture

Pollen have shown the interesting ability to rupture when air humidity increases through direct contact with water, expelling a large amount of smaller fragments made of cytoplasm coming from their vegetative cell. These cytoplasm fragments have sizes in the range from several nanometers to several micrometers and are formed after just a few minutes of direct contact with water (Miguel et al. (2006), Taylor et al. (2004), Taylor et al. (2002)).

The major components of pollen cytoplasm are proteins and polymeric carbohydrates (Steiner et al. (2015), Laurence et al. (2011)). The main carbohydrate within the cytoplasm is Starch (Franchi et al. (1996)). Most larger pollen which are emitted by anemophilous plants contain such starch granules within their vegetative cell Baker and Baker (1979).These starch granules are defined as subpollen particles (SPP) (Steiner et al. (2015)) and after being expelled due to the rupture process, they form hygroscopically more active compounds like glucose, sucrose and pectins (Suphioglu et al. (1992)). With starch being the main representative within the expelled cytoplasm material, it is most likely that these components govern the condensation ability of the cytoplasm fragments, once they are suspended into the air (Mikhailov et al. (2019)). But in addition to Starch, pollen cytoplasm also contains a number of soluble compounds which could potentially coat themselves along the starch granules as thin films, increasing their water affinity and solubility (Pacini et al. (2006)) It is this soluble fraction of cytoplasm material which is analyzed in this work.

This pollen rupture is also defined as osmotic shock and describes the process of water entering the grain through the pores due to a difference between solute concentrations outside and inside the pollen exine. Pollen grains contain various substances inside them dissolved in water, therefore a solution with a certain amount of organic solute components and water being the solvent. If the outside humidity increases there will be a an increasing difference in solute concentration outside and inside the grains, causing the water to force itself through the exine pores in order to offset this difference in solute concentration. This in turn results in the swelling and eventual bursting of the intine layer (Matamoro-Vidal et al. (2016)), causing cytoplasmic content from the pollen nucleus to emerge through the exine apertures into the air.

The works of Taylor et al. (2004) and Taylor et al. (2002) investigated the number of released fragments from flowering birch and grass samples. These fragments consisted mainly of pollen cytoplasm and are small enough to reach the lower airways and trigger asthmatic responses. High air moisture levels in the atmosphere can thus lead to an increase in organic cytoplasm fragments that contain pollen allergens. Thunderstorms in seasons of high pollen concentrations are linked with asthma outbreaks from people suffering from pollen allergy (D'Amato et al. (2007)).

The rupture process can proceed directly inside both anglio- (flowers) and gymnosperms (non-flowering) as seen in the works of Miguel et al. (2006), Taylor et al. (2004) and Taylor et al. (2002) which investigated the release of smaller cytoplasm fragments by exposing catkin and flower samples to a controlled wetting and drying cycle before being dispersed through wind in a chamber where their number concentration was measured. It is also possible for the rupture process to occur after the pollen grains are emitted into the atmosphere, either rupturing due to increasing ambient humidity or by settling on surfaces and coming to direct contact with water. The work of Schaeppi et al. (1997) gives evidence for the latter, investigating the release and number of fragments containing the major allergen Bet v 1. Birch pollen does not rupture under high air humidities but the allergen Bet v 1 is still found in large quantities in the air, suggesting that the rupture process does not happen in the air but when Birch pollen grains are settled on various surfaces, rupturing during rainfall events and then becoming airborne again due to resuspension.

Pollen rupture can be an additional source of biogenic load in the atmosphere and introduce a discrepancy between the number of measured pollen grains and the actual amount of biomaterial containing alergenes. Wheter these cytoplasm fragments can influence the global number concentration and mass concentration of bioparticles depends on how much content is expelled from a single pollen grain during the rupture process. Additionally the factors that influence the number of produced and lifted pollen grains (plant type and atmospheric conditions) naturally also determines the amount of cytoplasm fragments in the air. With the temperature increase through climate change the main pollination seasons increase as well, allowing more pollen grains and thus more organic fragments to be released into the air.

In most studies there is no clear distinction between the soluble fraction and the unsoluble starch granules of the cytoplasm inside the pollen nucleus. They are both denounced as subparticles without clear distinction. The master thesis of Gratzl (2020) describes a new method to extract the cytoplasm content from a pollen grain and separating the soluble material from the starch granules. His work focuses on the investigation of SPP from 5 different plant species, the same species that are also analyzed in my work. The process behind this method involved applying high enough stress to the pollen walls with an instrument, called Mixer Mill (*Retsch MM 400*) in order for the walls to break and release both SPP and soluble material. The Mixer Mill was used on suspensions consisting of 0.5g pollen and 2ml Milli-Q water for each pollen type and after applying the nessecary stress with the Mixer, all resulting suspensions contained both intact and damaged pollen grains, as well as soluble material and SPP. With the usage of a filter paper (with filter size of $10\mu m$) both damaged and undamaged grains are removed. Afterwards the soluble material is extracted from the suspension by using a 50nm or 200 nm syringe filter. For each pollen type soluble material is extracted in 10ml suspensions and stored as sample solutions to use my work's measurement.

My work focuses specifically on the soluble cytoplasm material expelled from pollem grains of 6 different anemphilous plant types. These plant species are *Betula pendula* (Birch), *Phleum pratense* (Timothy grass), *Poa pratensis* (blue grass), *Corylus avellana* (Hazel), *Artemisia vulgaris* (Mugwort) and *Ambrosia artemisiifolia* (Ragweed). In the following section I will briefly go over their most common whereabouts and their importance.

4.5 Investigated pollen species

4.5.1 Betula pendula

Betula, or more Birch is a tree species with high abundance in Europe and represents the most important sources for allergens in the atmosphere from all tree types in northern Europe (DAmato et al. (2007)). The highest concentration of Birch can be found in Northern Europe (Beck et al. (2016)). There the flowering period of Birch starts from the second half of April with the peak number concentration of produced pollen starting around 1-3 weeks after (DAmato et al. (2007)). Their flowering periods are especially sensitive to variations in temperature with the pollination time increasing or decreasing up to 2 - 8 weeks.

4.5.2 Artemisia vulgaris

Grains produced from mugwort have diameters ranging from 10 to 25 μm (Halbritter1998). It often falls under the term wirmwoord and it is a perennial plant, a species that lives for more 2 years. In comparison to most anemophilous plants mugwort also attracts wildlife, making their pollination process not solely dependent on wind. Their flowering period starts in early July and goes till September. It is mostly spread around around all of Europe and throughout countries of northern Asia from Russia to Japan til Korea. Furtheremore this plant is often used as herbal medicine in Europe and Asia.

4.5.3 Ambrosia artemisiifolia

Ambrosia artemisiifolia, more commonly under the name Ragweed is a herbaceous plant with a flowering period that peaks in the months of April and May and then decreases until August (Kazinczi et al. (2008)). Ragweed has it's origin in North America but today it can be also found in many other countries in Europe. Ragweed is a main contributor to allergen distributions with the major allergens they carry being Amb a 1 and Amb a 11 Chen et al. (2018). They thus provide a major influence on the health of people suffering from pollen allergy during the main flowering season. The size of their expelled pollen can be as low as 15μm in diameter and as large as 25μm.

4.5.4 Corylus avellana

The name Corylus avellana refers to common Hazel, a multi-trunked shrub which differs from trees by it's smaller height. Pollen grains of common Hazel are in the size range of $26 - 50\mu m$ (Quelle). The flowering period of common Hazel starts in early spring. In Europe and the US Hazel is grown for the production of nuts.

4.5.5 Phleum pratense

They are also denounced as timothy grass and as most grass pollen they represent one of the most important allergen sources in the world. Major allergens within their grains include Phl p 5 and Phl p 1 (Behrendt et al. (1999)). Expelled pollen grains from the grass genus have sizes from 30 and to 50 μm in diameter. It's main pollination season lies in the months between June to September.

5 Clouds and droplet formation

5.1 Clouds

My work focuses on the ability of cytoplasm fragments of pollen to enable the formation of droplets, making them a potential influence on the formation of clouds. Thus it is important to discuss the properties and formation processes of clouds as well as a more exact description behind the thermodynamics of droplet development first. In general aerosol particles that arise from both natural and antropogenic sources are an important reason as to why clouds can form in the atmosphere. They provide the nessecary surface that allows water vapor to condensate and form droplets. When these droplets reach sizes of 10μm in diameter or larger they are defined as cloud droplets and particles that enable this process are defined as cloud condensation nuclei, in short CCN (Seinfeld and Spyros (2006)). If atmospheric temperatures are low enough some particles can also allow the accumulation and freezing of droplets on their surface. These are particles are called ice nuclei, in short IN.

Clouds are accumulations of liquid droplets or solid ice crystals in the atmosphere. They can be generally distinguished between warm clouds and cold clouds (Lohmann et al. (2016)). War clouds are defined as those with only liquid droplets while cold clouds consist solely of ice crystals. Sometimes a cloud is made of both liquid and solid components and it is then reffered as a cloud of mixed state. Often these cloud components are reffered to as hydrometeors to give them a general name independent of the cloud phase. The properties and vibisibility of clouds depends on the size, shape and number concentration of these hydrometeors. For clouds to be visible to the human eye the number concentrations of either crystals of droplets needs to be sufficiently high. Hydrometeors that reach sizes where the sedimentation velocity overwhelms the updraft force can participate in precipitation processes. My work focuses on the formation of droplets on bioparticles and therefore the topic of cold clouds or IN is not further discussed in here.

5.1.1 Mechanics behind the formation of a cloud

Generally clouds form if the atmosphere is in a supersaturated state. Supersaturation is commonly defined as any humidity value above 100% (We will later define this in a more precise way). The generation of a supersaturated environment in the atmosphere can be achieved in 2 ways. One way is by introducing more water vapor into the atmosphere, thus increasing the humidity level past the saturation point of 100%. The other way is by cooling the air, which in turn decreases the saturation point and since this does not affect the current amount of water vapor in the atmosphere, this will lead to a humidity value above saturation (Abbott et al. (2009)). It is common in atmospheric science, when talking about processes in the atmosphere to define a large mass of air as an air parcel for easier imagination. Such cooling as previously mentioned can be achieved by the air parcel moving over colder surfaces or mixing of multiple air parcels of different temperatures.

However most visible clouds are formed due to the lifting process, also often defined as adiabatic cooling. For that the concept of an air parcel is used to better understand this general cloud formation process. An air parcel is defined as a block of air with it's own temperature and density different from the surrounding air. If such a parcel has a higher temperature than it's surrounding atmosphere it starts to rise due to the byoyancy effect. The higher temperature results in a stronger brownian motion of the air molecules which yields in an expansion of the parcel's volume. According to Boyle's law for ideal gases the volume is indirectly proportional to the pressure and due to this decrease in pressure the air parcel begins to rise. Such formation of warm air parcels can happen through the uneven distribution of sunlight over the surface, resulting in some spots receiving more heat than others. When the formation of a warm and moist parcel happens at the surface it is also often called a thermal.

This rise in altitude continues till the air parcel's pressure equals the surrounding atmospheric pressure. The parcel's temperature also drops with increasing height as it uses up internal energy for the volume expansion. At a certain point the temperature reaches the parcel's dew point, meaning the point where the parcel's moisture content has reached a relative humidity of 100%. Any further drop in temperature results in the parcel being in a supersaturated state which is needed for the formation of droplets, the liquid particles that make up a warm cloud.

The value of the supersaturation the air parcel can achieve is determined by it's updraft velocity, the velocity of it's vertical rise in altitude due to the byoyancy effect. Lands have a smaller heat capacity which means less heat is needed to rise in temperature. This in turn results in land masses heating up more quickly than oceans which causes higher updraft velocities and therefore higher supersaturations (Seinfeld and Spyros (2006)). Higher supersaturations mean that more particles will be able to grow into droplets over land surfaces than over oceans.

5.1.2 Importance for atmosphere and energy budget

Clouds have a substantial influence on our planet's radiative balance and it is therefore a goal in many climate models to estimate how their properties influence their forcing effect (Houghton et al. (2001), Lachlan-Cope (2010)). Their ability to reflect incoming shortwave radiation emitted from the sun results in a cooling effect for the earth's atmosphere and surface. They are also able to absorb incoming longwave thermal radiation emitted from the earth's surface and therefore trap it from leaving the earth's atmosphere.

Depending on the cloud's type, altitude and cover the resulting net effect of both processes can be that of cooling or heating the earth's climate system. Their annual and global mean net effect on our climate is around $-21.1 W m^{-2}$ (Lohmann et al. (2016)). Their cooling effect stands in competition to the warming effect that greenhouse gases have on the raditaive balance. Clouds are an important component in the planet's hydrological cycle, enabling water to travel from the atmosphere back to the surface in the form of precipitation and snow. The falling droplets or ice crystals reduce the number of airborne particles and soluble gases, cleaning the air. Clouds can be categorized even further according to their macroscopic and microscopic properties.

5.1.3 Macroscopic properties

On a macroscopic viewpoint clouds are grouped into 3 main types: *cumulus*, *stratus* and *cirrus*. Branches from these clouds are further divided into multiple species which makes a total of 10 different cloud types defined by the International Cloud Atlas WMO. Further specifications classify those types according to their level of altitude, meaning the height of the cloud base above mean sea level.

Cumulus clouds charaterize themselves through their fluffy appearance and their tower-like shape that extends more into the vertical direction than in the horizontal direction. They are formed mainly due to the process called convection where warm parcels of air rise in the vertical direction before the adiabatic cooling process initiates cloud formation. Therefore they are also often reffered to as convective clouds. Cumulus clouds appear mostly in mid to low altitudes (between 6,500 and 20,000 feet altitude).

Just as cumulus clouds, clouds of stratus type appear in low atmospheric levels. They re mostly characterizes by their flat and featureless appearance, along with colours that range from darker gray to almost white. Status clouds develop vertically and can produce light drizzle but produce no heavy precipitation events. Both cumulus and stratus types of clouds can contain solely hydrometeors in liquid and solid form, or even appear in mixed states.

Cirrus clouds develop in the highest layers of the troposphere. They consist purely of ice crystals and their appearance is hair- or feather-like, almost transparent due to their low number of ice crystals within. They develop mostly in the horizontal direction and showcase a bright white colour. They have the ability to disperse incoming sun radiations which results in the formation of a halo.

5.1.4 Microscopic properties

The microphysical properties of a cloud refers to the size, shape and number concentration of cloud hydrometeors. Furtheremore their phase determines wheter they form a warm, cold or a cloud of mixed phase. The properties of the formed droplets of a warm cloud are determined by the number and size of particles which can serve as CCN. For a fixed moisture level in the atmosphere an increase in the CCN concentration leads to a higher number of formed droplets. This increases a cloud's albedo, the amount of incoming solar radiation reflected back into space vs the fraction of solar radiation that gets transmitted to the earth's surface (Lohmann and Feichter (2005), Twomey (1977)). At the same time for a high CCN number concentration there will be more competition for water vapor, surpressing condensational growth of the individual droplets and decreasing precipitation efficiency. Cloud droplets are typically in the size range of 2 - 25 μm while drizzle drops are those defined in the size range 25 - 250 μm (Lohmann et al. (2016)). To become part of rain the droplets need to reach diameter values of a few millimeters. When there is competition for water vapor the individual droplet growth takes longer, making precitipation events more scarce.

On the other hand this reduced precipitation efficiency increases a cloud's lifetime, the time from the cloud's formation till it's desintegration due to precipitation. For a small number of CCN in the air droplet's will grow more quickly to sizes nessecary for precipitation.

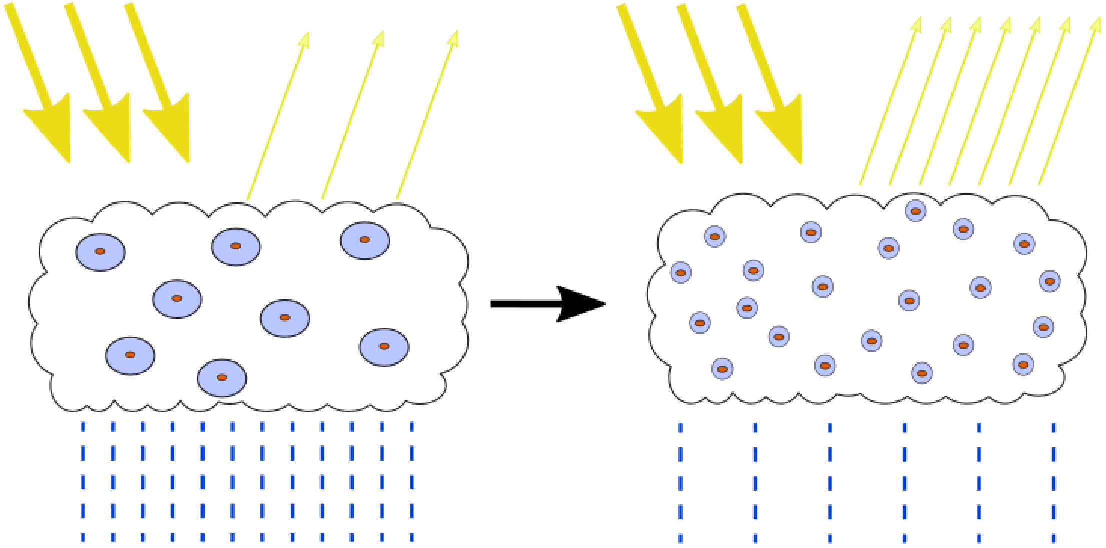

Figure 4: Influence of increased CCN concentration on cloud albedo

For a comparison the cumulus clouds over continental regions can reach cloud droplet number concentrations up to 950 cm^{-1} while over marine regions higher number concentrations than 200 cm^{-1} are rarely reached (Lohmann et al. (2016)). In general an increase in altitude corresponds to a decrease in number concentrations of aerosol particles which of course results in a decrease of the number of available active CCN. Adding to this the procentual decrease in water vapor with increasing height, clouds at the top consist of only a few and smaller droplets.

5.2 Droplet formation

Wheter an airborne aerosol particle can enable condensation of water vapor and grow into a cloud droplet depends on it's size, chemical composition and the current ambient saturation ratio S around the particle (Lohmann et al. (2016), Andreae and Rosenfeld (2008), Seinfeld and Spyros (2006), McFiggans et al. (2006)). For a liquid-vapor system the saturation ratio S is defined as the ratio of the current vapor pressure p and the saturation vapor pressure p_s over a flat surface of pure water. The vapor pressure of water p is denoted as the pressure the gaseous phase exerts on it's liquid phase. With a rising number of vapor molecules the vapor pressure increases. At a certain vapor pressure value the number of water molecules that evaporate equal the number of condensating water molecules. The gaseous phase of water is in equilibrium with it's liquid phase and that pressure point is defined as the saturation vapor pressure p_s.

$$S = \frac{p}{p_s} \qquad RH = S * 100\% \qquad SS = (S-1) * 100\% \tag{1}$$

A value of 1 for S indicates equilibrium for the system, the vapor pressure p is equal to the saturation vapor pressure p_s. Values below or above 1 mean that the atmosphere is either in a subsaturated or supersaturated state. Multiplying S with 100% yields the relative humidity RH which is the most common way to describe the procentual amount of water vapor in the air. Substracting S with 1 and multiplying with 100% afterwards gives us the procentual amount of supersaturation, denoted with SS.

5.2.1 Thermodynamics of liquid-vapor systems

In the field of themodynamics the goal is to describe systems of large particle numbers through macroscopic properties such as volume or internal energy, also called state variables. Such a system is in a state of thermodynamic equilibrium (TE) when external conditions remain unchanged and thus the state variables are constant in time. Any isolated system reaches the point of equilibrium after a certain amount of time. TE is described through minima of thermodynamic potentials. Those include the Helmholtz Free Energy F, the Gibbs Free energy G and the Enthalpy H. For an atmospheric system at constant pressure P and temperature T equilibrium between the liquid and gas phase can be shown through the absolute minimum of the Gibbs Free Energy (2).

$$G(T, P, N) = U + P \cdot V - T \cdot S \tag{2}$$

Here S denotes the system's entropy, not the previously defined saturation ratio. The other thermodynamic potentials can also be used to describe closed systems at equilibrium. However atmospheric processes happen mostly at constant pressure and temperature values and therefore the Gibbs Free energy G is used. Formulating the mimimum principle for G it can be further shown that at thermodynamic equilibrium the chemical potentials (which is simply the Gibbs free energy per particle) of both phases must equal each other (3-5).

$$dG = -S \cdot dT + V \cdot dP + \mu \cdot dN \tag{3}$$

$$dG = 0 \quad at \quad P = const., T = const. \ (dP = 0, dT = 0) \quad \rightarrow \quad dG = \mu \cdot dN \tag{4}$$

$$dG = \mu_l \cdot dN_l + \mu_v \cdot dN_v \quad \rightarrow \quad dN_l = -dN_v \quad \rightarrow \quad dG = dN_l \cdot (\mu_l - \mu_v) \tag{5}$$

$$\mu_v - \mu_l = k \cdot T \cdot ln(S) \tag{6}$$

Equation 3 shows the total differential of the Gibbs Free Energy, interpreted as an infitisemal change of G. At equilibrium G reaches it's minimum and doesn't fluctuate anymore. Since the temperature T and pressure P are held constant the infitisemal change dG only depends on the chemical potential μ and the change in molecule number dN (4). As mentioned before, evaporation and condensation happen simultanously at any time so the both phases experience a change dN_l and dN_v (l for liquid and v for vapor) in their molecule number. At the point of equilibrium the change in vapor molecules must be equal to the change in liquid molecule (5).

The phase with the higher chemical unstable and phase transition into the respective direction. If $\mu_v > \mu_l$ the gaseous phase is in an unstable state, which is realized through supersaturation and wants to initiate condensation to reduce it's vapor pressure to reach the point of equilibrium again. The reverse is happening if $\mu_l > \mu_v$ with evaporation being desired by the system to reach thermodynamic equilibrium again.

From Wendisch (1999) equation 6 can be derived to gain an relation between the chemical potentials of both phases and the system's saturation ratio S. In the case of $\mu_v > \mu_l$ where the systems prefers to condensate for a phase transition S needs to be bigger than 1 in order for the left hand term to be positive. Evaporation of the system is favoured at $\mu_l > \mu_v$ for S < 1, the system is in a subsaturated state with the liquid phase being unstable. Equation 6 gives a direct link between the ambient saturation ratio S and what that indicates for the Gibbs Free Energies of both phases.

If the temperature of the system doesn't remain constant and changes equilibrium between the 2 phases is temporarily abolished. Only once the temperature settles at a constant value thermodynamic equilibrium will be reached again after some time. A rise in temperature results in more water molecules at a liquid's surface gain enough energy to overcome the surface tension and escape into the gaseous phase of the atmosphere. The evaporation rate rises but since every thermodynamic system craves for equilibrium, in time the condensation rate rises too in order to compensante for the higher number of evaporated water molecules. At the new equilibrium point more water molecules are in the atmosphere indicating a higher pressure on it's liquid phase on the surface. The equilibrium point of vapor pressure grows with rising temperature. This relation between temperature T and saturation vapor pressure p_S is shown through the Clausius Clapeyron equation (7).

$$S = \frac{dp_s}{dT} = \frac{\Delta H(T) \cdot M_w}{T \cdot (v_v - v_l)} \tag{7}$$

The Clausius Clapeyron equation describes the slope of the saturation vapor pressure p_s per unit change of temperature T. M_w is the molecular weight of water, ΔH is the nessecary latent heat for the evaporation of water while v_v and v_l are respectively the molar volumes of liquid and vapor of water.

5.2.2 Homogenous nucleation

From the difference in chemical potentials of the 2 phases the direction of the phase transition can be specified.

Another way to find out the relation between the 2 phases is to plot the Gibbs Free energy of a substance as a function of the substance's occupied volume.

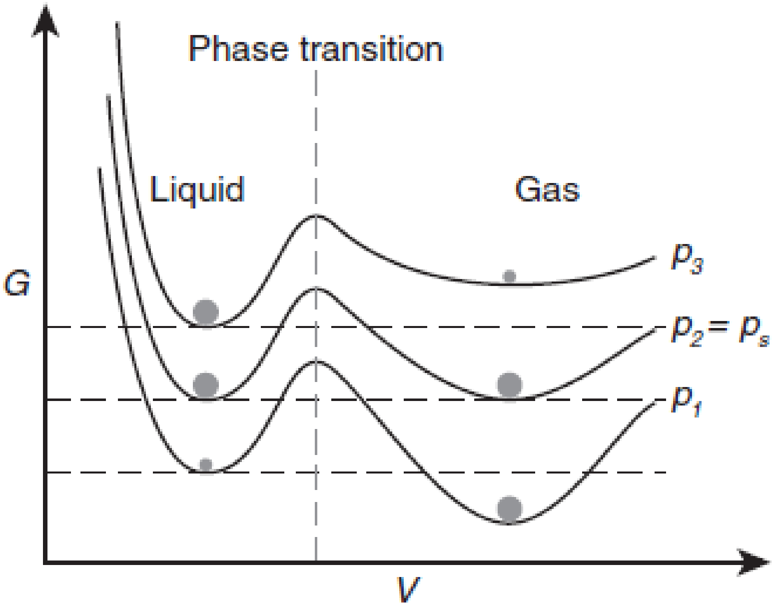

Figure 5: Gibbs free energy of a substance as a function of the volume of the substance for 3 pressure values. Graph from Lohmann et al. (2016)

Figure 5 gives a graphical representation of the Gibbs free energy of a substance as function of it's volume. For each vapor pressure value 2 minima of G can be seen, one for each phase. The phase with the lower minimum is the state the system desires to be in. For the pressure value p_1 the liquid phase is in an unstable phase, with it's Gibbs minimum higher than the vapor minimum. The system prefers to condensate in order to reach thermodynamic equilibrium between vapor and liquid. At p_2 both minima equal each other, indicating that both phases are in equilibrium with each other. At vapor pressure p_3, which is above the saturation vapor pressure p_s the Gibbs minimum of the liquid phase is below the minimum of the vapor phase. The vapor phase is in an unstable phase and wishes to condense to it's liquid phase.

The dotted line seperates both phases and denotes a maximum value of the Gibbs energy that has to be overcome in order for the phase change (no matter the direction) to happen. This energy barrier is common for phase transitions of 1st order. Evaporation and condensation are examples of such phase changes of 1st order.

Most phase transitions of 1st order are possible due to a process called nucleation. The theory behind it describes the formation of microscopic spherical clusters or droplet embryos. This allows for a lower free energy barrier to overcome because the nucleation happens gradually and doesn't involve the entire substance joining the new phase uniformly. The nessecary work ΔG_i for the formation of a nanometer-sized cluster of i molecules is defined as the difference between the Gibbs free energy of the cluster G_i itself and the Gibbs free energy of the number of vapor molecules not in cluster form $i \cdot \mu_v$ (8).

$$\Delta G_i = G_i - i \cdot \mu_v \;\; with \;\; G_i = A_i \cdot \sigma + i \cdot \mu_l \;\; (capillary\ approximation) \tag{8}$$

$$\Delta G_i = 4 \cdot \pi \cdot \sigma \cdot r_i^2 - \frac{4 \cdot \pi}{3} \cdot n_L \cdot r_i^3 \cdot k \cdot T \cdot ln(S) \tag{9}$$

An expression for ΔG_i can be derived consisting of a volumetric and surface term (9). ΔG_i is the energy barrier a nanometer sized cluster of i vapor molecules has to conquer in order to be considered a stable droplet that is in equilibrium with it's environment, meaning that it is unlikely to evaporate as soon as being formed. To compare with figure 3, ΔG_i is the point of interception between the dotted line and the graph for each pressure. Here σ is the surface tension of the droplet and n_L is the molar number density of the liquid.

If there are no particles in the air then the nucleation process is defined as homogenous. The nanometer sized droplet embryos form by accumulation and collision of water vapor molecules if the surrounding saturation ratio S is high enough to overcome the energy barrier ΔG. These small clusters already belong to the liquid phase.

5.2.3 Kelvin

Calculating the first derivative of ΔG_i with respect to the droplet radius r_i and setting it zero results in an expression that presents the particle saturation ratio $\frac{p_{sc}}{p_s}$ over a curved surface as a function of the droplet diameter D_w. Here p_{sc} denounces the saturation vapor pressure over the curved droplet surface. The Boltzmann constant has been replaced with $\frac{R}{N_A}$ where R is the universal gas constant and N_A the Avogrado number. The number density n_L has been replaced with the equivalent expression $\frac{N_A}{M_w} \cdot p_w$ with M_w and p_w being the molar mass and density of pure water.

$$S_c = \frac{p_{sc}}{p_s} = exp\left(\frac{4 \cdot \sigma_w \cdot M_w}{R \cdot T \cdot p_w \cdot D_w}\right) \quad \rightarrow \quad p_{sc} = p_s \cdot exp\left(\frac{4 \cdot \sigma_w \cdot M_w}{R \cdot T \cdot p_w \cdot D_w}\right) \tag{10}$$

The above equation is called Kelvin. The index i has been dropped to indicate the droplet formation out of any number of vapor molecules. The droplet diameter is just 2 times the radius. In it's form to the right this equation states that the saturation vapor pressure over a curved surface of pure water p_{sc} is always higher than the saturation vapor pressure over a flat surface of pure water p_s. The index c on S_c implies curvature. σ_w is the surface tension of pure water.

In terms of the classical nucleation theory the Kelvin equation shows the relation between the size of a microscopic droplet and the nessecary droplet saturation ratio S_c it needs to have to be in equilibrium with it's surroundings. Lower values for D_w mean higher droplet saturation ratios S_c. In order for a cluster of diameter D_w to be in equilibrium with it's surrounding atmosphere the saturation ratio of the cluster $S_c = \frac{p_{sc}}{p_s}$ needs to be equal to the ambient saturation ratio $S = \frac{p}{p_s}$. This is the case when p = p_{sc}Therefore $\frac{p_{sc}}{p_s}$ can be exchanged with $\frac{p}{p_s}$ to give a direct relation between the droplet diameter D_w and the nessecary ambient saturation ratio S. Furthermore σ_w is replaced with σ_{sol} to account for the case of the droplet containing impurities (The number and amount of impurities in a droplet also influences the nessecary saturation ratio to be in equilibrium. This effect is called Raoult and will be explained a bit later).

$$S = exp\left(\frac{A}{d_w}\right) \qquad with \quad A = \frac{4 \cdot \sigma_{sol} \cdot M_w}{R \cdot T \cdot p_w} \tag{11}$$

The higher saturation vapor pressure over a curved surface can be explained due to the fact that the number of bonds water molecules can form on a curved surface is much smaller than on a flat surface, resulting in a weaker surface tension. Therefore surface molecules are much more likely to escape into the vapor phase, resulting in a higher vapor pressure. To reach equilibrium over the curved surface the number of molecules getting back to the liquid must also rise in order for both evaporation and condensation rate to equal each other.

The microscopic clusters formed from homogenous nucelation exhibit such a small radius that according to the Kelvin equation the nessecary ambient saturation ratio S for their coexistence with the vapor phase is very high, the corresponding supersaturation being of several hundred percent (Pruppacher and Klett (2010), Andreae and Rosenfeld (2008)).

5.2.4 Heterogenous nucleation

In the presence of airborne particles the corresponding nucleation process to initiate cluster formation is called heterogenous. Water vapor molecules accumulate on the surfaces of seed particles. The presence of particle surfaces facilitates the nucleation process, lowering the Gibbs Free energy barrier that needs to be overcomed for phase transition. Heterogenous nucleation also eliminates the possibility for homogenous nucleation to occur. A lower energy barrier means that lower saturation ratios are enough for vapor molecules to accumulate and form clusters. This in turn means a reduction of water in the vapor phase, lowering the atmospheric saturation ratio and therefore a supersaturation needed for homogenous nucleation cannot be reached.

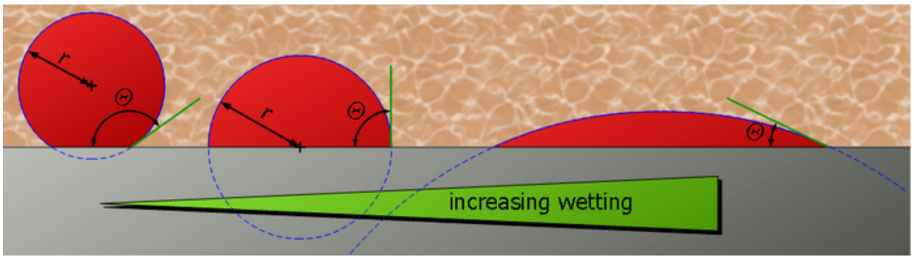

Figure 6: contact angle with increasing wettability. Digital Image. *Heterogenous Nucleation*. 28 May 2018. URL: tec-science.com/material-science/solidification-of-metals/heterogeneous-nucleation/

The contact angle between a vapor molecule and the particle surface determines how much the free energy barrier can be reduced. With growing wettability of a particle the contact angle θ descreases further. The Gibbs energy barrier for hetergoneous nucleation can be written as

$$\Delta G = \Delta G_{hom} \cdot f(cos(\theta), \frac{r^*}{r}) \tag{12}$$

r is the radius of the approaching spherical water cluster while r^* is the radius of the particle. Fletcher theory introduces an f factor that takes on values between 0 and 1. A larger ratio $\frac{r^*}{r}$ and smaller contact angle θ decreases the f factor which results in a reduction of the Gibbs barrier.

The contact angle depends on a particle's wettability, the ability to adsorb water. With rising wettability the contact angle decreases. Wettability is the main factor that determines the water uptake for insoluble particles (McFiggans et al. (2006)). For such particles the amount of water adsorbed can also be increased through the presense of soluble gases in the atmosphere (Sulfuric Acid). Heterogenous nucleation plays a foremost role in the formation of ice crystals and droplet initiation on insoluble particles.

Heterogenous nucleation cannot happen simultanously with homogenous nucleation. The presence of particles in the atmosphere allows water vapor to condense before the supersaturation can reach the nessecary high values needed for homogenous nucleation to be initiated.

5.2.5 Deliquescence and hygroscopic growth

Most airborne particles contain a number of soluble components. Those dissolve in water and form solution droplets already under subsaturated conditions. This process of droplet formation in a subsaturated environment is defined as deliquescence (Lohmann et al. (2016)). The RH value where this phase transition from solid to liquid occurs is called the deliquescence relative humidity (DRH). In comparison the formation of droplet embryos due to nucleation requires a supersaturated environment. The Kelvin equation which has been derived from the nucleation theory applies to any droplet, no matter the type of phase change. Most particles in the atmosphere exhibit some soluble components in their chemical composition and thus don't require a nucleation process to initiate droplet formation.

After reaching the DRH point the droplet takes up more water with a rising saturation ratio S. The growth factor describes how much the liquid particle grew in size at a certain RH value. It is defined as the ratio of the particle radius at a specific RH value and the radius at a RH value of 0%. The DRH point of a particle decreases when a particle has more soluble components or

the solube components themselves are more hydrophilic. The lower the DHR of a particle the larger the following water uptake under sabsaturated conditions and the bigger the resulting droplet. Furthermore an increasing particle radius decreases the DRH point even further. This can be explained due to the Kelvin equation. The dissolve solution droplet needs a certain ambient saturation ratio in order to be in equilibrium with it's surroundings. As the point of DRH gets smaller the growth factor gets larger.

The advantage of deliquescence is the lack of an energy barrier for the inititation of a new phase. Already at RH values below the DHR point soluble solid particles adsorb monolayers of water molecules at their surfaces, forming a so called quasi-liquid layer (QLL). This QLL causes a reduction in the surface energy of the particle. In comparison to nucleation where the new phase has to be initiated within the unstable parent phase here the reduction in surface tension eliminates the energy barrier.

5.2.6 Raoult's law

Raoult's law describes how the saturation vapor pressure over a flat surface of pure water changes when soluble components are dissolved in it. For an ideal solution (solutions where the bonds between water and solute molecules are of equal strength) Raoult's law can be described by the following equation (Lohmann, U. 2016).

$$\frac{p_{s,sol}}{p_s} = \frac{n_w}{n_w + n_s} = a_w \quad \rightarrow \quad p_{sol} = p_s \cdot \frac{n_w}{n_w + n_s} \tag{13}$$

Here $p_{s,sol}$ is the saturation vapor pressure over a flat surface of water containing n_w number of water molecules and n_s number of solute molecules. p_s is as before the saturation vapor pressure over a flat surface of pure water. The right hand term shows that the saturation vapor pressure over a solution is always lower than over a pure water surface. It is the opposite effect of Kelvin.

This reduction of the saturation vapor pressure over a solution can be explained due to the reduced evaporation rate. The solute molecules are evenly distributed in water and some of them will be placed at the surface. Thus less water molecules will be able to sit at the surface which results in the flux of water molecules per unit time towards the gas phase being smaller than for pure water. With more solution components added even less space at the surface can be reserved for water molecules, decreasing the evaporation rate even further. A decrease in evaporation is met with a decrease in condensation to reach equilibrium again. The saturation vapor pressure has been lowered. Furthermore some soluble elements can cause strong bonds with the water molecules, surpassing the hydrogen bonds.

For dilute solution droplets the Rault equation above can be further changed. The total mass m_{tot} of a solution droplet is the sum of the mass of the solute m and the mass of water m_w. But for highly dilute solutions the solute mass can be neglected and the total mass of the droplet is $m_{tot} \approx m_w = \frac{4}{3} \cdot \pi \cdot r^3 \cdot p_w$. Here p_w is the density of water and $r = \frac{D_w}{2}$ is the droplet radius. Furthermore the number of solute molecules n_s in a solute mass m_s can be expressed as $n_s = \frac{i \cdot N_A \cdot m_s}{M_s}$. Here N_A indicates the Avogadro's number (The number of particles in 1 mol of that same substance) while M_s is the molecular weight of the solute. i is the Van't Hoff factor and indicates the number of ions the solute produces per unit of solution. For a dilute $(NH_4)SO_2$ salt solution and assuming ideal solution behaviour and complete dissociation (Rose et al. (2008)) this factor equals 3. Using these approximations the Rault term can be changed further (Lohmann et al. (2016)).

$$\frac{p_{s,sol}}{p_s} = 1 - \frac{B}{D_w^3} \qquad with \;\; B = \frac{i \cdot 6 \cdot m_s \cdot M_w}{4 \cdot \pi \cdot M_s \cdot p_l} \tag{14}$$

Now the reduction in vapor pressure over a solution is directly linked to the amount of solute mass m_s. A smaller particle radius r increases the Raoult effect on the saturation vapor pressure but it also increases the Kelvin effect due to the higher surface to volume ratio. An increase in the radius means that the droplet needs only a smaller saturation ratio due to Kelvin influence but the effect of the solute decreases as the droplet becomes more dilute.

As in the section detailing the Kelvin term the saturation ratio $\frac{p_{s,sol}}{p_s}$ can be replaced with the saturation ratio $\frac{p}{p_s}$. The solution droplet is in stable equilibrium with it's environment if the current ambient vapor pressure p is equal to the saturation vapor pressure $p_{s,sol}$ over it's curved surface. Here we only looked at the influence of Raoult on the nessecary S value for equilibrium. In the next section we see how the combined influence of both Raoult and Kelvin impacts the saturation ratio S that the droplet needs to be in stable equilibrium.

5.2.7 Koehler equation

Combining both Rault's law and the Kelvin effect yields the Koehler equation which describes the pathway that a tiny dilute solution droplet has to take in order become a micrometer sized cloud droplet. This equarion gives us the relation between a solution droplet's size, the chemical composition and size of it's seed particle and nessecary saturation ratio S value it needs to have to be in thermal equilibrium with the ambient water vapor. The graphical representation of the Koehler equation is called the Koehler curve. Every particle with different size and chemical composition has a different Koehler curve.

$$\frac{p_{sol,sc}}{p_s} = \frac{p_{sol,sc}}{p_{sc}} \cdot \frac{p_{sc}}{p_s} = \left(1 - \frac{B}{D_w^3}\right) \cdot exp\left(\frac{A}{D_w}\right) \tag{15}$$

Here $p_{sol,sc}$ is the saturation vapor pressure over a curved surface with a certain amount of solute while p_{sc} is just the saturation vapor pressure over a curved surface of pure water. p_s is as usual the equilibrium vapor pressure over a flat surface of pure water and D_w is the diameter of the solution droplet. For small $\frac{A}{D_w}$ the Kelvin term can be approximated with a Taylor expansion.

$$\frac{p_{sol,c}}{p_s} = \frac{p}{p_s} = S = 1 + \frac{A}{D_w} - \frac{B}{D_w^3} \tag{16}$$

The ambient vapor pressure p needs to be equal to the saturation vapor pressure $p_{sol,sc}$ over a solution droplet in order for said droplet to be in equilibrium with the atmosphere. Figure 7 shows the Koehler curve for a solution droplet with the solute itself being a Ammoniumsulphat particle with dry diameter D_s of 40 nm. The x axis corresponds to the droplet diameter and the y axis is the procentual amount of supersaturation SS where the intersection with the x axis (y = 0) corresponds to the saturation ratio S = 1 (equilibrium) and any value above 0 indicates supersaturation.

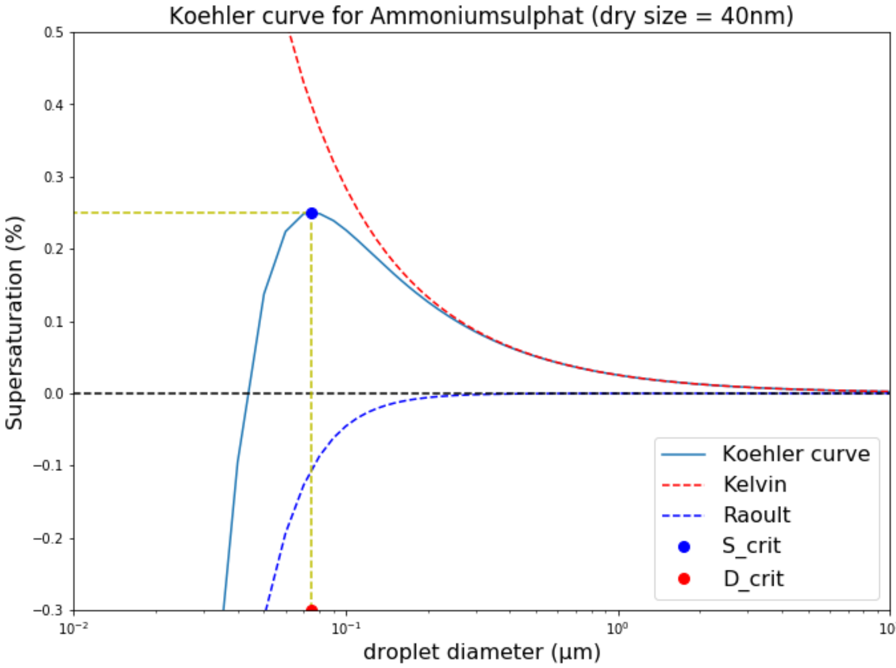

Figure 7: Koehler curves for an $(NH_4)SO_2$ particle with dry diameter of 40 nm

The ascending branch of the Koehler curve describes the hygroscopic growth of a solution droplet while being in stable equilibrium with it's surroundings. For any point on the acending branch the curve shows the nessecary ambient saturatio ratio S the solution droplet needs to have to be in such equilibrium and not evaporate automatically. It's important to note that the Koehler curve doesn't provide any history on the process the particle has to take to become liquid. It merely shows the water uptake process and the nessecary saturation ratios it needs for that but provides no information on the actual phase transition from solid to liquid.

Through spontanous coagulation the droplet can reach a higher diameter value without any increase in saturation ratio, puhing it to the right. In that case the doplet jumps to the corresponding point on the Koehler curve where the new diameter on the x-axis corresponds to the SS value it needs to have for equilibrium. On the other hand, vapor molecules can also spontanously escape the droplet's surface, rendering it with a smaller diameter and forcing it to jump to a previous point on the Koehler trajectory that corresponds to that size.

Figure 7 also shows both the Raoult and the Kelvin equation plotted individually as a function of the droplet diameter (red and blue dotted line). Their combination yields in a trajectory with a distinct maximum. That maximum is denoted as the critical supersaturation SS_{crit} which corresponds to a critical droplet diameter $D_{w,crit}$ on the x axis. The critical supersaturation SS_{crit} naturally corresponds to a critical saturation ratio S_{crit}. At that point the droplet is said to have been activated and is is that point that the droplet needs to reach in order to grow further and reach micrometer size or even bigger. The solution droplet ceazes to be in equilibrium and from that point on grows uncontrollably. In theory the solution droplet can then grow forever as the saturation ratio S does not need to be increased for further growth. The descending path of the Koehler curve function as a sort of boundary. For any point along the descending trajectory if the saturarion ratio S has a value beneath it, then the solution droplet will fall onto the corresponding point of the acending branch, meaning it will evaporate till it reaches that size.

The most important aspect of the curve is to understand that a particle of given size and number of chemical constituents can only reach this critical point if it's critical supersaturation value is below the ambient level of supersaturation. Particles that don't reach this requirement will only grow along the ascending branch until reaching the point on the y axis that corresponds to the atmospheric supersaturation.

$$D_{w,crit} = \left(\frac{3 \cdot B}{A}\right)^{(1/2)} \qquad SS_{crit} = \left(\left(\frac{4 \cdot A^3}{27 \cdot B}\right)^{(1/2)} - 1\right) \cdot 100\% \tag{17}$$

The above expressions for $D_{w,crit}$ and SS_{crit} are gained by differentiating the Koehler equation from (16) with respect to droplet diameter D_w and setting the derivating to zero which is the common way to find the maximum value of a function.

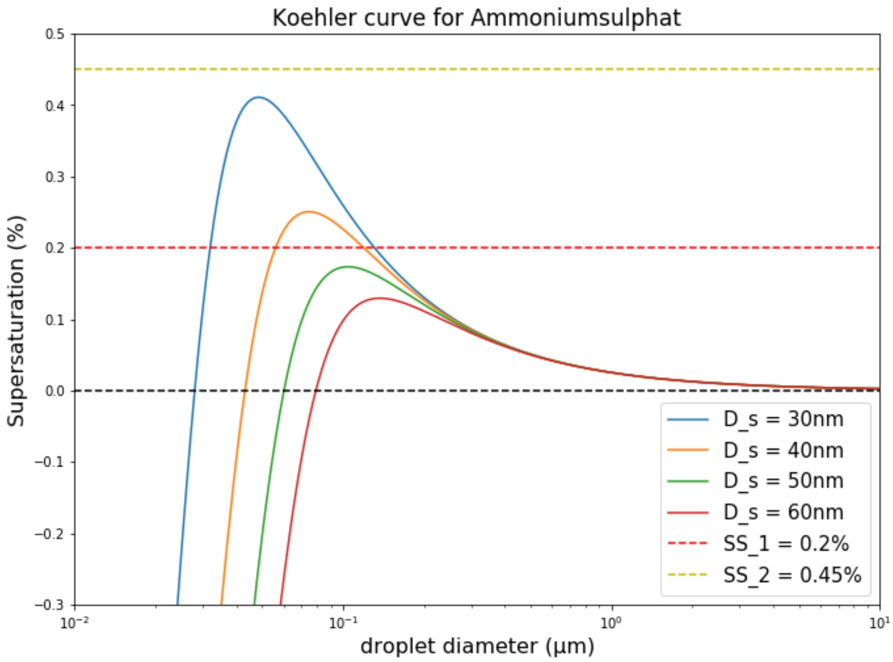

Figure 8: Koehlers curve for Ammoniumsulphat with a multiple dry diameter values

Figure 8 shows how a variation in the dry diameter D_s changes the resulting Koehler curve. The variation in dry diameter noticaebly influences the acending branch and the critical point of the curve. Afterwards their descending trajectories all all fall into the same line as they growth in size. This is because the Raoult term dominates in the first section of the curve due to the D_w^3 in the denominator. The dry diameter D_s is also only inside the Raoult term and therefore a variation in D_s only changes this first section of the curve. The droplet continues to grow due to water uptake and becomes more dilute, the influence of Rault gets smaller and the Kelvin effect begins to takes over dominance.

From figure 8 it can be seen that the Ammoniumsulphat particle with the smallest dry radius ($D_s = 30$nm) showcases the highest value for SS_{crit}. A smaller dry diameters corresponds to a smaller particle size which means a lower amount of solute in the droplet. A decrease in solute indicates a weaker Raoult influence. A higher dry diameter indicates an increase of solute which means that the the critical point gets lowered further. For dry sizes large enough the critical point SS_{crit} can even be underneath 0, meaning the particle doesn't even need supersaturation to activate into a cloud droplet.

Figure 8 also shows 2 different ambient saturation ratios and what those mean for the hygroscopic growth of an Ammoniumsulphat particle of given dry size. The SS_1 line (red dotted) indicates a certain supersaturation level of 0.2% while the SS_2 (yellow dotted) line indicates an ambient supersaturation of 0.45%. If we follow the Koehler curve of particle with $D_s = 40$nm (orange line) it is easy to see that the particle would be able to reach the critical point and grow further if the ambient supersaturation would be equal to SS_2. However if the ambient amount of supersaturation had a value of SS_1 then the solution droplet only grows along the equilibrium path till it reaches the point where the curve intersects with the SS_1 line. For further growth a higher ambient supersaturation level would be needed and only then water can be continued.

There are multiple Koehler models which focus on different approximations and parameterizations for the water activity a_w and the surface tension σ_{sol} of the solution droplet. Differences between the models are analyzed in the study of Rose et al. (2008). The previously defined

Raoult term is an approximation for this water activity and only works if the solution droplet is dilute and ideal (meaning all interactions between solution molecules are equal in strength). Furtheremore for particles consisting of a multitude of species of unknown density and mass the effect of the chemical composition on the condensation activity can't be described by Raoult as simple as before.

5.2.8 Hygroscopicity parameter κ

For particles with a multitude of soluble chemical constituents whose dissociation behaviour is unknown it is useful to characterize a particle's water activity a_w through a single parameter κ (Petters and Kreidenweis 2007). The Rault term was used as an approximation describing the water uptake ability of soluble salts like $(NH_4)SO_2$ whose chemical composition and dissociation behaviour in water is well known. In comparison the κ parameter can be used to describe the Koehler curve of a particle with unknown chemical composition. Using κ the Koehler equation (15) can be rewritten (Mikhailov et al. 2017).

$$S = \left(\frac{D_w^3 - D_s^3}{D_w^3 - D_s^3 \cdot (1 - \kappa)} \right) \cdot exp \left(\frac{A}{D_w} \right) \tag{18}$$

The hygroscopicity parameter κ can then be calculated by differentiating the saturation ratio S with respect to the droplet diameter d_w and setting the derivative to zero. Therefore κ is related to the maximum of the Koehler curve S_{crit} as that point determines a particle's condensational growth within a certain ambient saturation ratio. However for κ values above 0.1 an approximation can be derived which expresses κ as a function of the critical supersaturation s_{act} and the critical dry diameter d_{act} (Petters and Kreidenweis 2007).

$$\kappa = \left(\frac{4 \cdot A^3}{27 \cdot D_{s,crit} \cdot (ln(SS_{eff}))^2} \right) \tag{19}$$

From the work of Mikhailov et al. (2017) which experimentally determined the κ values of various pollen extracts the difference between the κ values determined by the full Koehler equation (which would require numerical algorithms for the solution) and the κ values found by the approximation in the equation above is less than 7%. In general κ values between 0.5 and 1.4 indicate inorganic species with strong water affinity while κ values between 0.01 and 0.5 stands for species containing a multidue of organic compounds (Petters and Kreidenweis (2007))

In general κ values between 0.5 and 1.4 indicate inorganic species with strong water affinity while κ values between 0.01 and 0.5 stands for species containing a multidue of organic compounds (Petters and Kreidenweis (2007)).
The κ range for organic species can be further specified and divided. Organic particles produced due to the burning of biomass exhibit κ values between 0.01 and 0.55. Such freshly produced organic species can increase their hygroscopicity due to the process of chemical aging, which increases their κ values into the range 0.1 - 0.3 (Andreae and Rosenfeld (2008)).

From the study of Pringle et al. (2010) the global mean for κ of aerosols above continental regions is calculated as (0.27 ± 0.21) while the mean value for κ of particles above oceanic regions is (0.72 ± 0.24). The values are calculated for particles of both the Aitken and accumulation modes which dominate the number concentrations in the atmosphere.

6 Experimental

After going through the most important aspects of the theroy for this work I will begin the experimental section by introducing the most important components that were used for the measurement.

6.1 CCNC

6.1.1 Operation principle

The single column continuous-flow streamwise thermal-gradiadient cloud condensation nuclei counter (CCNC) from Droplet Measurement Technologies is the key instrument for this study. The CCNC measures the number of particles that activate and grow into cloud droplets at given supersaturations. It's design and operation principles were thoroughly analyzed (Lance et al. (2006), Roberts and Nenes (2005)) and assessed through calibration experiments using ammonium sulphate and sodium chloride aerosol particles (Rose et al. (2008)). The traditional way of operating the CCNC is by changing the temperature gradient to step through the supersaturations but it is also possible to use it in a scanning flow mode, stepping through the supersaturations by changing the flow through the main column (Raatikainen et al. (2012), Moore and Nenes (2009)).

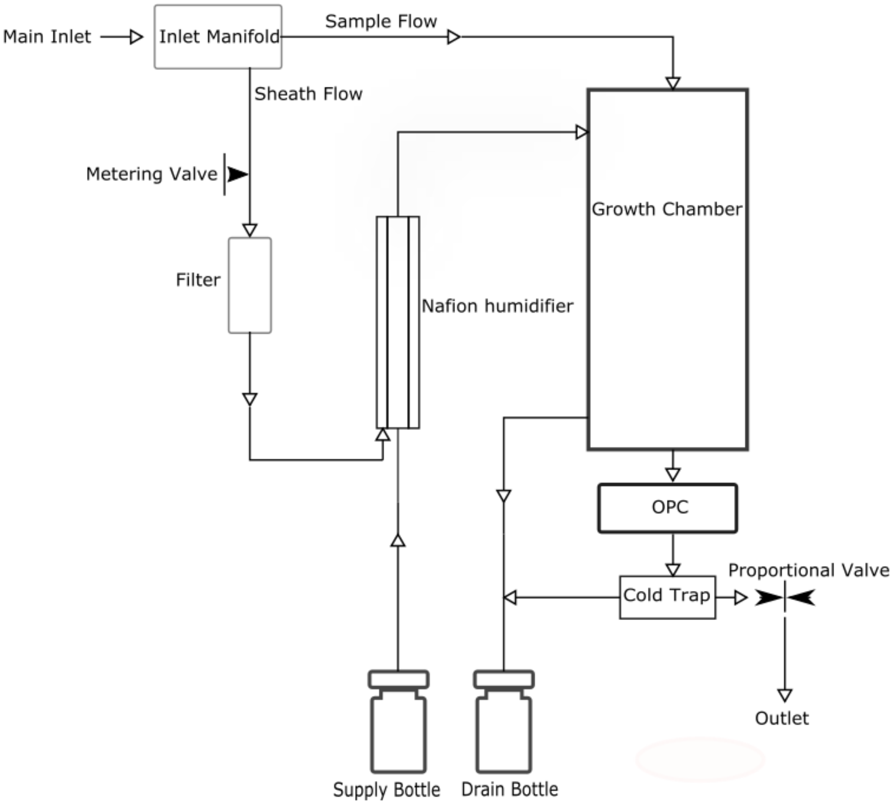

Figure 9: schematic of the CCNC's inner design

Figure 9 showcases a flow chart for the pathway of the aerosol flow through the CCNC. The flow is introduced through a main inlet which then reaches the inlet manifold. Here the flow is split into a seperate sample and sheath flow. The sheath stream goes through a filter to purify it from particles before being saturated with water vapor by a Nafion Perma-Pure humidifier. The Nafion humidifier is made of an outer and inner tube with the inner tubing wall highly permeable for water. Water from the supply bottle goes through the inner tube while the sheath stream is passes through the space between outer and inner tubing wall. Due to the humidity gradient between the water and the sheath stream water molecules pass the permeable inner tubing wall and saturate the sheath flow. The Nafion Perma-Pure unit is operated with a temperature close to the temperature at the entrance portion of the CCNC growth chamber.

The sample flow passes through a stainless steel capillary before rejoining with the sheath flow at the entrance portion and entering the growth chamber where particles can activate and grow into cloud droplets. Once the flow exits the column an Optical Particle Counter is used to analyze and count the number of droplets present. Using a diode laser (wavelength = 660nm) as the lightsource, droplets are counted and sized through the number and intensity of the light pulses they scatter when passing the laser. The sizing range goes from 0.75 to 10μm and there are 20 size bins. The number of droplets up to a maximum size of 0.75μm are collected in the first bin, the second bin counts the number of particles in the size range 0.75 to 1μm. The third bin goes from 1 to 1.5μm and from there the size difference between each bin remains 0.5μm. The first bin counts droplets that don't reach a size greater than 0.75μm and all passing particles that fail to activate.

The absolute values for both sheath and sample flows inside the CCNC are controlled indirectly with a metering valve at the sheath air line and a proportional valve set after the cold trap. The proportional valve controls the value of the total flow which for this work is kept at 0.5 L/min. The metering valve determines the sheath-to-sample flow ratio which is set at 10:1, 10 parts of sheath air for 1 part of sample air.

After calculating the droplet number per bin the flow enters the cold trap where the saturation point is lowered enough that in order for any remaining particles to condense and captured here before going to the proportional valve. These droplets are then collected in the drain bottle.

6.1.2 Growth chamber

The growth chamber is a cylindrical vertical column and constitutes the main component of the CCNC. Sheath and sample flow join each other in the entrance portion of the column and travel downstream along the vertical axis in a laminar profile. The sample flow travels along the centerline, surrounded by the purified sheath flow.

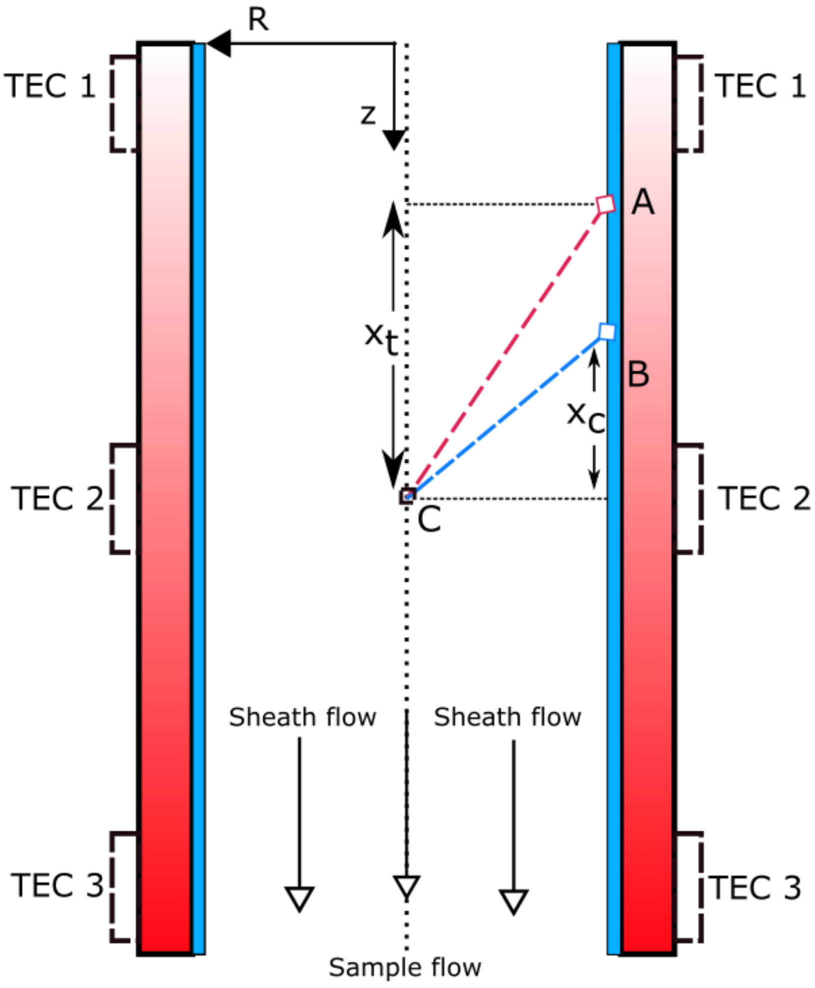

Figure 10: Establishing a supersaturation in the growth chamber

Each side of the column has 3 thermal electric coolers (TEC) installed. They each mantain a certain temperature range, with the TECs at the bottom of the column exhibiting the highest and the ones on the top the smallest temperature zones. They result in a temperature gradient inside the chamber, a gradual ascending slope from top to bottom. To ensure that this temperature gradient is mantained as linear as possible, the walls of the column must be thick enough in order for the heat transfer in the vertical streamwise direction to be much bigger than the convective heat losses to the sample flow. Furthermore heat-conductive silicon paste is applied between the TECs to allow proper heat transfer.

The inner surface of the column walls are mantained wet. Purified water from the supply bottle is brought into the chamber to keep the wetted walls saturated with water vapor. The temperature range of the TEC at the column top is kept higher than the ambient temperature. This prevents accidental droplet activation at the entrance portion of the chamber. The linear temperature gradient results in a near constant centerline supersaturation.

Figure 10 showcases how the supersaturation is generated at any point along the centerline where the sample stream is located. For a given point C of the centerline with the coordinates (0, z) the red and blue line indicate the heat from point A and the water vapor from point B diffusing from the inner wall surface. x_t and x_c are the distances in z direction that both heat and water vapor need to travel to reach C. Heat transer is primarily governed by N_2 and O_2 molecules which both exhibit molecular weights of 28u and 32u (u being the unit for atomic mass). H_2O has a molecular weight of 18u and thus it is much lighter and diffuses faster. At point B the saturation point of water vapor is higher than at point A due to the increased temperature. It follows that C has the temperature from point A and the amount of water vapor from the saturation point of B which correlates to a temperature higher than at A. This results in C being in a supersaturated state.

6.1.3 Calculating the centerline supersaturation

It can be shown from the work of Bergman et al. (2011) that the timescale needed for water vapor and heat to reach the centerline is given by

$$\tau_C = \frac{R^2}{D_v} \qquad and \qquad \tau_T = \frac{R^2}{\alpha} \tag{20}$$

Here R is the inner radius of the growth chamber. α is the diffusivity of heat and D_v is the diffusion coefficient for water vapor. The average velocity for a flow through a cylindric volume is given as $V_{mid} = \frac{Q}{\pi \cdot R^2}$ with Q being the flow rate. Thus the axial distances x_T and x_C for both heat and water vapor respectively can be given as

$$x_T = V_{mid} \cdot \tau_T = \frac{Q}{\pi \cdot \alpha} \qquad and \qquad x_C = V_{mid} \cdot \tau_C = \frac{Q}{\pi \cdot D_v} \tag{21}$$

Any point (0, z) along the centerline will have the inner surface temperature from (R, z - x_T) and the water vapor concentration from (R, z - x_C). The saturation ratio S at the is then defined as

$$S_{center} = \frac{p(0,z)}{p_s(T(0,z))} = \frac{p_s(T(R, z - x_c))}{p_s(T(R, z - x_T))} \tag{22}$$

From the Clausius Clapeyron equation it has been shown that the saturation pressure p_s is a function of the temperature T. The vapor pressure p at the point (0, z) of the centerline is equal to the saturation vapor pressure at the point (R, z - x_c) of the inner walls. The transferred heat from point (R, z - x_T) results in the point (0, z) having that same temperature which correlates to a saturation vapor pressure equal to that at (R, z - x_T). The previously defined general form of the Clausius Clapeyron equation can be transformed into a simple version for solely liquid-vapor systems which allows to calculate saturation vapor pressures at given temperatures when the vapor pressure at a reference temperature is known.

$$\frac{p_s(T_2)}{p_s(T_1)} = exp(\frac{\Delta H_v \cdot (T_2 - T_1)}{R_g \cdot T_1 \cdot T_2}) \approx 1 + \frac{\Delta H_v \cdot (T_2 - T_1)}{R_g \cdot T_1^2} \tag{23}$$

The expression is then approximated with a first-order Taylor expansion and the product $T_1 \cdot T_2$ can be approximated with T_1^2 for small temperature differences. Subtituing the expression for S_{center} into this approximation yields

$$\frac{p_s(T(R, z - x_c))}{p_s(T(R, z - x_T))} = 1 + \frac{\Delta H_v \cdot \Delta T}{R_g \cdot (T(R, z - x_T))^2} \tag{24}$$

The temperature gradient G along the walls is constant and therefore for any distance $x_T - xc$ the temperature difference ΔT is given as $\Delta T = G \cdot (x_T - xc)$. Using the previously defined diffusional timescales for heat and water vapor the distance $x_T - xc$ can be expressed as a function of the column Radius and the diffusion coefficients.

$$x_T - xc = (\tau_T - \tau_C) \cdot V_{mid} = V_{mid} \cdot R^2 \cdot (\frac{1}{\alpha} - \frac{1}{D_v}) \tag{25}$$

$$T(R, z - x_T) = T(R, z) - G \cdot x_T = T(R, z) - G \cdot \frac{R^2 \cdot V_{mid}}{\alpha} \tag{26}$$

Using both expressions above and entering them into equation (5) yiels the centerline saturation ratio S_{center} as a function of the operational parameters Q and R.

$$S_{center} = 1 + \frac{\Delta H_v}{R_g \cdot \pi} \cdot \frac{G \cdot Q}{T(R, z) - \frac{G \cdot Q}{\alpha \cdot \pi}} \cdot (\frac{1}{\alpha} - \frac{1}{D_v}) \tag{27}$$

$$s_{center} = (S_{center} - 1) \cdot 100\% \tag{28}$$

If a particle's size and chemical composition results in a critical supersaturation s larger than the established centerline supersaturation s_{center} then the particle will be able to activate and grow into a cloud droplet. Thus it will gain the nessecary size to be in the detectable range of the OPC. Depending on how quickly a sample particle manages to activate it will have more time to grow. Particles with a Koehler curve that showcase a small distance till reaching the critical supersaturation will mostly activate in the upper portion of the growth chamber, allowing for more time to grow before reaching the OPC. Highly hygroscopic salt particles manage to appear in droplet form even at very small sizes in subsaturated conditions, spending most of their travel time in the column to grow.

6.1.4 Flow calibration

It is important to make sure that the flow with which the CCNC draws in particle is the same as the one shown on the CCNC software because the centerline supersaturation is dependent of the flow through the growth chamber. In this work experiments have been conducted with the CCNC software set at a flow of 0.5 L/min. The following procedure assures that the true flow inside the chamber is close to equal to the one shown on the display.

First a no-particle filter is installed onto the CCNC inlet and soon after the display needs to show a particle count of less than 5 per second. After this is done the supersaturation on the CCNC is set at 5 nominal values, at each the CCNC is measuring for a few minutes. It must be ensured that the CCNC counts more particles with rising supersaturation. Both of these procedures ensure that the CCNC is measuring correctly.

Afterwards a gillibrator is connected to the inlet, measuring the flow in 1 minute intervalls for 5 minutes. A mean value is calculated and compared with the flow value shown on the Display. According to the CCNC operator manual the difference between this average and the flow value shown on the display should at worst have a maximum difference of ±10%.

Both sheath and sample flow of the CCNC are calibrated seperately. For the sample flow the sheath flow metering valve at the back of the CCNC is closed completely, ensuring that the CCNC only draws with the remaining sample flow. Ont he DMT service tab of the software the "FlowCal" sub table is clicked on and the values of "Sample Flow y-int" and "Sample Flow slope" are changed to 0 and 1 respectively. With the “"Valve Set M(V)" option the valve voltage is adjusted till the flow measured on the gillibrator is approximately 75 cm^3/min. The "Sample Flow" field on the display now shows the voltage value from the sample flow pressure transducer (which measures the sample flow inside the CCNC). The volve voltage is adjusted again till the gillibrator measures external flows of 60, 45 , 30 and 20 cm^3/min. For each of those the voltage value on the "Sample flow" field is noted. A linear regression is run between the notes voltage values and the values of the external flows. The slope of and intercept of this regression are written into the FlowCal tab as the new calibration paremeters.

In a very similar way the sheath flow is calibrated.

6.2 DMA

6.2.1 Theory and operation principle

The Differential Mobility Analyzer, in short DMA, is used to classify particles of a polydisperse sample according to the measurement technique of Electrical Mobility Spectrometry. The DMA used here is the Vienna Type (Reischl (1991), Winklmayr et al. (1991)) which exhibits a cylindrical capacitor design. Figure 9 shows the general structure of a cylindrical Vienna Type DMA.

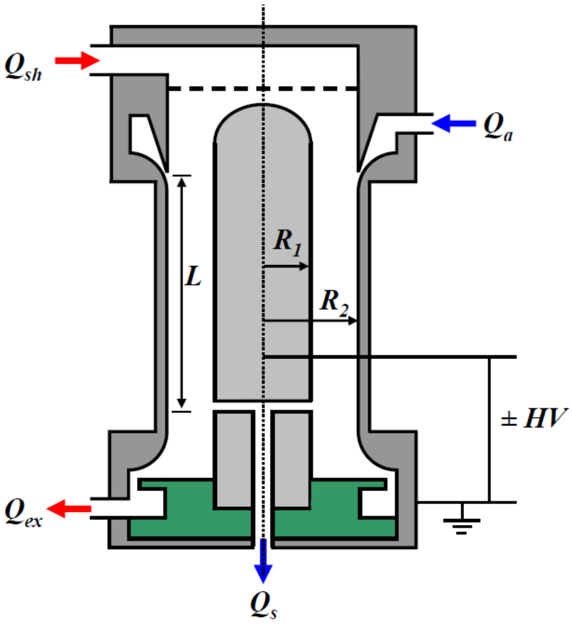

Figure 11: Structure of a cylindrical Vienna Type DMA, adapted from Steiner (2011)

The sample flow Q_a is introduced through an inlet near the top of the outer electrode. The cavity between inner and outer electrode is filled with purified particle-free sheath air of laminar flow Q_{sh}. Setting up a voltage builts a radial electric field between inner and outer electrode. Charged particles entering the DMA chamber experience both an electrostatic force $\vec{F_E}$ in radial direction and a drag force $\vec{F_R}$ in axial direction expressed through Stokes law which assumes spherical shape of the particles and a laminar flow profile of the carrier flow.

$$\vec{F_E} = n \cdot e_0 \cdot \vec{E} \qquad \vec{F_R} = \frac{3 \cdot \pi \cdot \eta \cdot D_p \cdot \vec{v}}{C(D_p)} \tag{29}$$

$\vec{E}$ is the vector of the radial electric field, describing both the field's direction and strength. $n \cdot e_0$ indicates the number of the elementary charges on the particle. For the drag force $\vec{F_R}$ η is the dynamic viscosity of the carrier gas, D_p is the aerodynamic equivalent diameter which is equal to the diameter of a sphere with a density of $1g/cm^3$ and $\vec{v}$ is the drift velocity of the particle . $C(D_p)$ is the Cunningham slip correction factor which reduces the drag force on particles whose size approaches the mean free path of the carrier gas molecules, meaning very small values. With a higher particle diameter $C(D_p)$ converges against 1 which means no reduction of the drag force. The combination of both forces results in a drift movement where only particles with certain electrical mobilities Z manage to leave the DMA in a classified flow Q_s through a narrow slit in the inner electrode. All other non-classified particles leave the DMA in an exhaust flow Q_{ex}. The flow Q_{ex} is then filtered and reintroduced as purified sheath flow Q_{sh}. The electrical mobility Z of a particle under the influence of forces $\vec{F_E}$ and $\vec{F_R}$ is defined as

$$Z = \frac{n \cdot e_0 \cdot \ C(D_p)}{3 \cdot \pi \cdot \eta \cdot D_p} \tag{30}$$

D_p is here the mobility equivalent diameter, meaning the diameter of a spherical particle with the same electric mobility Z as a particle of non-spherical shape.

Furthermore at a set of constant geometrical and operational parameters the electrical mean mobility Z^* can be derived as a function of only the applied voltage V.

$$Z^* = \frac{1}{V} \cdot \frac{ln(R_2/R_1)}{2 \cdot \pi \cdot L} \cdot \frac{Q_{sh} + Q_{ex}}{2} \tag{31}$$

Here L is the effective length of the DMA channel, R_1 is the outer radius of the inner electrode, R_2 is the inner radius of the outer electrode and both Q_{sh} and Q_{ex} are as already mentioned before the sheath and exhaust flow. Z^* is defined as the eletrical mobility of particles entering the DMA in the middle of the sample flow Q_a and leaving in the middle of the classified flow Q_s.

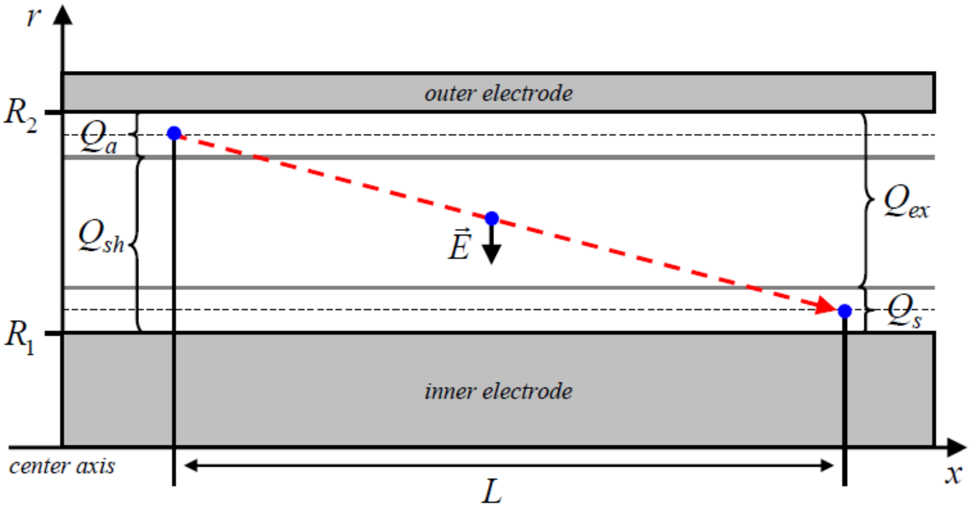

Figure 12: Figure from the dissertation of Mag. Gerhard Steiner showing the highest and lowest mobility trajectories through the DMA. April 2011. "High Resolution Mobility Spectrometry Of Molecular Ions And Their Effect On The Charging Probabilities Of Airborne Particles Under Bipolar Diffusion Charging Conditions". Faculty of Physics.

For symmetric operation conditions ($Q_s = Q_a$ and $Q_s = Q_s$) equation 31 becomes

$$Z^* = \frac{1}{V} \cdot \frac{ln(R_2/R_1}{2 \cdot \pi \cdot L} \cdot Q_{sh} \tag{32}$$

Combining both expressions for the electrical mobility Z and eletrical mobility Z* yields a relation between aerodynamic equivalent particle diameter Dp, number of charges i and applied voltage V (for constant geometry parameters).

$$\frac{n \cdot e_0 \cdot \ C(D_p)}{3 \cdot \pi \cdot \eta \cdot D_p} = \frac{1}{V} \cdot \frac{ln(R_2/R_1}{2 \cdot \pi \cdot L} \cdot Q_{sh} \tag{33}$$

A specific eletrical mobility equals singly charged particles with a certain diameter D but it also includes doubly charged particles with diameter 2*D, particles with three charges and diameter 3*D, etc.. A specific voltage there doesn't equal classified particles of a single size.

For this experiment it is nessecary to convert voltage values into their respective singly charged mobility equivalent particle diameters. By rearranging equation (32) the voltage V can be directly calculated for a given mobility equivalent diameter D_p with a given number of charges n. However the equation is not directly solvable for D_p for any given V since D_p is included directly and indirectly through the Cunningham Correction Factor $C(D_p)$. One can use iterative procedures to determine D_p for any given value of V.

In this thesis the D_p values for any given V are calculated through an inversion method in python. First an n-dimensional vector x with n diameter values in the range of 1nm-1000nm is generated. Using the relation in (32) the voltage V is calculated for each vector element, resulting in a new vector y which includes all calculated voltages as it's elements. The interp function from the numpy module is used to generate a linear interpolation polynomial. It is generated by using the calculated voltage vector f(x) as the x data and the generated diameter value x as the y data. Afterwards a new vector xx with 10000 voltage values as elements is created the linear polynomial is evaluated at these 10000 voltages. This results in a vector with diameter results for each integer voltage in the range of 1V - 10000V. For this measurement only integer voltage values are typed into the DMA control software.

6.2.2 Transferfunction

Applying a voltage on the inner electrode doesn't mean that only particles with one specific value for the eletrical mean mobility Z^* get extracted. A DMA's performance is limited due to it's finite resolution and therefore The classified flow Q_s contains particles in a certain mobility range Z^* - $\Delta Z^* <$ Z $< Z^* + \Delta Z^*$. The propability of a particle with eletrical mobility Z to be within this mobility range is given by the Transfer Function TR(Z). By definition the transfer function TR(Z) is the propability that particles with certain electrical mobility Z are included in the classified outler flow Q_s when voltage and flow values are set for a certain eletrical mean mobility Z^*. The Transfer Function TR(Z) takes on values between 0 and 1. A value of 1 is reached when the electrical mobility Z of incoming particles equals the eletrical mean mobility Z^*.

The full width ΔZ^* at TR(Z) = 0.5 divided by the mean eletrical mobility Z^* specifies the resolution of the DMA. This resolution is in practice given be the ratio of the incoming sample flow Q_a and the sheath flow Q_s (Willeke and Baron 2001).

6.2.3 PSL measurements

To determine the DMA's specific resolution (without accounting for diffusion losses) and verify the validity of the above described inversion method to derive the singly charged diameter value from a given voltage, measurements with monodisperse polystyrene latex (PSL)l sample solutions are conducted. Two sizes (288nm and 390nm) of PSL solutions are used to create dilute aqueous sample solutions (2-3 droplets mixed in 40ml water). Both are atomized, subsequently dried and classified in the DMA at various voltage values. The CPC measures the number concentration per cubic centemeter of the classified fractions. Since according to equation (8) one voltage values corresponds to multiple diameters the resulting data is not a size distribution but rather a mobility/voltage-distribution. Figure 13 shows the voltage distribution for both the PSL-288nm sample and the PSL-390nm sample.

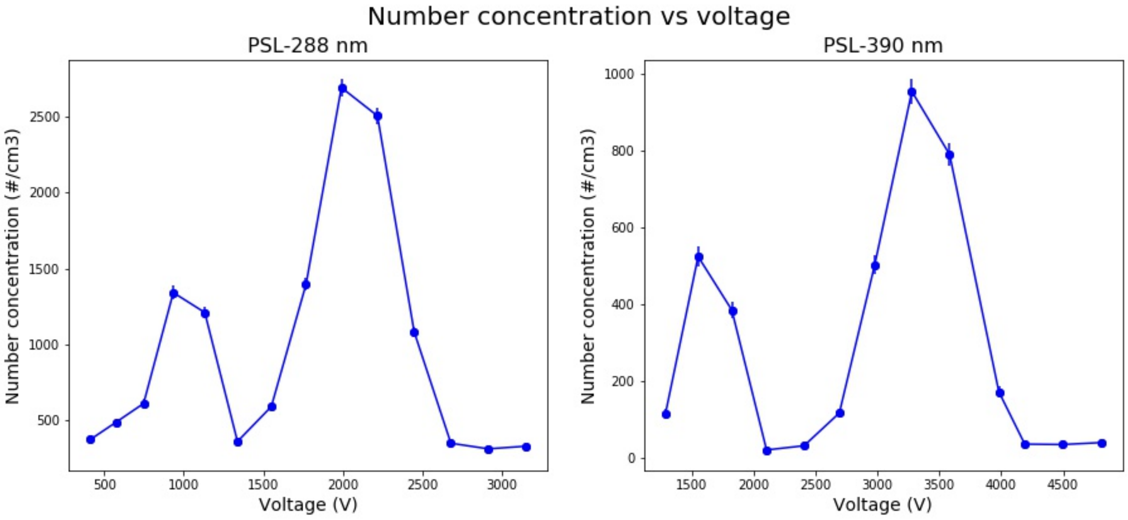

Figure 13: Number concentration vs voltage

Both sample solutions consist of only monodisperse particles. Looking at eqation 33 a constant particle diameter leaves only the number of charges n and the voltage as the free parameters. If the number of charges n is multiplied by 2, the voltage is divided by 2 and the same applies for any higher numbers. Therefore for a monodisperse aerosol source the DMA classifies a singly charged particle fraction with it's maximum at a certain voltage value while also classifying a doubly charged particle fraction with it's maximum at half of that voltage value. Depending on the size distribution of the sample aerosol sometimes even a fraction of particles with third charges can be idenified at a third of the same voltage value. Identifying the right peak for both graphs at figure 13 as the peak of singly charged particles, these data points are cut out and plotted in a new graph before fitted with a Gauss curve. The maxima of both fits from figure 14 correspond to certain voltage values. Those value are then converted to their respected diameter and compared with the PSl size. For the PSL-288nm measurement the maximum of the singly charged peak corresponds to a voltage of 2068.5 V. This voltage is converted to it's singly charged diameter value, which is 276.5nm. Comparing it with 288nm shows that there is a certain difference in what is expected. The PSL sample solution could consist of not only specifically 288 nm particles but a fraction around that value. Sampling losses and the finite resolution of the DMA have both an influence on the resulting data point and thus an influence on the peak maximum of the fit. For the PSL-390nm measurement the singly charged peak maximum corresponds to the voltage 3360.1 V. This equals a diameter value of 393.5 nm which is much closer to the expected value of 390nm.

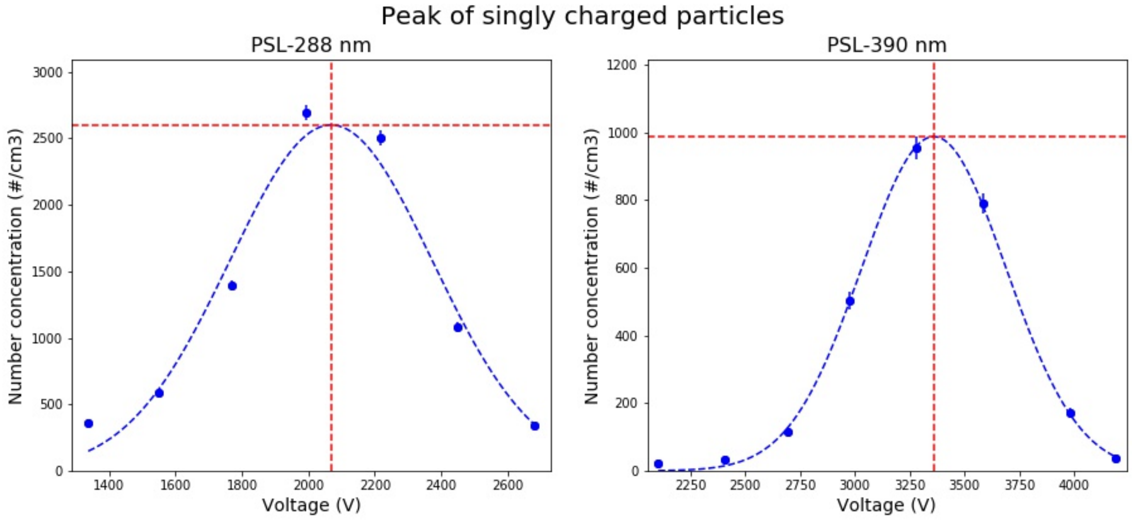

Figure 14: Gauss fit over the data points of the singly charged peak from both PSL measurements

With higher particle sizes diffusion losses loose on importance and that could be a reason for the more accurate result for the measurement with the PSL-390 sample. The DMA's measurement capability is verified if the maxima of these peaks are equal to to size of the PSL particles. Diffusion losses for smaller particles and finite resolution will result in deviations.

6.3 Experimental Setup

6.3.1 Setup and schematic of the experiment

Figure 15 describes the schematic construction for the experiment of this work.

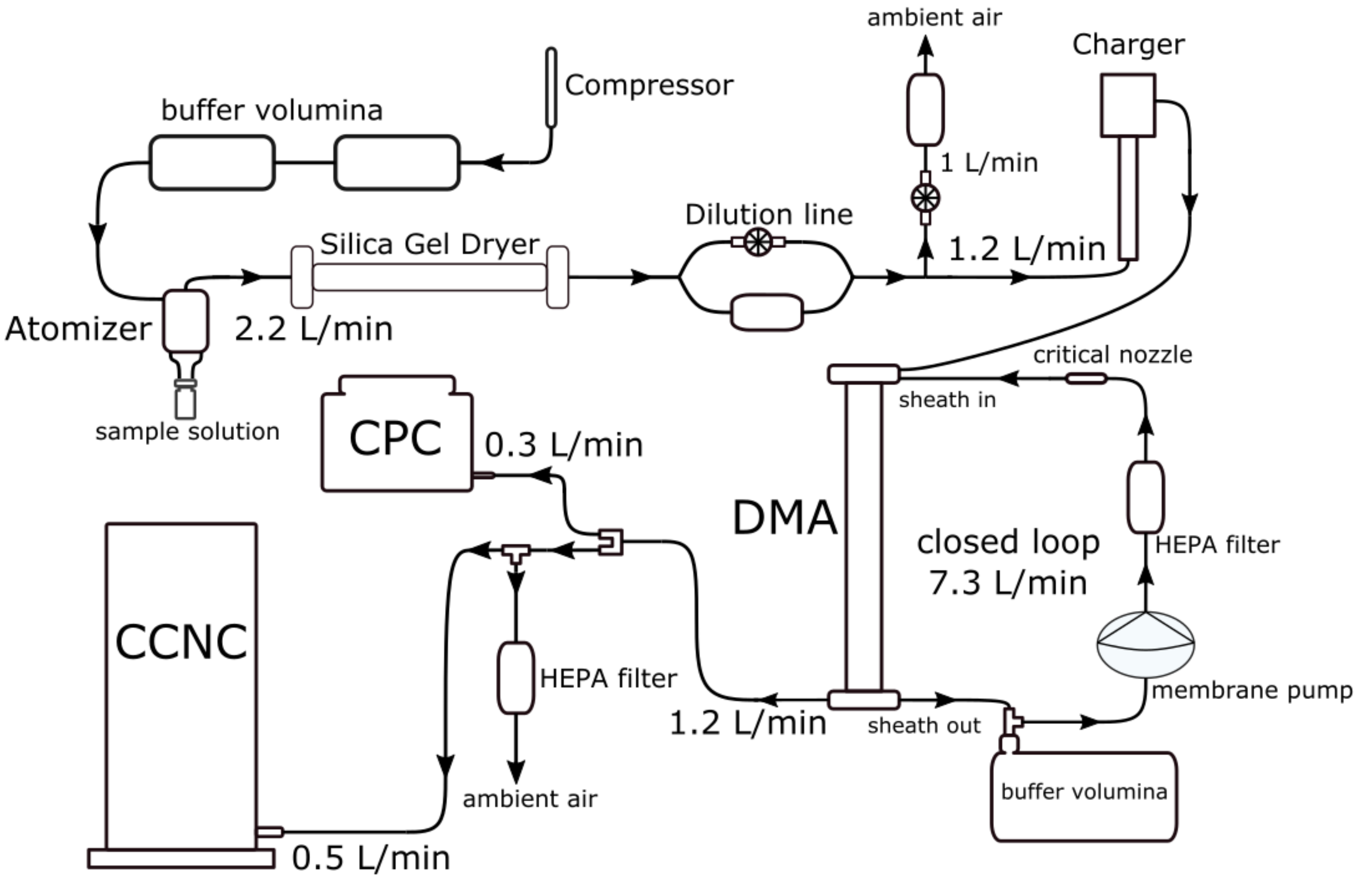

Figure 15: setup for the experiment

The experiment consists of two parts and the setup shown in figure 15 is used for both (with minor differences detailed later on).

A solution of sample particles with ultrapure water with a conductivity value below 0.07 μS/cm is prepared in a small bottle. The bottle is then connected to the bottom of the aerosol atomizer. Pressurized air is provided from a compressor which allows the atomizer to generate droplets consisting of solid particles. Pressure fluctuations in the compressor lead to variations in the pressurized air flow. To help stabilize the volumetric flow 2 mixing vessels are installed in the line between compressor and atomizer. A pressure value of 1 bar is set on the control panel for the compressor. This corresponds roughly to a volumetric of flow around 2L/min. A stable flow through the sample line is important for both the DMA and the CCNC especially. A changing sample flow leads to changes in the DMA's resolution power and for the CCNC the centerline supersaturation depends on the flow through the growth chamber among other variables (Roberts and Nenes (2005)).

The generated droplets travel through 2 Cilica Gel dryers to keep the wetness level to a minimum in order for the solid sample particles to remain. The following dilution line allows adjustment of the particle number concentration. This part is used for every calibration measurement with salt particles due to their size distributions showcasing maxima in the aitken mode size range. Since salt particles are highly hygroscopic they already activate at very small sizes and therefore calibration measurements are done mainly in this size range. Particle concentration of above

2000 cm^3 can lead to increased water vapor depletion effects on the centerline supersaturation, leading to particles competing for water vapor and not being able to reach droplet sizes they would have at smaller number concentrations (Lathem and Nenes (2011)). An installed valve on the right side allows to control the amount of the flow that splits itself from the incoming sample stream. That splitted flow travels through an HEPA filter to rid itself of particles for cleaning. This cleaned sheath air stream is then unified with the sample stream. The particle number concentration of the mixture of both flows has been reduced. Opening the valve fully indicates splitting a the highest amount of flow which indicates the highest possible dilution level for the sample stream. Due to no display available on the valve it's not possible to say the exact value of the splitted flow.

The line seperates into 2 directions, one of them being connected to another HEPA filter with it's ending leading to the ambient atmosphere of the laboratory. As seen in the section of the DMA, the highest possible resolution for size stepping at constant geometry parameters is achieved by a small sample flow Q_a compared to the sheath flow Q_s inside the DMA. Both CCNC and CPC together draw a flow of $0.8cm^3$/min. Therefore the sample flow through the DMA can't be lower than that but it's desirable to keep it as close as possible to it. The additional line with the HEPA filter allows a reduction of the overflow by closely 1 L/min. This means that the incoming sample stream which previously hung around a value of 2L/min enters the charger and DMA subsequently is now around a flow value of 1L/min which is much closer to the desired 0.8L/min. Further reduction of pressure on the compressor control panel leads to a further flow reduction. However due to the high sensitivity of the compressor control panel, a very slight move of the controlling valve can bring higher pressure reductions with time, leading to the sample flow inside the DNA to be underneath 0.8L/min. In that case sheath flow will be drawn into the CPC and CCNC to accustom for the flow loss.

The sample stream enters the charger to ensure a stable charge equilibrium state of the aerosol before going through the DMA where a narrow fraction of particles is allowed to leave. It's maximum corresponds to the particle size of the selected voltage. The line is split once again between the CPC and the CCNC. The line towards the CCNC has another line connected with a HEPA filter which corrects additional overflows. Both CPC and the CCNC measure the number of particles per cm^3.

The sheath flow for the DMA is set around a value of 7.3 L/min. A critical nozzle controls stabilizes the flow around this value. Another HEPA filter is used to purify the air stream before reaching the DMA.

6.3.2 General procedure of the experiment

The first part of the experiment involves the calibration of the CCNC with a sample solution of $(NH_4)SO_2$ in ultrapure water with a condictivity value below 0.07 μS/cm. Mixing 8 mg of solid $(NH_4)SO_2$ with 80 ml ultrapure water will result in an aqueous solution with a salt concentration of 0.1g/L, keepig the solution as dilute as possible. A salt like $(NH_4)SO_2$ was chosen as the calibration standard because it's CCN activation ability is well known and the particles themselves are almost spherically shaped.

In the second part of the experimental procedure, aqueous solutions of the soluble cytoplasmic sample matericals from the respective pollen samples are prepared (extraction of soluble cytoplasm material described in the work of Gratzl (2020)). In comparison to the calibration standard which features a defined concentration, the solution concentrations of the cytoplasm samples all vary depending on the pollen species. The reason for that are the different size distributions of the various cytoplasm species. Small number concentrations at low particle diameters will be more strongly influenced by diffusion losses and result in higher errors in the concentration measurements by the CPC and CCNC. That in return affects the error in the calculated CCNC/CPC ratios. Therefore those sample solutions require higher solute concentrations in order to make up for the low size distributions. In general the incoming number concentration of the sample flow should stay below 3000 $\#/cm^3$ in order to avoid coincidence errors on the OPC inside the CCNC. But lower concentration values like 200 $\#/cm^3$ should also be avoided since diffusion and sampling losses will have a much bigger impact on the deviation of particle concentration.

6.4 Calibration

This section describes the step-by-step procedure to gain a good graphical representation of the CCN activity of $(NH_4)SO_2$ salt particles at multiple centerline supersaturations. From each activation spectra a critical diameter or critical supersaturation can be retrieved which corresponds to a certain temperature gradient in the CCNC. Using Koehler theory (Lohmann et al. (2016), Seinfeld and Spyros (2006)) each critical raw diameter corresponds to a critical supersaturation. Plotting these calculated supersaturations against the temperature gradient leads to a calibration line, showcasing a near linear dependence (Rose et al. (2008), Lance et al. (2006)).

By the end of a general experiment cycle (as explained above in the general procedure section) we are left with measurement data for the number concentration of the CCNC and CPC. Both measure the number concentration of particles per cm^3.

There are 2 ways to measure the condensation activity. In one way the nominal supersaturation in the CCNC is held at a constant value and the voltage on the DMA is varied around a certain range (DMPS mode). Then the voltages are converted into their respective singly charged particle diameter values, expressed in nanometers according to the way described in the DMA section. The calculated ratios CCNC/CPC are plotted as a fuction of these particle diameters. This measurement principle is called D-Scans. The other way is to have the DMA set a fixed voltage and vary the nominal supersaturation in the CCNC, resulting in a graph of the CCNC/CPC ratios plotted against the stepped nomnial supersaturations. This way of measuring the CCN activity is called S-Scans. Both ways are valid methods to describe the CCN activation of an aerosol sample. For the calibration it is nessecary to first use the D-scan method and verify the principle through the S-scan method.

6.4.1 D-scans

First the D-Scans approach to gain an activation curve will be described in detail. For this the raw measurement data for the $(NH_4)SO_2$ sample solution at a fixed nominal supersaturation of 0.1% is shown in the graph below (figure 16).

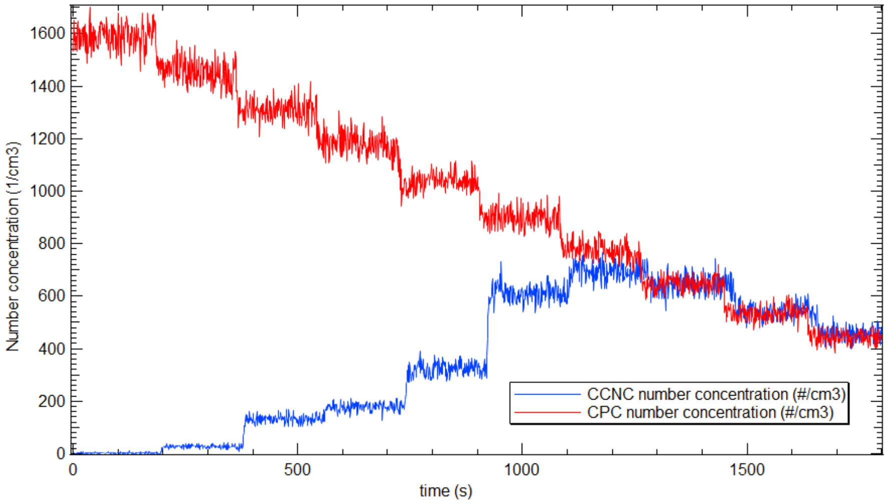

Figure 16: number concentration vs time

The nominal supersaturation ss = 0.1% corresponds to a temperature gradient of (3.1 ± 0.1) K. The temperature gradient is most commonly calculated as $\Delta T = T_3 - T_1$ but for this work the temperature gradient is calculated through $\Delta T = 2 \cdot (T_2 - T_1)$ as recommended in the standardized operations procedure (SOP) document provided by ACTRIS. The reason for using this particular for for the temperature gradient is the slightly higher temperature gradient in the first half of the CCNC growth chamber. The temperature zone T_2 controlled by the TEC in the center is kept slightly higher then it would be for an ideal linear temperature gradient. This is done with the aim of ensuring that droplet activation occurs mainly in the first half of the column, leaving the second half solely for droplet growth.

$(NH_4)SO_2$ has it's number concentration peak at around <40nm and therefore with rising diameter steps the CPC number concentration falls. The CCNC number concentration rises with higher diameter steps because a bigger particle has a smaller critical supersaturation which means enhanced chance for droplet activation. At a certain diameter value both number concentrations of CCNC and CPC remain largely at the same values. This is because the CPC measures all incoming particles and after a certain diameter value all particles grow into optically detectable droplets.

Both CPC and CCNC start at the same time (CPC may sometimes lag by a second) and at each voltage they both measure for 180 seconds which equals 180 data points for the number concentration. For this example 10 voltage values are selected on the DMA and therefore the total measurement time is 1800 seconds (30 minutes). For each diameter scan (measurement of number concentration at a certain voltage) the first 90 seconds are cut to allow the CCNC time to adjust to the new incoming size distribution (Rose et al 2008, SOP ACTRIS). The voltages are converted into their respective singly charged diameter values while the CCN active particle fraction CCNC/CPC is calculated from the remaining data points at each diameter scan. Afterwards for each diameter a CCNC/CPC mean value is determined. The graph below (figure 17) showcases the mean ratios as a function of the singly charged diameter values.

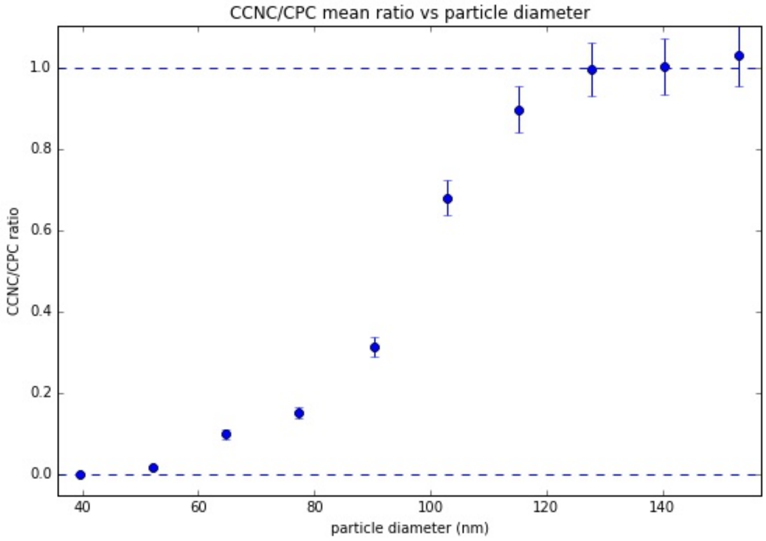

Figure 17: ratios vs particle diameter

The error bars are calculated from Gauss's rule of error propagation for divisions and multiplications. The deviations increase with higher diameter values. A reason for that could be that spontanous evaporation and condensation plays a bigger role on the way through the CCNC chamber when more particles have the chance to grow into droplets. At diameters below the critical point the activation probability remains low and thus the number of optically detectable droplets entering the OPC remains constantly low.

A ratio of 1 indicates that all incoming particles activate and have sufficient time in the CCNC chamber to grow into cloud droplets at the given nominal supersaturation. A ratio of zero indicates that either particles can't reach their critical diameter or they can reach it but have not enough time left in the chamber to continue growing to a size that can induce a signal within the OPC. Slight deviations from a total acivation ratio of 1 can occur. Diffusion losses in the sample line (especially at smaller diameter values) to the CCNC or high insolubility of the sample can cause a slight reduction for the total activation plateu, reaching only a ratio of 0.9 or slightly lower. On the other hand particles stuck in the chamber from previous measurement cycles activate at high diameters too, causing a slight shit above 1. Ideally additional diameter scans after reaching total activation should form a constant plateu at 1 due to the effects mentioned before but this is not always easy to achieve.

In order to account for the deviations from a perfect total activation ratio of 1 the mean ratio values are normalized. This is done by multiplying the mean ratios with a factor of a/0.5 where a is half of the plateu of total activation. As previously mentioned the plateu of total activation should form a constant line at 1. However in the case of this activation spectra there is a slight rise above 1 after reaching total activation. A mean of the last 3 measurement points is calculated and used as the total activation value.

6.4.2 Data fitting procedure

After the normalization of data points to the maximum activation plateu the data is fitted with a sigmoid function.

$$y(x) = base + \frac{max - base}{1 + exp((x_{half} - x) \cdot (1/rate))} \tag{34}$$

For this work the The fitting is done with the curve_fit function from the scipy_optimize module in python as well as with Igor Pro's built in sigmoid fitting feature. Igor Pro's fitting routine doesn't require input parameters and finds the best case fitting parameters automatically. The curve_fit function requires a more manual approach which will be described here shortly. In order to fit the data points as accurately as possible the curve_fit function needs good estimations for the parameters base, max, rate and x_{half}. The better these values are guessed the more accurate the fitting is conducted. The initial base value is taken as a mean of all data points at zero activation. Here only one ratio value touches the 0 line so only that one will be taken as the base.

The initial max parameter takes on the mean of the 3 last data points that are near the 1 line. The only other parameters left are x_{half} and the rate. The rate indicates the range on the x-axis that matches the biggest growth of the sigmoid function. The ratio means grow the most in the area between 80 and 120 nm and therefore a value of 40 is used as the input value for the rate. x_{half} represents the critical raw diameter $D_{critraw}$. For a D-scan activation spectra It is defined as the particle size where 50% of the incoming sample particles manage to reach the critical droplet diameter which enables their growth into optically sizable droplets. The initial input value is estimated as $x_{halftry} = \frac{diameter_{max} - diameter_{min}}{2}$. $diameter_{max}$ equals 153.1 nm which is the diameter value on the x-axis that corresponds to the last ratio point. $diameter_{min}$ is 39.7 nm which corresponds to the first ratio point. Using these values the curve_fit function tries to find the best possible sigmoid fit through the data (figure 18).

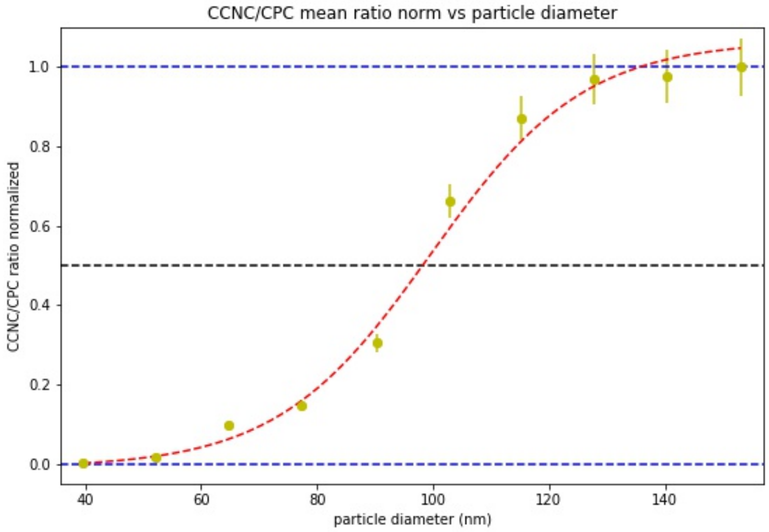

Figure 18: normalized ratios vs particle diameter

The curve_fit procedure delivers for x_{half} a value of (99.6 ± 10.4) nm. It's important to note that the error here is the error of the fitting procedure. To gain the error for the critical diameter multiple D-scan activation spectra at the same nominal supersaturation need to be done and the standard deviation of the mean of multiple $D_{crit,raw}$ values provides an estimation for the error.

To ensure that the sigmoid function can properly go through all data points the diameter values are chosen as equidistant to each other as possible. This is done by first search the voltage values where the number concentration of the sample solution reaches a maximum and a minimum. Both of these values are noted. Then both of these voltages are converted into their respective singly charged diameter. Dividing the difference between these diameter values with the chosen number of steps (in figure 18 this number is 10) gives the distance between each diameter point. All of these are converted back to their voltage values which are then used as input voltages for the DMA once the measurement starts.

6.4.3 Correction of doubly charged particles

The fitting error for x_{half} is rather large but this is presumably because the fit function doesn't go as accurately through the data points as wanted.

The reason for that are the fraction of doubly charged particles which are extracted from the DMA. Selecting a voltage on the DMA means that only particles within certain electrical mobility range are allowed to continue. Looking back at equation (31) in the DMA section a certain voltage equals a certain particle size with a single charge. But it also equals double this size with 2 charges and triple the size with 3 charges and so on. The x-axis shows the singly charged diameter values. As an example at a singly charged diameter value of 50nm we also have a fraction of doubly charged particles with 100nm diameter.

The latter activates earlier due to their larger size and the activation ratio CCNC/CPC is slightly increased. In order to gain the activation curve for only singly charged particles the baseline of the fit function is set to the plateu of doubly charged activation ratios (Gysel and Stratmann 2013). This is done in python by cutting off the first 2 data points and making new estimations on the fit parameters on the new reduced data range as described in the Data analysis procedure subsection.

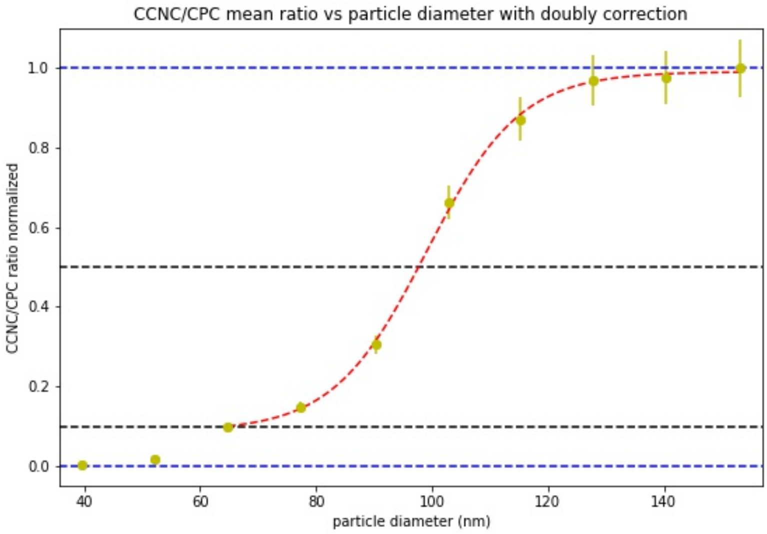

Figure 19: normalized ratios vs particle diameter with charge correction

Figure 19 shows the corrected fit which now only represents the activation of singly charged particles. The third data point has been used as the new baseline for the fit because a plateu of doubly charged particles can't be found (more data points would be needed to see for certain if a constant plateu of doubly charged particled can be found). The third data point slightly deviates from the desired sigmoid curve, indicating the slight increase of activation ratio due to doubly charged particles. For x_{half} we now get a value of (99.1 ± 0.3) nm. The correction yielded only a slight reduction for the x_{half} value but the fitting error was reduced significantly because now the fit function follows the data points much more accurately.

A narrow transfer function on the DMA can significantly help in identifying this plateu of doubly charged particles.

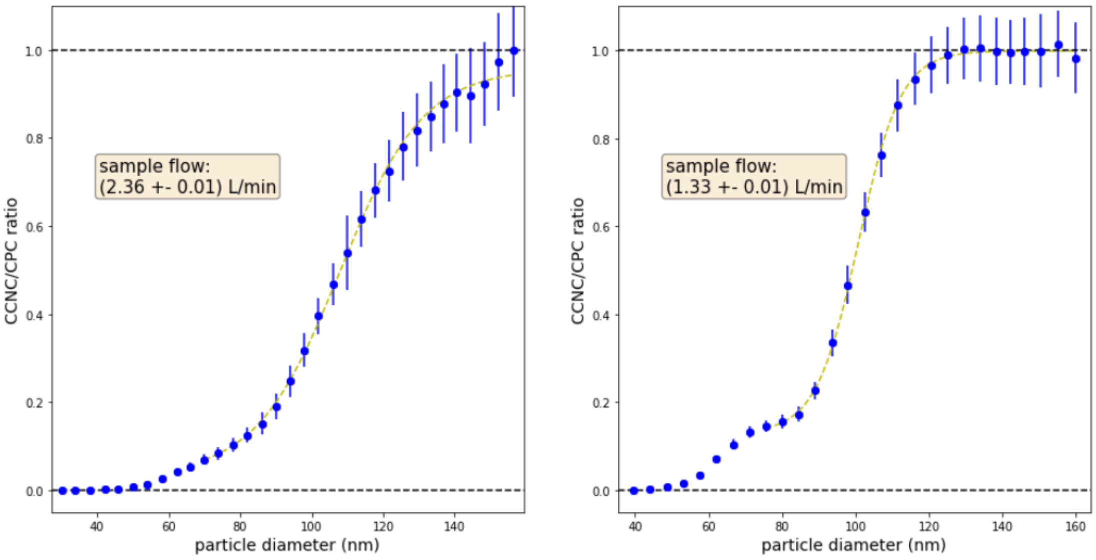

Figure 20: Influence of DMA resolution on finding the doubly charged plateu

Figure 20 illustrates the activation spectra of Ammoniumsulphat sample solutions at a nominal supersaturation of 0.1%.

Ideally the activation curve should be a step function, with all particles activating after reaching the critical diameter and the rest not reacting beneath the critical size. Due to the finite transfer function of the DMA a certain voltage allows a certain fraction of particles to be extracted. A very narrow transfer function translates to a narrow range of classified particles. Doubly charged particles can be easier seperated for monodisperse measurements with a higher DMA resolution.

The instrument specific resolution power of the DMA is given by the ratio $\frac{Q_a}{Q_{sh}}$ where the Q_a indicates the sample flow that carries the particles into the DMA and Q_{sh}, the sheath flow that surrounds the sample flow inside the DMA. A higher value of this ratio broadens the transfer function and weakens the resolution power of the DMA. The activation spectra to the left was measured at a sample flow of 2.36 ± 0.1 L/min while the graph to the right at a sample flow value of 1.33 ± 0.1 L/min. The resolution power is therefore higher for the activation ratio on the right, indicated by the much more visible plateu of doubly charged particles..

6.4.4 Calculating the effective supersaturation and plotting the calibration line

The analytical Koehler model yields formulas to determine both critical raw diameter and critical supersaturation as described in equation (17) in the Koehler section of this work.

The parameters molar mass of water M_w, density of pure water p_w and molar mass of Ammoniumsulphat M_s remain the same values as used to plot the Koehler curve previously in the theory section. The A term stays the same as before. For the temperature T it is recommended to use $T = 0.5 \cdot (T_1 + T2)$ where T_1 and T_2 are the temperatures maintained by the TECs at the top and center of the CCNC column (ACTRIS). The B term can be changed slightly to make it a function of the dry solute particle diameter D_s (Petters and Kreidenweis (2007), Seinfeld and Spyros (2006), Rose et al. (2008)). The mass m_s of an ammoniumsulphat particle can be approximated by the mass of a spherical particle $m_s = \frac{1}{6} \cdot \pi D_s^3 \cdot p_s$ where p_s is the density of the solute. Here the value for p_s was chosen as 1770 kg/m^3 which is the density of Ammoniumsulphat at a temperature of 298.15K.

$$B = \frac{i \cdot D_s^3 \cdot p_s \cdot M_l}{M_s \cdot p_l} \qquad A = \frac{4 \cdot \sigma_{sol} \cdot M_w}{R \cdot T \cdot p_w} \tag{35}$$

D_s will be the variable where the critical dry parameter from the activation scan will used. Therefore the equation for the critical supersaturation SS_{crit} has been approximated to a function of the critical dry diameter $D_{s,crit}$.

The x_{half} parameter for figure 19 is a value of (99.6 ± 10.4) nm. With correcting the graph for doubly charged particles (figure 18) the new values of x_{half} equals (99.1 ± 0.3) nm. The correction yields only a slight change in diameter value but the fitting error was reduced significantly because now the fit function follows the data points much more accurately.

Using the latter value as the critical dry diameter for this measurement the critical supersaturation is calculated according to the formula in equation (17 while using the terms A and B from equation 35) for SS_{crit} and it equals a value of 0.14%. No error estimation was given because it is dependent on the error of the critical diameter which would require multiple activation spectra at the same conditions which hasn't been conducted in this work.

This critical supersaturation SS is defined as the effective supersaturation S_{eff} that corresponds to the established temperature gradient set inside the CCNC column. At this effective supersaturation 50% of all particles that have a critical dry size and enter the growth chamber are able to grow into cloud droplets.

Conducting the described measurement principle for multiple nominal supersaturations yields the calibration line for the CCNC. In this experiment the chosen nominal supersaturations for the calibration are 0.1%, 0.2%, 0.3%, 0.4% and 0.5%. Each activation spectra at such a nominal value results in an effective supersaturation SS_{eff} corresponding to the respective temperature gradient ΔT. Plotting SS_{eff} against ΔT and fitting the data points with a linear function $y = k \cdot x + d$ yields the calibration line. The fitting was once again done with the scipy_optimize module in python and initital values for k and d were both set at 1.

6.4.5 S-scans

The S-scan procedure of gaining an activation curve is done similarily to D-scans. The only difference is the X axis of the activatio ratio not being the particle diameter but the nominal supersaturation. The DMA is set at a certain voltage corresponding a particle size while the CCNC steps through multiple nominal supersaturations. Figure 21 shows a summary of the process.

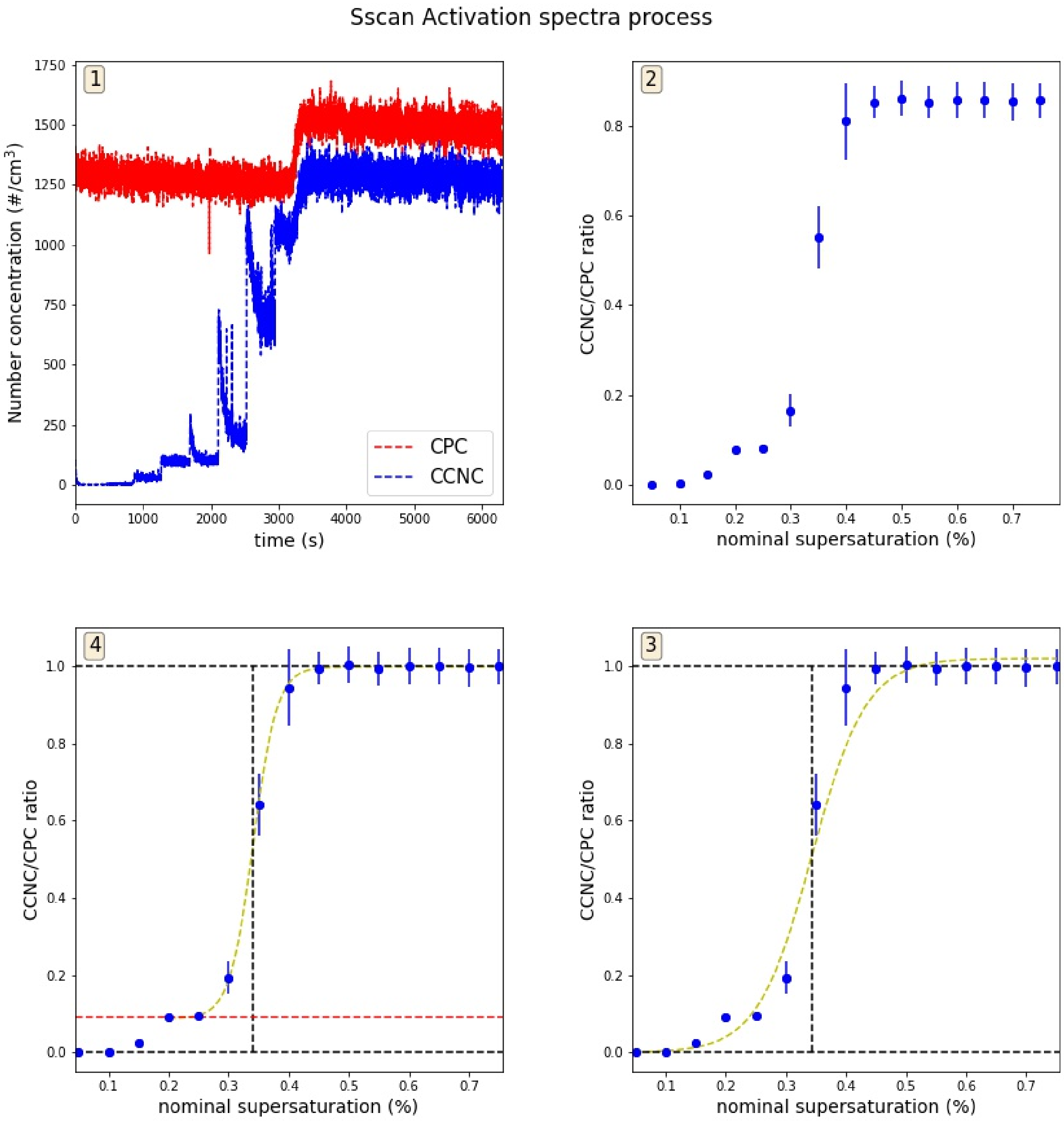

Figure 21: Process of gaining an activation curve with S-scans

Figure 21 showcases the major steps of the S-scan measurement for Ammoniumsulphat with the DMA set at a voltage of 78V, corresponding to a single charged diameter of 40nm. The numbers in the top left corner of each graph indicate the beginning and direction of the process which of course is very similar to D-scans. This work focuses mostly on D-scans. A important detail to note would be the continues difference between the number concentration measured by the CCNC and the one measured by the CPC in the first gaph. Normally in a D-scan spectra both number concentrations would the same range with increasing particle sizes. However this doesn't seem to be the case when keeping the particle size constant and increasing the nominal supersaturation. This may be an indicator that the particle size limits the condensation ability and is most likely the property that has the biggest influence on the CCN activity.

6.4.6 Pollen measurements

The second part of the experiment contains the measurements of the cytoplasmic material samples from various pollen genera. The solution samples were prepared according the extraction method described in Gratzl (2020). Using a pipette droplets of the cytoplasm solutions were mixed with 40mL ultrafine water. Activation curves of soluble cytoplasmic material from 5 pollen types were measured. Those are *Betula pendula* (Birch), *Phleum pratense* (Timothy grass), *Poa pratensis* (blue grass), *Corylus avellana* (Hazel), *Artemisia vulgaris* (Mugwort) and *Ambrosia artemisiifolia* (Ragweed).

For each cytoplasm species the D-scan method is applied at 5 different effective supersaturations SS_{eff} which results in of 5 critical diameter values for each sample. Since these cytoplasm samples exhibit an unknown chemical composition their condensation activity are described through the hycroscopicity parameter κ..

D-scan measurements of the pollen species were done similar to the process described in the Calibration. Due to the lower size distribution of the cytoplasm samples in comparison to the highly active Ammiumsulphat salt at lower mobility diameters the concentration of the sample solutions had to be increased by adding more cytoplasm solution droplets into the sample mixtures. Due to that the dilution line has been removed.

6.5 Results

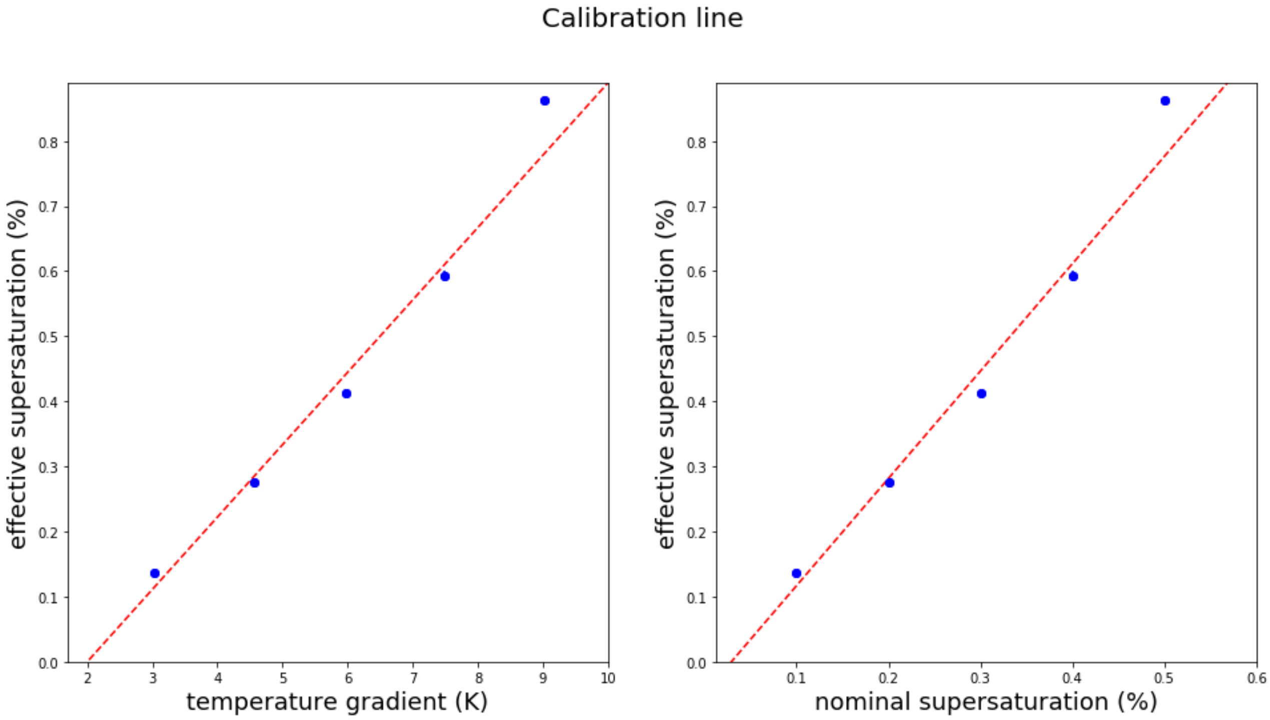

Figure 22: Calibration line from D-scans measurements with Ammoniumsulphat

Figure 22 showcases the effective supersaturation SS_{eff} as a function of both the temperature gradient ΔT and the nominal supersaturation SS_{nom}.

The effective supersaturation SS_{eff} is expected to grow linearly with rising temperature gradients ΔT/nominal supersaturation SS_{nom}. However deviations start to occur at the fifth data point, corresponding to the measurement at a nominal supersaturation of 0.5%. It was tried to approximate equation (17) for the critical supersaturation with a taylor expansion aborted after the linear term but the deviation from linearity did not change. It may be nessecary for calibration lines at higher nominal supersaturation ranges to fit the data points with a non-linear fit in case the deviations from lineratiy continue to rise.

The calibration line makes it possible to determine the true supersaturation S_{eff} that corresponds to a certain temperature gradient ΔT. It also makes it possible to conduct measurements at true supersaturations of 0.1%, 0.2%, 0.3%, 0.4% and 0.5% by simply reshaping the linear function $y = k \cdot x + d$ into $x = \frac{1}{k} \cdot (y - d)$. Putting in the desired S_{eff} value yields the temperature gradient that needs to be put into the CCNC control software. The parameters k and d are known due to the fit culculation from the scipy_optimize module from python. For example an input supersaturation of 0% into x yields a temperature gradient of 2K which is in line with the calibration curve of the left graph in figure 22.

Results for Calibration			
SS_{nom} (%)	ΔT (K)	$D_{s,crit}$ (nm)	SS_{eff}(%)
0.1	3.1 ± 0.1	99	0.14
0.2	4.6 ± 0.1	62	0.28
0.3	5.9 ± 0.1	47	0.41
0.4	7.5 ± 0.1	37	0.59
0.5	9.1 ± 0.1	29	0.86

Table 1: Results for the Calibration measurement

Activation curves of Ammoniumsulphat and all investigated pollen species are seen in figure 23-26. Here the correction for doubly charged particles isn't shown graphically to give a better visual representation of all activation curves for a single species in one graph. Noticeable is the wider gap between the activation spectra at $SS_{eff} = 0.14\%$ and the spectra at the other SS_{eff} values for every graph. This is due to the deviation from linearity between the temperature gradient and the corresponding SS_{eff} value, as seen in the calibration curve in figure 22.

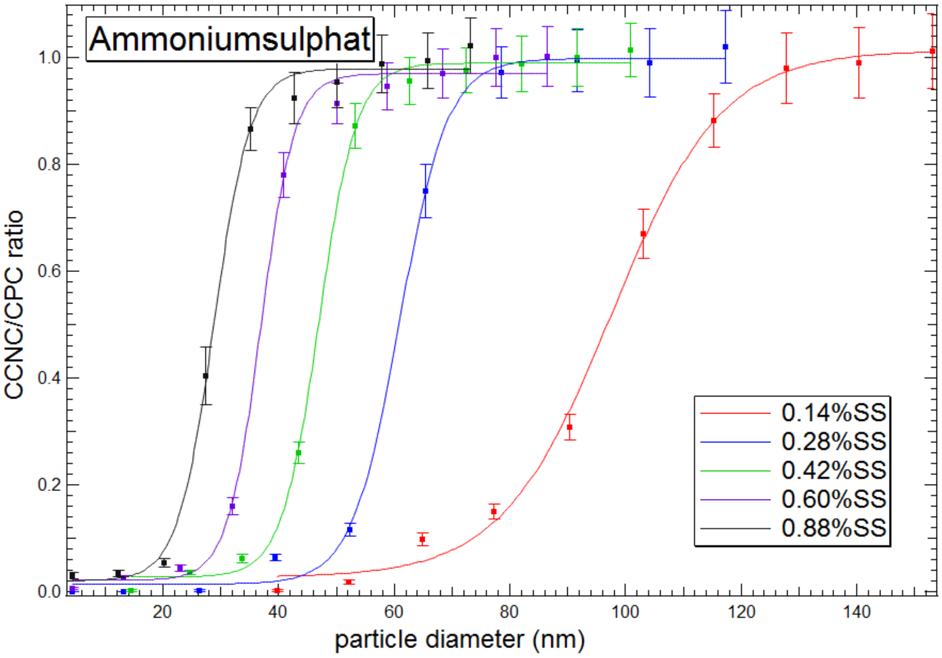

Figure 23: Activation curves of Ammoniumsulphat

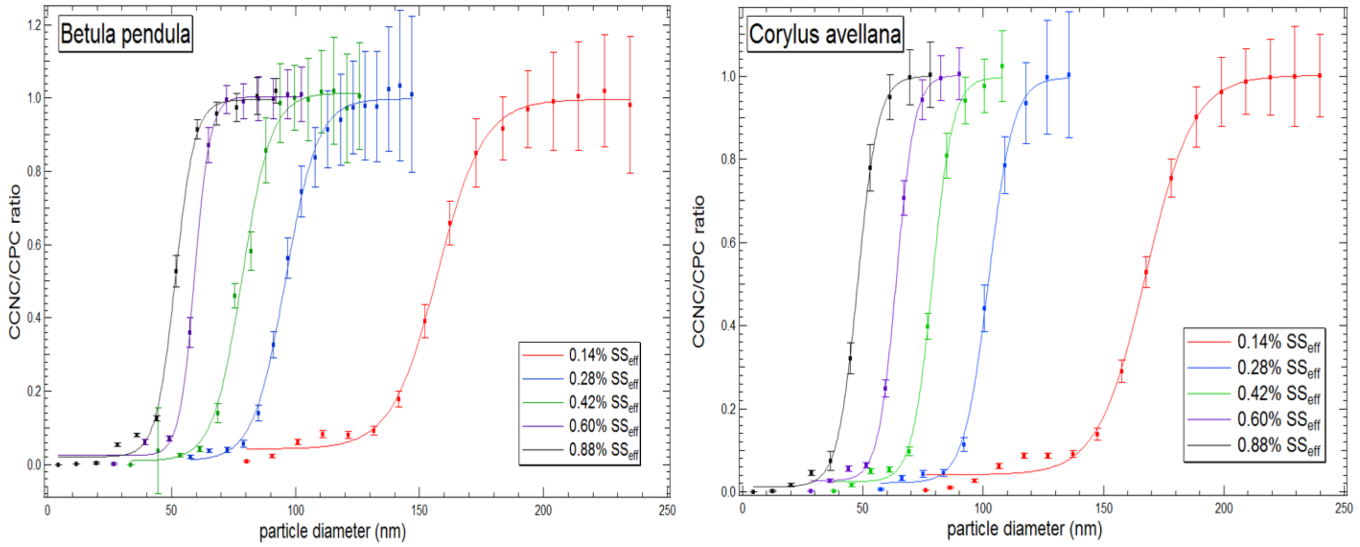

Figure 24: Activation curves of Betula pendula and Corylus avellana

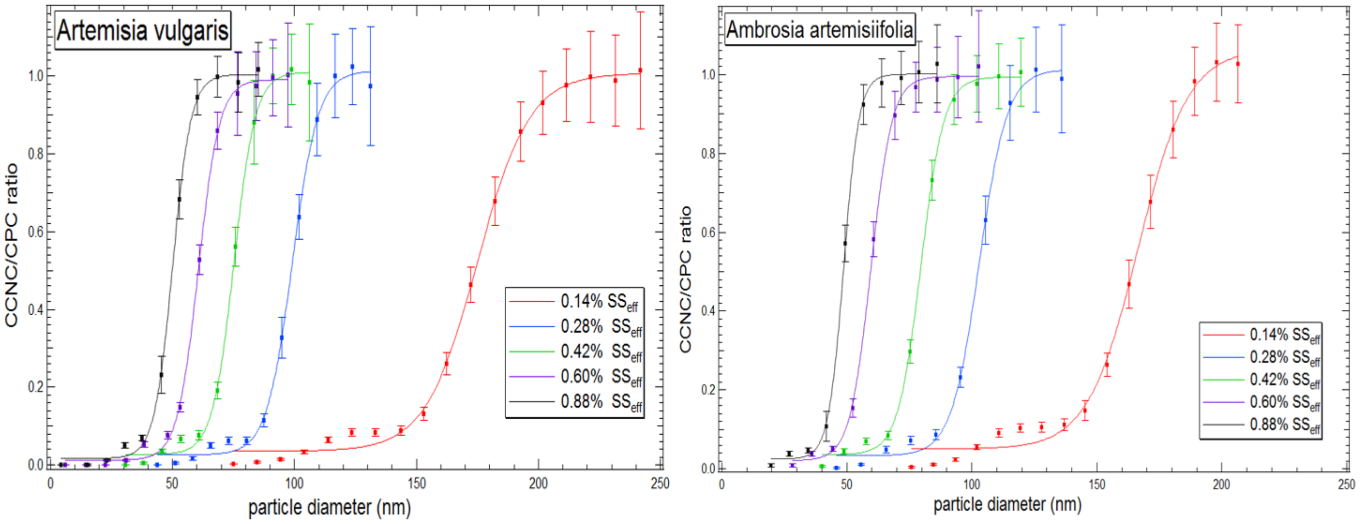

Figure 25: Activation curves of Betula pendula and Corylus avellana

All pollen spectra are roughly in the same diameter range while there is a noticeable shift in diameters for the Ammoniumsulphat spectra. This shift is the strongest for the activation curve at the lowest investigated SS_{eff} of 0.14 and decreases with increasing SS_{eff} value.

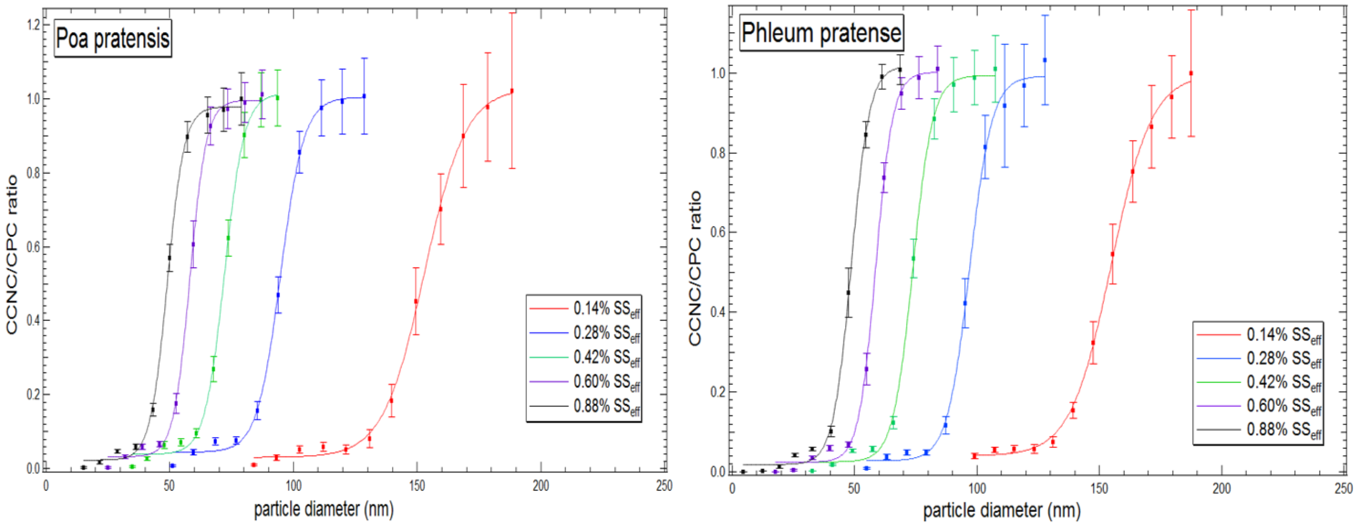

Figure 26: Activation curves of Betula pendula and Corylus avellana

An interesting aspect to note is the increase of the error bars (representing the standard deviations) with higher CCNC/CPC mean ratio values in each activation curve, particularily noticable for the D-Scan Pollen measurements. The existence of deviations in detected cloud droplets stems from losses in the sample line and the finite transfer function of the DMA, allowing to extract a narrow size distribution from a polydisperse sample instead of a perfect monodisperse sample flow, with the maximum of the distribution corresponding to the selected particle size. One would assume that after selecting sizes on the DMA above the critical dry diameter, more particles of the extracted distribution would be counted by the OPC with increasing particle size and thus decreasing the error bars as the probability of a particle growing into a droplet and being counted rises.

However as noted in the beginning chapters for clouds, a higher number of CCN active particles at a fixed supersaturation level means more competition for available water vapor. All particles can potentially activate but not all are able to accumulate enough water molecules onto their surfaces to grow into cloud droplets in their time travelling through the growth chamber. Therefore the deviations in counted droplets increase with higher particle size since more particles at larger sizes makes them stronger CCN which in turn means more competition for the set amount of water vapor in the column.

Tables 1, 2, 3, 4, 5, 6 and 7 showcases the calculated values for the hygroscopicity parameters κ for Ammoniumsulphat and cytoplasm species at their corresponding effective supersaturations SS_{eff} along with their critical dry diameters $D_{s,crit}$.

Results for Ammiumsulphat		
SS_{eff} (%)	$D_{s,crit}$ (nm)	κ
0.14	99	0.73
0.28	62	0.73
0.41	47	0.73
0.59	37	0.73
0.86	29	0.73

Table 2: Results for the Ammiumsulphat sample measurements

Results for Poa		
SS_{eff} (%)	$D_{s,crit}$ (nm)	κ
0.14	152	0.2
0.28	95	0.2
0.41	72	0.2
0.59	58	0.19
0.86	49	0.14

Table 3: Results for the Poa cytoplasm measurements

Results for Phleum		
SS_{eff} (%)	$D_{s,crit}$ (nm)	κ
0.14	153	0.19
0.28	97	0.19
0.41	74	0.19
0.59	59	0.18
0.86	49	0.14

Table 4: Results for the Phleum cytoplasm measurements

Results for Artemisia		
SS_{eff} (%)	$D_{s,crit}$ (nm)	κ
0.14	175	0.13
0.28	99	0.18
0.41	75	0.18
0.59	62	0.16
0.86	50	0.13

Table 5: Results for the Artemisia cytoplasm measurements

Results for Ambrosia		
SS_{eff} (%)	$D_{s,crit}$ (nm)	κ
0.14	167	0.15
0.28	103	0.15
0.41	80	0.15
0.59	60	0.17
0.86	49	0.14

Table 6: Results for the Ambrosia cytoplasm measurements

The results for the κ values of all cytoplasm species lie in the range of 0.1 - 0.2 while the κ values for Ammoniumsulphat stays at a constant value of 0.73. The latter is typical for particles containing hygroscopically active inorganic species (Petters and Kreidenweis (2007)) while the κ values for the cytoplasm fragments agree with the findings of organic emissions over both boreal and tropical forests (Pöhlker et al. (2016), Ryshkevich et al. (2015), Mikhailov et al. (2015), Levin et al. (2014)).

Results for Corylus		
SS_{eff} (%)	$D_{s,crit}$ (nm)	κ
0.14	168	0.15
0.28	102	0.16
0.41	79	0.15
0.59	64	0.14
0.86	48	0.15

Table 7: Results for the Corylus cytoplasm measurements

Results for Birch		
SS_{eff} (%)	$D_{s,crit}$ (nm)	κ
0.14	157	0.18
0.28	98	0.18
0.41	78	0.16
0.59	60	0.18
0.86	52	0.12

Table 8: Results for the Birch cytoplasm measurements

6.5.1 Discussion and comparison with other studies

The results showcase that soluble cytoplasm fragments which emerge during the rupture of pollen grains can in fact serve as nuclei for the formation of droplets in the atmosphere. All 5 investigated cytoplasm samples are able to reach their critical raw diameter at effective supersaturations below 1%, which are typical supersaturation values under which clouds form in the troposphere. At the lowest effective supersaturation of 0.14% the Poa fragments showcase the strongest water uptake ability with a κ value of 2.0 and the smallest critical diameter. Artemisia reaches at that humidity level only a κ value of 1.3, making it the cytoplasm sample with the weakest hygroscopicity.

However it is difficult to say for certain which pollen species showcases the strongest hygroscopicity as κ of all 5 species varies within the range 1.0 - 2.0. In theory the chemical composition and thus the hygroscopiticy of a single pollen species should stay constant at different supersaturations and dry particle sizes. Yet, especially at higher effective supersaturations there is a clear change in the value of κ. I used the approximation formula (x) for κ which is valid for values above 1. The work of Mikhailov et al. (2019) uses a numerical approach to determine κ however their caculations showcased that the difference between the simplified κ formula and their numerical approach doesn't go larger than 7% on average however this deviation could make a slight difference in the calculation. In comparison it is worth to note that for the Ammoinumsulphat measurements κ stays a constant.

What can be said however is that the κ values from each species vary only slightly, showing that all 5 plant species expell cytoplasm fragments with roughly the same water uptake ability. These findings also stay in agreement with other works that investigated the hygroscopic nature of pollen subparticles. The study conducted by Mikhailov et al. (2019) investigated and calculated the κ values from 3 pollen species at very similar effective supersaturations. All 3 species: Pine, Birch and Rape lie in the range $0.11 < \kappa < 0.14$. The Birch sample from our work showcases a slightly stronger hycroscopicity than their sample. This however could also be due to the chemical aging process which improves an organic particle's water affinity after time but the exact time gap between solution sample preparation and measuring their acitivation curve is unknown.

The work of Steiner et al. (2015) which also serves as the main inspiration behind this work investigated the condensation ability of the soluble cytoplasm fraction from 6 pollen types (*Ambrosia*, *Betula*, *Pinus*, *Quercus*, *Carya* and *Juniperus*) using the S-Scan method (at 3 mobility diameters of 50nm, 100nm and 200nm) showcased in figure (x). In our work we analyzed the CCN ability of cytoplasm fragments in the critical dry diameter range of around (50nm-180nm) and we can compare them with their S-Scan measurements of Birch and Ambrosia at critical diameters of 50nm and 100nm. At 50nm Ambrosia exhbits a critical supersaturation of 0.96 and the closest comparison is my measurement of Ambrosia at the effective supersaturation 0.86, yielding a critical diameter of 48nm. Thus my measurement showcases a higher hygroscopicity, indicated since at closely the same raw diameter our Ambrosia sample needs a lower supersaturation value to activate. Solution prepratation and measurement were conducted at the same time in their study while in our work the solution a considerably longer time before being measured. From the Figure 2 in Steiner et al. (2015) where the critical supersaturation is depicted as a function of critical dry particle diameter we can conduct similar comparisons with the Ambrosia and Birch measurements at 100nm. Here their Birch result shows a slightly lower critical supersaturation (around 0.24 in comparison to 0.26 of Ambrosia) and thus a stronger water uptake ability. Unfortunately the exact supersaturation values are not written in the article and thus I can only compare approximately by looking at their graph. The closest comparison would be our D-Scan measurement of Birch and Ambrosia at SS_{eff} of 0.28 where Birch has a lower critical diameter (98nm) than Ambrosia (103nm) and thus supports the slightly stronger hygroscopicity of Birch. The same comparison can be done by looking at the S-Scan results of Ambrosia and Birch at 50nm and my D-Scan measurements of the same pollen types at SS_{eff} of 0.86%. Here however Ambrosia shows a smaller critical dry diameter than Birch, therefore indicating a higher CCN activity. This stands in contrast to the S-Scan measurements where Birch has clearly the higher water uptake ability.

Birch, *Poa* and *Phleum* exhibit a clear shift in κ value between SS_{eff} of 0.86% and the other SS_{eff} levels. It is unknown what causes this shift especially at the highest measurest supersaturation. The very sensitive response of the CCN to noise in the sample line, the DMA's finite resolution, the error between using the simplified version to calculate κ or using the numerical approach as in Mikhailov et al. (2019) or even general mistakes in the caculation could all be sources of reasons for this deviation.

The measurements from Pope (2010) of the CCN ability of whole pollen grains from anemophilous plants showcase that they can activate at supersaturations as low as 0.001%. But their κ values lie in the range of 0.05 - 0.1, indicating a stronger hydrophobic nature than the cytoplasm samples of my work.

The next step for the CCN investigation of Pollen would be to measure the CCN activity of the starch granules within the expelled cytoplasm, the actual subpollen particles. The DMA used for this experiment can classify particles up to a size of 1000nm but the starch granules have sizes of a few micrometers in diameter, thus a longer DMA with a wider classification range would be needed. My work focused on investigating the hygroscopicity of the soluble fraction of expelled cytoplasm from 5 pollen species. As discussed here, atmomized particles of that soluble fraction can activate and grow into cloud droplets under supersaturations typical in the atmosphere ($< 1\%$). Coated with this soluble cytoplasm material to increase their water uptake ability these starch granules are a potential addition to the atmospheric CCN concentration. Due to their smaller size in comparison to pollen grains they are also expected to be a part of atmospheric processes for a much longer time before being deposited to the ground or on other objects. With ever increasing temperatures flowering seasons of angliosperms will become longer and more time can be spend on the production of pollen which in turn increases the amount of allergens but also organic fragments that take part in condensation processes and thus their impact on cloud properties and in turn weather is also potentially increasing.

The measurements here focused on the CCN ability of atomized particles made of the soluble cytoplasm fraction in the laboratory. Although the S-Scan measurement indicated that particle size is the deciding factor for a particle's water uptake ability, it would be an important goal to gain a more information about the chemical composition of the soluble cytoplasm material. The work from Pummer et al. (2013) used the method of Raman and infrared spectroscopy to gain information about the chemical compounds in both intact pollen grains and expelled material when coming to contact with water. Their results show that the expelled soluble cytoplasm differs in their chemical composition between different pollen species but all of them contain a multitude of organic compounds as mentioned before in the theory section for pollen rupture. This stands in agreement with the chemical analysis from Steiner et al. (2015) but in that work there was no distinction made between the starch granules, the actual subparticles and the soluble part of the cytoplasm. The work from Burkart et al. (2019) investigated the composition and mixing state of SPP from various pollen types. The κ results of our work for the soluble cytoplasm samples show a smiliar chemical structure among all pollen types (which only slight variation between pollen type) but despite that, more knowledge of their exact chemical composition could perhaps provide the pathway of predicting which plant types could have a stronger impact on CCN number in the atmosphere.

Adding to that, another important step for the future would be to develop a method that allows for direct in-situ measurements of the number of expelled subparticles during weather conditions that allow for the rupture process to occur. Combining this with the knowledge that would let us find out from which plant type a subparticle (coated with soluble cytoplasm) comes from (by knowing the chemical structure of the soluble cytoplasm around the particle), we could make an assessement how much individual plant species could impact cloud formation processes in regions of dense vegetation.

6.5.2 Impact of cytoplasm fragments on cloud formation

While the expelled cytoplasm material from pollen grains can influence cloud formation processes, the degree of their potential impact is up to this date still a topic for debate.

In the work of Suphioglu et al. (1992) the measured number of starch granules released per rye-grass pollen after rainfall, reaches numbers around 700 to 1000. Using surface pollen count observations over the United States (provided by the American Association for Allergy Asthma and Immunology) we assume an average number of around 10000 pollen grains per m^3 in the atmosphere Steiner et al. (2015). Using that number and taking into account that 1 pollen grains expells up to 1000 cytoplasm fragments, this would result in $10 \cdot 10^7$ pollen subparticles per m^3 and thus 10 subparticles per cm^3. Typical number concentrations of CCN lie in the range of 100 cm^{-3} in remote marine regions up to 1000 cm^{-3} in polluted urban regions.(Seinfeld and Spyros (2006)). Thus the expelled subfragments from pollen don't appear to bring a significant impact on atmospheric CCN numbers.

However as already mentioned in the introductory sections, the number of bioparticles in the atmosphere showcases huge variations depending on multiple factors that include the regional density of vegetation, the temperature and available sources for nutrition. The work from Steiner et al. (2015) predicts that in the northern midlatitutes where pollination is dominated by wind transportation, the number of expelled pollen subparticles is predicated to increase and make impacts on the local number concentration. Furthermore more studies on the release of both smaller soluble cytoplasm fragments and starch granules would be needed to make qualitivite assessments on their potential impact on local CCN concentrations.

6.5.3 Suggested improvements and outlook

The accuracy of the measurement results depends heavily on the stability of the flow through the sample line and the device specific transfer function of the DMA. Furthermore at small particle size ranges diffusion losses play a bigger role on the activation curve, specifically effecting the point of total activation.

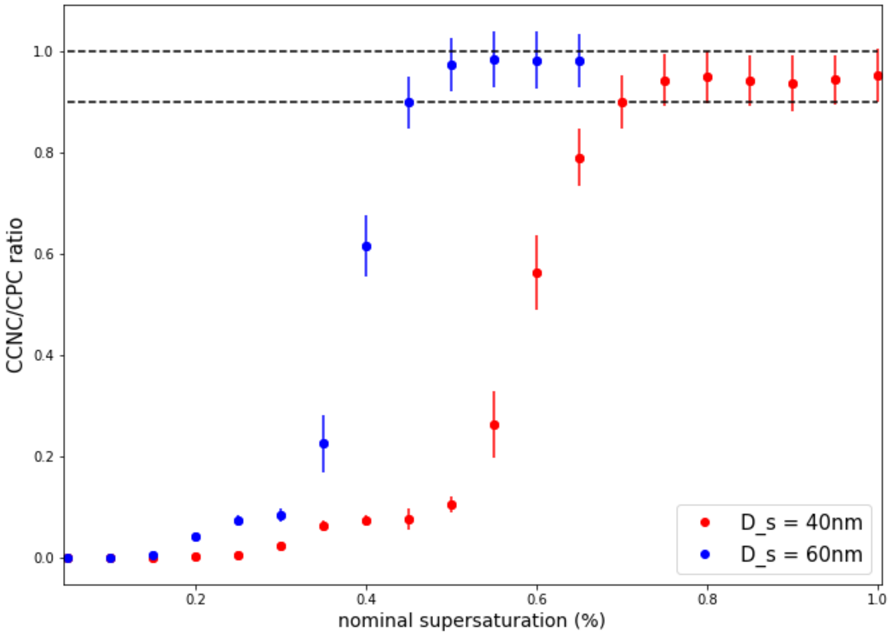

Figure 27: S-Scan activation spectra of Birch cytoplasm (dry diameters of 40nm and 60nm)

Figure 24 shows the activation curves of Birch cytoplasm samples gained through the S-Scan method at 2 different dry diameters D_s. The data points haven't been normalized to showcase how diffusion affects the plateu at maximum activation. At a higher dry size the curve manages to reach ratios closer to 1.

Another aspect to note is that the DMA in this work has been used as a differential mobility particle sizer (DMPS). The alternative would be to use it as a scanning mobility particle sizer (SMPS) which would allow a continuous scan over particle mobilities and would also very likely make it easier to identify the plateu of doubly charged particles. Furtheremore the fitting would probably be done more accurately as holes between the data points could be minimized. To account for that the mobilities corresponding to the particle diameters have been chosen to be as equidistant to each other as possible.

A better transfer function would be possible if the sheath flow through the DMA could be increased. For this work the critical orifice controlls the sheath flow rate at a value of 7.3 L/min. An orifice with a higher flow rate was not available for this work and only the sample through could be controlled through the compressor.

6.6 Outro

The biological fraction of the atmospheric aerosol has become a topic of growing interest among climate researchers in the recent decades due to their significant influence on human mortality and as a potential source of additional CCN and IN (Despres et al. (2012)). Their number concentrations and size distributions are up to this day, riddled with high uncertainties (Andreae and Rosenfeld (2008), Tormo-Molina et al. (2010)).

Pollen, a primary aerosol of biological origin can become a major contributor to the organic fraction of atmospheric aerosols in the peak of pollination seasons in regions with a high density of both boreal and tropical forests (Pöhlker et al. (2016), Ryshkevich et al. (2015), Tormo-Molina et al. (2010)). Despite their micrometer size, these bioparticles can travel up to distances of 1000km before depositing on the ground or on other objects or plants (Schueler and Schlünzen (2006), Sofiev et al. (2006)). They have shown to be effective nuclei for the condensation of water due to their size and their wettable surface (Pope (2010)). But despite their strong water uptake ability and the long travel distances, they still remain not long enough in the atmosphere to be relevant for cloud formation processes.

However under conditions of growing humidity in the air, pollen grains can undergo a process defined as osmotic shock which describes the bursting of the grain's outer layer due to a difference in solute concentration inside and outside the pollen wall (Matamoro-Vidal et al. (2016)). Cytoplasm material from the pollen nucleus is then expelled outside. The main components of pollen cytoplasm are various proteins, starch and additional soluble compounds. Many studies investigated the release of cytoplasm content of pollen from various plant species (Mikhailov et al. (2019), Steiner et al. (2015), Miguel et al. (2006), Taylor et al. (2004), Taylor et al. (2002)) and most studies denounce the expelled cytoplasm material as subparticles or pollen fragments. The work from Gratzl (2020) which my work is based on makes a clear distinction between the starch granules, which are the actual Subpollen Subparticles (SPP) and the soluble cytoplasm material.

Pollen grains loose the ability to expell cytoplasmic content through osmotic shock, a method involving the application of great stress on the pollen walls to force bursting and eventuall emittance of both soluble cytoplasm and SPP is described in great details in the work of Gratzl (2020). Both SPP and soluble material is additionally extracted and prepared as sample solutions. My work analyzes the CCN ability of atomized particles made of this soluble material from 5 different anemophilous plant species.

The main components for my experiment in this study are the Cloud Condensation Nuclei Counter from DMT (CCNC), the Differential Mobility Analyzer (DMA) with cylindrical Vienna Type structure and a Condensation Particle Counter (CPC). The experimental procedure involves the atomization of the sample solution, before drying the produced droplets and letting the sample particles reach the DMA where they are classified according to method of electrical mobility spectrometry (Steiner (2011)). The sample flow exits the DMA as a narrow size distribution before being split between the CCNC and the CPC. The CCNC measures the number of incoming particles which can activate and grow into cloud droplets at certain established supersaturations while the CPC measures all incoming particles. From their recording data I calculate the CCNC/CPC ratios and plot them as a function of the mobility diameter (D-Scans) or as a function of the nominal supersaturation set in the CCNC (S-Scans).

The data is then fitted with a Sigmoid function and corrected for doubly charged particles by finding the plateu of double charges on the graph. The resulting curve is the activation spectra for the sample samples and it's halfway point indicates the critical dry diameter $D_{crit,s}$, the size that the particles of the sample flow need to reach in order for 50% of them to activate and grow into cloud droplets at the given nominal supersaturation. (Rose et al. (2008)). From this critical dry diameter $D_{crit,s}$ I calculate the resulting critical supersaturation SS_{crit}through Koehler theory. This supersaturation is also defined as the effective supersaturation SS_{eff}, the true supersaturation generated in the CCNC column where 50% of passing particles can grow into cloud droplets if they have reached the critical dry diameter.

Measuring D-Scan activation curves of Ammoniumsulphat and plotting the SS_{eff} as a function of the temperature gradient that corresponds to said SS_{eff} yields the calibration line. Both D-Scan and S-Scan measurements of soluble cytoplasm from 5 wind-pollinated plants has been conducted. All samples are able to activate at SS_{eff} lower than 1%, making them thus able to contribute to the atmospheric CCN number concentration. Their hygroscopic ability is described through the parameter κ (Petters and Kreidenweis (2007)) and lies in the range of 0.1 - 0.2. This coincides with the results of studies from (Mikhailov et al. (2019)) and is typical for organic subparticles found over both tropical and boreal forests (Pöhlker et al. (2016), Ryshkevich et al. (2015), Mikhailov et al. (2015), Levin et al. (2014))

Generally their global contribution to atmospheric number concentrations is low but in regions of dense vegetation and during the peak of the blooming seasons of flowers pollen grains can reach numbers that make them substantial contributors to the mass and number of local organic aerosols (Despres et al. (2012)). With increasing temperatures pollination seasons are expected to increase, making their contribution even larger and thus making the study of pollen grains and their cytoplasm fragments a topic that continues to grow in importance.

References

Abbott, J. et al. (2009). *Encyclopedia of Inland Waters.* Academic Press.

Andreae, M. and Rosenfeld, D. (2008). "Aerosol-cloud-precipitation interactions. Part 1. the nature and sources of cloud-active aerosols". *Earth-Science Reviews*, pages pp. 13–41.

Baker, H. G. and Baker, I. (1979). "Starch in angiosperm pollen grains and its anthecological significance". *New Zealand Journal of Botany*, vol. 17(4):pp. 535–535.

Beck, P., Caudullo, G., de Rigo, D., and Tinner, W. (2016). *Betula pendula, Betula pubescens and other birches in Europe: distribution, habitat, usage and threats*, chapter European Atlas of Forest Tree Species. Luxembourg : Publications Office of the European Union.

Behrendt, H., Tomczok, J., Sliwa-Tomczok, W., Kasche, A., von Eschenbach, C. E., Becker, W., and Ring, J. (1999). "timothy Grass (Phleum pratense L.) Pollen as Allergen Carriers and Initiators of an Allergic Response". *International Archives of Allergy and Immunology*, vol. 118:pp. 414 – 418.

Bergman, T., DeWitt, D., Incropera, F., and Lavine, A. (2011). *Fundamentals of Heat and Mass Transfer.* Publisher John Wiley & Sons.

Bohrer, G., Katul, G., Nathan, R., Walko, R., and Avissar, R. (2008). "Effects of canopy heterogeneity, seed abscission and inertia on wind-driven dispersal kernels of tree seeds". *Journal of Ecology*, vol. 96:pp. 569 – 580.

Boucher, O. (2015). *Atmospheric Aerosols.* Springer.

Burge, H. A. (1995). *Bioaerosols, Vol. 2.* CRC Press.

Burkart, J., Gratzl, J., Seifried, T., Grothe, H., and Wonaschütz, A. (2019). "Investigating subparticles of pollen with a single particle mass spectrometer". *12th International Conference on Carbonaceous Particles in the Atmosphere.*

Chen, K., Marusciac, L., Tamas, P., Valenta, R., and Panaitescu, C. (2018). "ragweed Pollen Allergy: Burden, Characteristics, and Management of an Imported Allergen Source in Europe". *International Archives of Allergy and Immunology*, vol. 176:pp. 163 – 180.

Conwell, K., Wiest, J., Anderson, M., Reponen, T., and Grinshpun, S. (2001). "Aerodynamic versus physical size of spores: Measurement and implication for respiratory deposition". *Grana*, vol. 40:pp. 119–125.

DAmato, G. et al. (2007). "Allergenic pollen and pollen allergy in Europe". *Allergy (Copenhagen)*, vol. 62(9):pp. 976–990.

D'Amato, G., Liccardi, G., and Frenguelli, G. (2007). "Thunderstorm-asthma and pollen allergy". *Allergy*, vol. 62:pp. 11–6.

Despres, V. et al. (2012). "Primary biological aerosol particles in the atmosphere: a review". *Tellus B: Chemical and Physical Meteorology*, vol. 64(1):p. 15598.

Diehl, K., Quick, C., Matthias-Maser, S., Mitra, S. K., and Jaenicke, R. (2001). "the ice nucleating ability of pollen Part I: Laboratory studies in deposition and condensation freezing modes". *Atmospheric Research*, vol. 58:pp. 75–87.

Elbert, W., Taylor, P. E., Andreae, M. O., and Pöschl, U. (2007). "Contribution of fungi to primary biogenic aerosols in the atmosphere: wet and dry discharged spores, carbohydrates, and inorganic ions". *Atmospheric Chemistry and Physics*, vol. 7(17):pp. 4569–4588.

Forster, P. (2007). "Changes in atmospheric constituents and in radiative forcing, in Climate Change 2007: The Physical Science Basis". *Contribution of Working Group i to the Fourth Assessment Report of the Intergovernmental Panel on Climate Change*, 2007.

Franchi, G., Bellani, L., Nepi, M., and Pacini, E. (1996). "Types of carbohydrate reserves in pollen: localization, systematic distribution and ecophysiological significance". *Flora*, vol. 191:pp. 143–159.

Fröhlich-Nowoisky, J. et al. (2016). "Bioaerosols in the Earth System: Climate, Health, and Ecosystem Interactions". *Atmospheric Research*, vol. 182:pp. 346–376.

Gratzl, J. (2020). "Extraction and size distribution measurements of subpollen particles". Master's thesis, Faculty of Physics, University of Vienna.

Hinds, W. C. (2012). *Aerosol technology: properties, behavior, and measurement of airborne particles*. John Wiley & Sons.

Hoose, C., Kristjánsson, J. E., and Burrows, S. M. (2010). "How important is biological ice nucleation in clouds on a global scale?". *Environmental Research Letters*, vol. 5(2):p. 024009.

Houghton, J. et al. (2001). *Contribution of Working Group I to the Second Assessment Report of the Intergovernmental Panel on Climate Change. WMO/UNEP*. Cambridge University Press.

Jaenicke, R. (2005). "Abundance of Cellular Material and Proteins in the Atmosphere". *Science (New York)*, vol. 308:p. 73.

Jones, A. and Harrison, R. (2004). "The Effects of Meteorological Factors on Atmospheric Bioaerosol Concentrations a Review". *The Science of the total environment*, vol. 326:pp. 151–80.

Kazinczi, G., Novák, R., Pathy, Z., and Béres, I. (2008). "common ragweed (Ambrosia artemisiifolia l.): A review with special regards to the results in Hungary: III. Resistant biotypes, control methods and authority arrangements". *Herbologia*, vol. 9:pp. 119–144.

Knut, F., Johannes, I., Peter, E. K., and Knut, K. (1989). *Textbook of pollen analysis*. John Wiley and Sons Ltd.

Kuparinen, A., Katul, G., Nathan, R., and Schurr, F. (2009). "Increases in air temperature can promote wind-driven dispersal and spread of plants". *Proceedings. Biological sciences / The Royal Society*, vol. 276:pp. 3081–3087.

Lachlan-Cope, T. (2010). "Antarctic clouds". *Polar Research*, vol. 29(2):pp. 150–158.

Lance, S., Medina, J., Smith, J., and Nenes, A. (2006). "Mapping the operation of the DMT Continuous Flow CCN counter". *Aerosol Science and Technology - AEROSOL SCI TECH*, vol. 40:pp. 242–254.

Lathem, T. L. and Nenes, A. (2011). "water Vapor Depletion in the DMT Continuous-Flow CCN Chamber: Effects on Supersaturation and Droplet Growth". *Aerosol Science and Technology*, vol. 45(5):pp. 604–615.

Laurence, A., Thoms, A., Bryant, V., and Mcdonough, C. (2011). "Airborne Starch Granules as a Potential Contamination Source at Archaeological Sites". *Journal of Ethnobiology*, vol. 31:pp. 213–232.

Levin, E. et al. (2014). "Size-resolved aerosol composition and its link to hygroscopicity at a forested site in Colorado''. *Atmospheric Chemistry and Physics*, vol. 14:pp. 2657–2667.

Lohmann, U. and Feichter, J. (2005). "Global indirect aerosol effects: a review". *Atmospheric Chemistry and Physics*, vol. 5(3):pp. 715–737.

Lohmann, U., Lueoend, F., and Mahrt, F. (2016). *An Introduction to Clouds: From the Microscale to Climate.* Cambridge University Press.

Matamoro-Vidal, A. et al. (2016). "Links between morphology and function of the pollen wall: An experimental approach". *Botanical Journal of the Linnean Society*, vol. 180:pp. 478–490.

McFiggans, G. et al. (2006). "The effect of physical and chemical aerosol properties on warm cloud droplet activation". *Atmospheric Chemistry and Physics*, vol. 6(9):pp. 2593–2649.

Metz, B., Davidson, O., Swart, R., and Pan, J. (2001). *Climate Change 2001: Mitigation, Contribution of Working Group III to the Third Assessment [TAR] Report of the Intergovernmental Panel on Climate Change (IPCC).* Cambridge University Press.

Miguel, A. G., Taylor, P. E., House, J., Glovsky, M. M., and Flagan, R. C. (2006). "Meteorological Influences on Respirable Fragment Release from Chinese Elm Pollen". *Aerosol Science and Technology*, vol. 40:pp. 690–696.

Mikhailov, E., Ivanova, O., Nebosko, E., Vlasenko, S., and Ryshkevich, T. (2019). "Subpollen Particles as Atmospheric Cloud Condensation Nuclei". *Izvestiya, Atmospheric and Oceanic Physics*, vol. 55:pp. 357–364.

Mikhailov, E., Ivanova, O., Vlasenko, S., Nebosko, E., and Ryshkevich, T. (2017). "Cloud condensation nuclei activity of the Aitken mode particles near St. Petersburg, Russia". *Izvestiya, Atmospheric and Oceanic Physics*, vol. 53:pp. 326–333.

Mikhailov, E. F. et al. (2015). "Chemical composition, microstructure, and hygroscopic properties of aerosol particles at the Zotino Tall Tower Observatory (ZOTTO), Siberia, during a summer campaign". *Atmospheric Chemistry and Physics*, vol. 15(15):pp. 8847–8869.

Moore, R. and Nenes, A. (2009). "Scanning flow CCN analysis a method for fast measurements of CCN spectra". *Aerosol Science and Technology*, vol. 43:pp. 1192–1207.

Noh, Y. et al. (2012). "Investigation of the diurnal pattern of the vertical distribution of pollen in the lower troposphere using LIDAR". *Atmospheric Chemistry & Physics Discussions*, vol. 12:pp. 31187–31204.

O'Dowd, C. D., Smith, M. H., Consterdine, I. E., and Lowe, J. A. (1997). "Marine aerosol, sea-salt, and the marine sulphur cycle: a short review". *Atmospheric Environment*, vol. 31(1):pp. 73–80.

Ogden, E., Hayes, J., and Raynor, a. (1969). "DIURNAL PATTERNS OF POLLEN EMISSION IN AMBROSIA, PHLEUM, ZEA, AND RICINUS". *American Journal of Botany*, vol. 56:pp. 16–21.

Pacini, E., Guarnieri, M., and Nepi, M. (2006). "Pollen carbohydrates and water content during development, presentation, and dispersal: A short review". *Protoplasma*, vol. 228:pp. 73–77.

Paivi M, S. et al. (2014). "Prevalence of allergic sensitization in the United States: results from the National Health and Nutrition Examination Survey (NHANES) 2005-2006". *Journal of Allergy and Clinical Immunology.*

Petters, M. D. and Kreidenweis, S. M. (2007). "A single parameter representation of hygroscopic growth and cloud condensation nucleus activity". *Atmospheric Chemistry and Physics*, vol. 7(8):pp. 1961–1971.

Pöhlker, M. et al. (2016). "Long-term observations of cloud condensation nuclei in the Amazon rain forest – Part 1: Aerosol size distribution, hygroscopicity, and new model parametrizations for CCN prediction". *Atmospheric Chemistry and Physics*, vol. 16:pp. 15709–15740.

Pope, F. D. (2010). "Pollen grains are efficient cloud condensation nuclei". *Environmental Research Letters*, vol. 5(4):p. 044015.

Pöschl, U. et al. (2010). "Rainforest Aerosols as Biogenic Nuclei of Clouds and Precipitation in the Amazon". *Science (New York)*, vol. 329:pp. 1513–1516.

Pringle, K. J., Tost, H., Pozzer, A., Pöschl, U., and Lelieveld, J. (2010). "Global distribution of the effective aerosol hygroscopicity parameter for CCN activation". *Atmospheric Chemistry and Physics*, vol. 10(12):pp. 5241–5255.

Pruppacher, H. and Klett, J. (2010). *Microphysics of Clouds and Precipitation*, volume 18. Springer Netherland.

Pummer, B. et al. (2013). "Chemistry and morphology of dried-up pollen suspension residues". *Journal of Raman Spectroscopy*, vol. 44(12):p. 4395.

Raatikainen, T., Moore, R., Lathem, T., and Nenes, A. (2012). "A coupled observation - modeling approach for studying activation kinetics from measurements of CCN activity". *Atmospheric Chemistry and Physics*, vol. 12:pp. 4227–4243.

Ramanathan, V., Crutzen, P., Kiehl, J., and Rosenfeld, D. (2002). "Aerosols, Climate, and the Hydrological Cycle". *Science (New York)*, vol. 294(5549):pp. 2119 – 2124.

Reischl, G. P. (1991). "Measurement of Ambient Aerosols by the Differential Mobility Analyzer Method: Concepts and Realization Criteria for the Size Range Between 2 and 500 nm". *Aerosol Science and Technology*, vol. 14(1):pp. 5–24.

Roberts, G. and Nenes, A. (2005). "A Continuous-Flow Streamwise Thermal-Gradient CCN Chamber for Atmospheric Measurements". *Aerosol Science and Technology - AEROSOL SCI TECH*, vol. 39:pp. 206–221.

Rose, D. et al. (2008). "Calibration and measurement uncertainties of a continuous-flow cloud condensation nuclei counter (DMT - CCNC): CCN activation of ammonium sulfate and sodium chloride aerosol particles in theory and experiment". *Atmospheric Chemistry and Physics*, vol. 8(5):pp. 1153–1179.

Ryshkevich, T., Mironov, G., Mironova, S., Vlasenko, S., Chi, X., Andreae, M., and Mikhailov, E. (2015). "Comparative analysis of hygroscopic properties of atmospheric aerosols at ZOTTO Siberian background station during summer and winter campaigns of 2011". *Izvestiya - Atmospheric and Ocean Physics*, vol. 51:pp. 512–519.

Schaeppi, G., Taylor, P., Staff, I., Suphioglu, C., and Knox, R. (1997). "Source of Bet v 1 loaded inhalable particles from birch revealed". *Sexual Plant Reproduction*, vol. 10:pp. 315–323.

Schueler, S. and Schlünzen, H. (2006). "Modeling of oak pollen dispersal on the landscape level with a mesoscale atmospheric model". *Environmental Modeling and Assessment*, vol. 11:pp. 179–194.

Seinfeld, J. H. and Spyros, N. P. (2006). *Atmospheric Chemistry and Physics: From Air Pollution to Climate Change.* John Wiley & Sons.

Sofiev, M., Siljamo, P., Ranta, H., and Rantio-Lehtimäki, A. (2006). "Towards numerical forecasting of long-range air transport of birch pollen: Theoretical considerations and a feasibility study". *International journal of biometeorology*, vol. 50:pp. 392–402.

Steiner, A. L., Brooks, S., Deng, C., Thornton, D., Pendleton, M., and Bryant, V. (2015). "Pollen as atmospheric cloud condensation nuclei". *Geophysical Research Letters*, vol. 42(9):pp. 3596–3602.

Steiner, G. (2011). *"High Resolution Mobility Spectrometry Of Molecular Ions And Their Effect On The Charging Probabilities Of Airborne Particles Under Bipolar Diffusion Charging Conditions".* PhD thesis, Faculty of Physics, Uiversity of Vienna.

Suphioglu, C., Singh, M., Taylor, P., Knox, R., Bellomo, R. R., Holmes, P., and Puy, R. (1992). "Mechanism of grass-pollen-induced asthma". *The Lancet*, vol. 339(8793):pp. 569–572. Originally published as Volume 1, Issue 8793.

Taylor, P., Flagan, R., Miguel, A., Valenta, R., and Glovsky, M. (2004). "Birch pollen rupture and the release of aerosols of respirable allergens". *Clinical & Experimental Allergy : Journal of the British Society for Allergy and Clinical Immunology*, vol. 34:pp. 1591–1596.

Taylor, P., Flagan, R., Valenta, R., and Glovsky, M. (2002). "Release of allergens as respirable aerosols: A link between grass pollen and asthma". *The Journal of Allergy and Clinical Immunology*, vol. 109:pp. 51–56.

Tomasi, C., Fuzzi, S., and Kokhanovsky, A. (2016). *Atmospheric Aerosols: Life Cycles and Effects on Air Quality and Climate.* Wiley VCH Verlag GmbH and Co. KGaA.

Tormo-Molina, R., Silva, I., Gonzalo, A., Moreno, A., Pérez, R., and Fernández-Rodríguez, S. (2010). "Phenological records as a complement to aerobiological data". *International journal of biometeorology*, vol. 55:pp. 51–65.

Twomey, S. (1977). "The Influence of Pollution on the Shortwave Albedo of Clouds". *Journal of The Atmospheric Sciences*, vol. 34:pp. 1149–1154.

Wendisch, M. (1999). "h. R. Pruppacher and J. D. Klett, Microphysics of Clouds and Precipitation". *Journal of Atmospheric Chemistry*, vol. 32:pp. 420–422.

Winiwarter, W., Bauer, H., Caseiro, A., and Puxbaum, H. (2009). "Quantifying emissions of primary biological aerosol particle mass in Europe". *Atmospheric Environment*, vol. 43:pp. 1403–1409.

Winklmayr, W., Reischl, G., Lindner, A., and Berner, A. (1991). "New electromobility spectrometer for the measurement of aerosol size distributions in the size range from 1 to 1000 nm". *Journal of Aerosol Science*, pages pp. 289–296.